FREE BODIES IN UNSTEADY VISCOUS FLOWS AND SIMPLE MECHANICAL ANALOGS: NONLINEAR DYNAMICS AND UNDERACTUATED CONTROL

by

Rodrigo Abrajan Guerrero

A dissertation submitted to the faculty of
The University of North Carolina at Charlotte
in partial fulfillment of the requirements
for the degree of Doctor of Philosophy in
Mechanical Engineering

Charlotte

2018

Approved by:

Dr. Scott D. Kelly

Dr. Christopher Vermillion

Dr. James M. Conrad

Dr. Yogendra Kakad

ABSTRACT

RODRIGO ABRAJAN GUERRERO. Free bodies in unsteady viscous flows and simple mechanical analogs: nonlinear dynamics and underactuated control. (Under the direction of DR. SCOTT D. KELLY)

In this dissertation we study the interactions between free bodies and unsteady viscous flows, with particular interest in locomotion and in particle transport in streaming flows.

For self-propelling bodies, we present systems with two different mechanisms that generate locomotion. The first one obtains its propulsive force from vortex shedding that results from the spinning of a rotor internal to a hydrofoil. The second type of locomotion results from changes in shape of the system, similar to the deformations one sees in a fish as it swims. We present a set of swimmers whose configuration manifold exhibits the structure of a trivial principal fiber bundle. For such systems, locomotion can be obtained from cyclic actuation of the shape variables, as long as the corresponding closed loops in the manifold of body shapes enclose a certain kind of curvature. In the robotics literature, this curvature is typically obtained from an analytical model. We present a strategy to obtain the curvature of a system from experiments. We also study the performance of a swimmer with underactuated dynamics on the shape manifold. We show that single input actuation can enable locomotion comparable to that realized with full actuation in the shape variables.

For particles in streaming flows, we concentrate on flows generated by oscillating cylinders in a viscous fluid. Particles in such flows get trapped in the centers of streaming cells. We explore strategies — with the aid of a low-order approximation

and a high-fidelity model — to transport particles from a streaming cell near one cylinder to a streaming cell near another cylinder.

DEDICATION

To my wife, my parents, and all my family.

ACKNOWLEDGMENTS

I would like to thank my advisor Dr. Scott D. Kelly for his guidance and support during the realization of this work. Special thanks to Dr. Ronald E. Smelser for being a good friend and always stopping by the lab to check on us. I also want to thank the members of my Ph.D. dissertation committee for their time and suggestions.

I will always remember my friends from the lab, TB, Mike, Rakshit, Blake and Hunter. It was always fun working with them.

I want to acknowledge the Univeristy of North Carolina at Charlotte, Mexico's National Council of Science and Technology (CONACYT), and my advisor for providing financial support for my studies.

I want to thank my family in Mexico for always showing their support.

Finally, thanks to my wife for her support and always believing in me.

TABLE OF CONTENTS

LIST OF FIGURES

LIST OF TABLES

CHAPTER 1: INTRODUCTION

In this document we will study how free bodies interact with unsteady viscous flows, in particular we are interested in how these bodies can move in the fluid. We will consider the case in which bodies are self propelled by actuation of some internal variables and the case in which the bodies — particles in particular — are advected or transported in streaming flows.

For the self-propelled systems considered, locomotion is obtained by one of two different mechanism, in one it is done with vortex shedding — breaking symmetry in the system — through the actuation of a single degree of freedom. The other mechanism is where the system exhibits a configuration manifold with the structure of a principal fiber bundle where points in base manifold represent different shape configurations and the fibers are diffeomorphic to $SE(2)$, the spatial coordinates in planar locomotion. In the cases considered herein, there exists a principal connection in the bundle such that cyclic changes in shape variables result in motion along the fibers, the holonomy. To be able to obtain this holonomy, motion along the fibers, the shape change needs to describe a close loop that encloses some area; typically, in robotics this is obtained by having full actuation over the shape variables. We consider a case where instead of having direct actuation in all shape variables one of the joints is elastic compliant, and the passive dynamics show to be sufficient in some cases to generate such loops in the shape manifold that result in locomotion. The

document is organized as follows.

Chapter 2 presents a rigid hydrofoil with an internal rotor. Rotation of the internal rotor — via a servo motor — causes the hydrofoil to counter rotate, because of conservation of angular momentum. The rotations of the hydrofoil shed vorticity at the tip, due to exchange of momentum the hydrofoil propels forward. Using a PI controller it is shown experimentally that both the heading and swimming speed of the hydrofoil can be controlled. The self-recovery phenomenon ([9], [10], [11]) is observed and analyzed in the system.

In Chapter 3, we visit an analog to the system of Chapter 2, the Chaplygin beanie. This system shares the caracteristic of being constrained — an even harder constriant in this case — to move only forward, in the hydrofoil this is due to the teardrop shape of the hydrofoil, making it easier to move longitudinally, and in the Chapligyn beanie it is due to a nonholonomic constraint, preventing the rear wheel from slipping laterally. The constraint of the swimmer may be considered as a relaxed version of the constraint on the Chaplygin beanie. Experimental results show that heading and speed may also be controlled in this case with a PI controller. This had already been shown in [24] in simulation but had never been done or validated with physical experiments.

In Chapter 4 we present two systems that swim in viscous fluid. The first system is Purcell's canonical three-link swimmer [40]. The second is a novel system consisting of an array of 4 paddles which are actuated in pairs, having two degrees of freedom in shape space in both cases. Assuming the systems and fluid start from rest, both systems can be modeled in terms of a principal connection on a fiber bundle. This

can be exploited using techniques from geometric mechanics to design actuation gaits that will make the system locomote. To use this techniques it is necessary to have an analytical model from which a local connection can be extracted, which can then be used to obtain curvature plots from where the gaits can graphically be designed. We present a methodology with which the curvature plots can be approximated from a sequence of experiments. A comparison between the experimental and theoretical curvature plots is made.

Chapter 5, looks at a variation of Purcell's swimmer, it is a three-link swimmer in ideal flow, i.e., inviscid and irrotational. This system can also be modeled in terms of a principal connection; from the connection, curvature plots may be obtained from which it can be seen what shape changes can result in better locomotion. The system has two joints, which can be fully actuated or one may be set as an elastic compliant joint. A comparison between locomotion obtained in the fully actuated case and the singly actuated case is done, including comparisons of power consumption.

In Chapter 6 we look at the problem of transporting particles using streaming cells generated when a cylinder is vibrated laterally in a fluid. In particular we devise a strategy in which two vibrating probes can be used together to move the streaming cells around in the plane. By cyclic variation of two parameters we create background flows that could move particles to new locations different than those obtained with a single oscillating probe.

In Chapter 7, we make use of a high-fidelity simulation to validate the strategy used in Chapter 6 to move streaming cells in the plane through cyclic variation of a set of parameters. We also investigate the option of using an averaged flow of the

oscillating cylinders to track inertial particles, the behavior of particles is compared to that obtained in the full oscillatory flow.

Chapter 8 outlines the contributions of this dissertation and potential lines of research for future work.

CHAPTER 2: HEADING CONTROL OF A RIGID HYDROFOIL WITH AN INTERNAL ROTOR

2.1 Introduction

In this chapter we study the planar self-propulsion and maneuvering of a free rigid hydrofoil with a balanced internal rotor. The system is depicted schematically in the left panel of Fig. 1. A solitary control input regulates the difference in orientation between the foil and the rotor. Spinning the rotor relative to the foil induces the foil to counter-spin; lateral movement of the foil's trailing point through a surrounding fluid generates a propulsive force with a nonzero component aligned along the foil's axis of symmetry. This force reflects the shedding of vorticity from the foil's trailing point in accordance with variations in the circulatory flow around the foil. The foil's vortical wake advects momentum away from the foil and the foil attains contrary momentum in the balance. The rotor is "internal" in the sense that it doesn't interact directly with the surrounding fluid. A physical realization of this system is depicted in the right panel of Fig. 1. The foil takes the form of a styrofoam raft two and a half centimeters thick that floats with roughly half this thickness submerged when placed in water. The rotor is mounted atop the raft to isolate it from the water.

A system analogous to that in Fig. 1, comprising a rotor mounted not atop a raft in a fluid but atop a platform supported — like a typical shopping cart is supported — by casters in front and by wheels in the rear, was introduced in [24] and named the

Chaplygin beanie.[1] The present system and the Chaplygin beanie share the feature that lateral movement is resisted in the rear but not in the front, as a consequence of which a rotor-driven oscillation in heading will necessarily give rise to forward propulsion. It was shown in [24] that if the Chaplygin beanie is initially at rest, then it's possible to vary the relative heading of the rotor thereafter in a manner that will drive the system to translate asymptotically at an arbitrary heading with an arbitrary translational speed. In particular, a proportional controller of the form $\ddot{\phi} = k\theta$ (in the notation of Fig. 1) was shown analytically to drive the heading angle θ asymptotically to zero as the system approached a steady translational speed depending monotonically on the constant feedback gain k. The Chaplygin beanie will be visited again in Chapter 3.

The system in Fig. 1 is susceptible to primitive control of this kind only to a limited degree, primarily because the resistance to lateral motion at the rear of the foil is not absolute as it is in the case of a nonholonomically constrained cart with wheels. The force that resists lateral motion at the rear of the foil isn't a force of constraint, but is instead a force that dissipates energy as the foil rotates. This dissipation of energy exposes the system to the phenomenon termed *damping-induced self-recovery* in [9, 10, 11], whereby the rotor-driven rotation of a body subject to (exclusively or partly) viscous drag will be (entirely or partly, respectively) undone when rotor motion stops. A mathematical analysis of self-recovery in the presence of purely viscous drag appears in the preceding references.

[1] The Chaplygin beanie combines features of two canonical systems from the mechanics literature, *Elroy's beanie* ([33, 32]) and the *Chaplygin* (or *Carathéodory*) *sleigh* ([6, 15]).

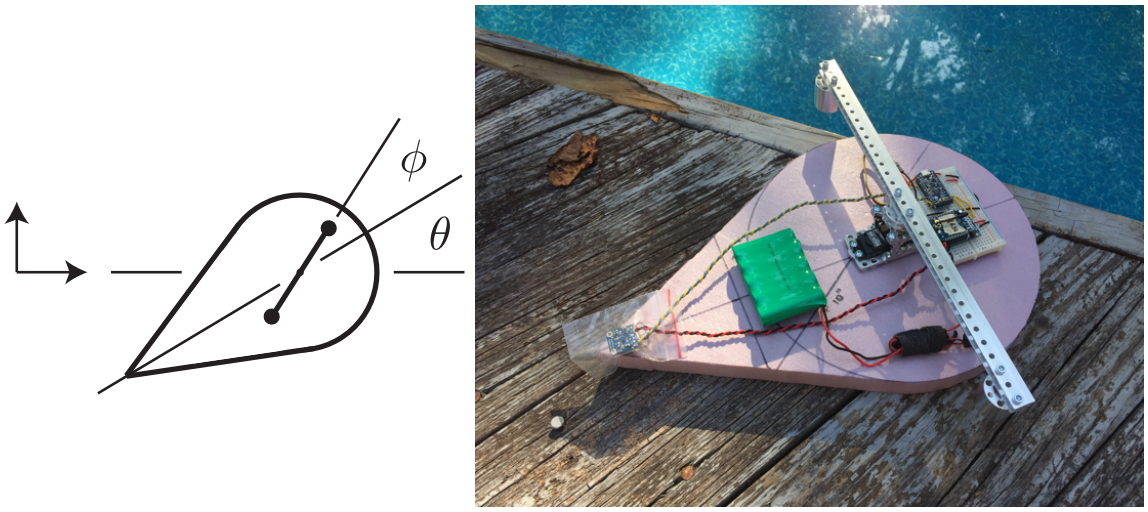

Figure 1: A planar aquatic vehicle comprising a rigid hydrofoil coupled to a balanced rotor. Spinning the rotor counter-rotates the foil; oscillations in the foil's heading generate forward propulsion. The styrofoam foil on the right is thirty-six centimeters long and twenty-four centimeters wide.

In section 2.2, we demonstrate with laboratory data that the essential premise of [24] — that regulation of the Chaplygin beanie's heading will engender forward propulsion as a byproduct, and that sufficient freedom is available in the design of heading controllers to accommodate the additional regulation of translational speed — also applies to the system in Fig. 1. In section 2.3, we demonstrate that if the dissipative moment resisting rotation of the foil is linear in $\dot{\theta}$, then the self-recovery phenomenon prohibits permanent reorientation of the foil as a result of finite-time changes in the relative orientation of the rotor, but that nonlinearity in this moment may be exploited to attenuate recovery. In section 2.4, we draw attention to a saturation phenomenon that sometimes accompanies damping-induced recovery, presenting a model-based analysis to guide future physical experiments.

2.2 Propulsion through Heading Control

Proportional and integral feedback control laws were tested for regulating the heading of the physical foil shown in Fig. 1. The measurement of θ was obtained using the STMicro L3DG20H gyrometer contained within a ten-degree-of-freedom inertial measurement unit available from Adafruit. The gyrometer measures angular velocity, which can be integrated to obtain angular position over short periods of time. Only the z-axis measurement was used; the sensor was mounted on the tail of the foil with this axis pointed upward. The control routine was programmed to an Adafruit Pro Trinket, an ATMega328-based microcontroller. An XBee radio module was used to enable serial communication between the microcontroller and a PC so that control parameters could be adjusted remotely during testing. The rotor visible in Fig. 1 comprises a length of aluminum Actobotics "mini channel", to which weights can be affixed at a variety of locations to vary the rotor's inertia, mounted atop a Hitec HSR-1425CR continuous-rotation servomotor. Also visible in the figure is a 6V 2200mAh NiMH battery used to power the servo, microcontroller, XBee, and sensors.

Experiments were performed in a 240×120 centimeter pool, shown in Fig. 2, filled with water roughly eight centimeters deep. A Raspberry Pi with a camera module was mounted three meters above the pool to record video, from which trajectories of the foil's extremes and the rotor's extremes could be extracted. The camera was used only to collect data for post-processing; the microcontroller used only measurements from the IMU to regulate the behavior of the rotor. A projective transformation was used to convert trajectories in the camera's view to real-world coordinates. The

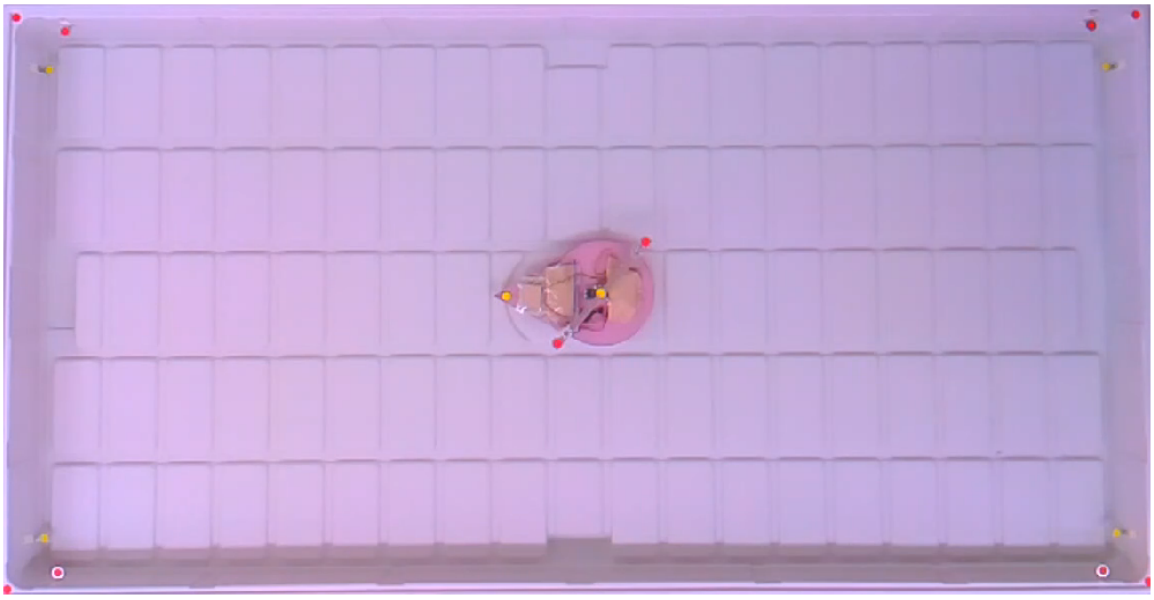

Figure 2: The laboratory pool with the foil in the center as viewed from a camera mounted three meters above. The red tone in the image is the result of brightness, saturation, and white balance settings that were determined to facilitate tracking of the colored markers. The pool floor is actually white.

stationary markers visible in the corners of the pool in Fig. 2, situated at different heights to match the heights of the markers on the foil and rotor, facilitated realization of this transformation.

Each experiment began with the foil at rest near one end of the pool, where it would receive a command to reorient counterclockwise to increase the heading angle θ from zero to $\pi/18$ radians using a PI controller to determine the angular velocity of the servo from the foil's orientation. Fig. 3 shows the trajectories obtained with five different sets of control gains, three corresponding to purely integral control (on the top) and two corresponding to purely proportional control (on the bottom). The trajectory of the center of the rotor is shown in each case for a period of twenty-six seconds, corresponding to the time required for the integral controller with $k_i = 7$ to

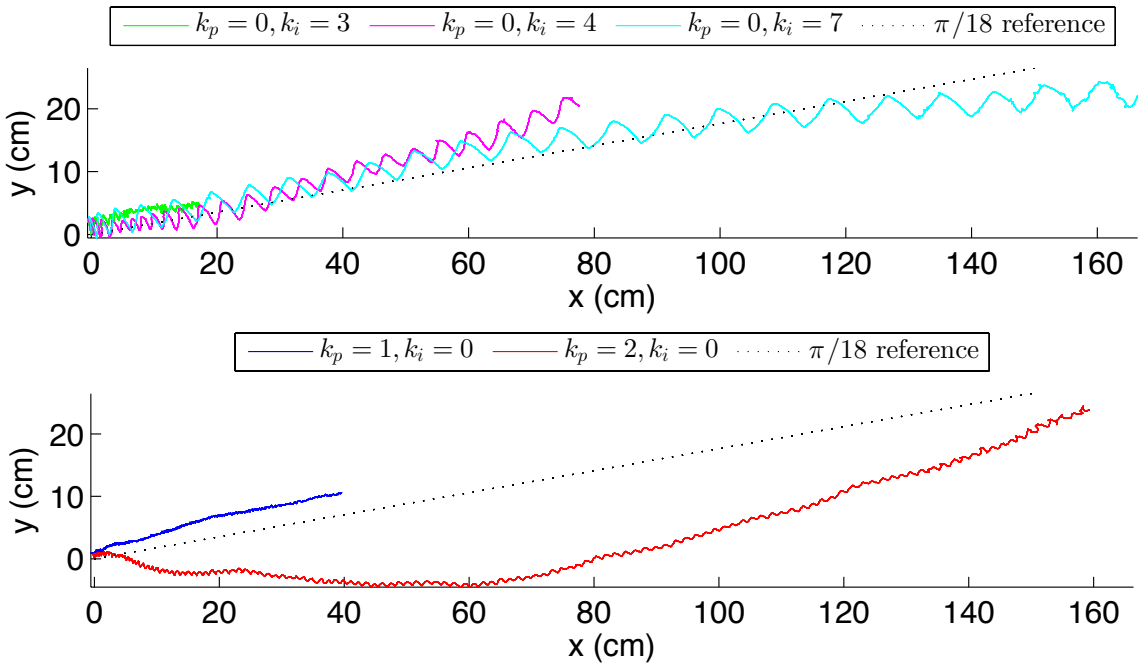

Figure 3: Swimming trajectories obtained as byproducts of heading control using purely integral (top) or purely proportional (bottom) feedback.

bring the foil in contact with the opposite end of the pool. Both panels show that different gains yield different swimming speeds. Gradual drift is apparent in the foil's heading, particularly in the case of purely integral control; this drift is an artifact of both numerical error in the integration of the angular velocity and bias in the sensor.

Fig. 4 depicts heading data corresponding to the trajectory data of Fig. 3. It's apparent that purely integral control engenders forward propulsion more reminiscent of the swimming of fish, whereby the nose of the foil repeatedly overshoots its average heading to a substantial degree as the foil moves forward. Purely proportional control (with the chosen gains) engenders higher-frequency vibrations in heading that contribute to the observed drift in gyrometer measurements.

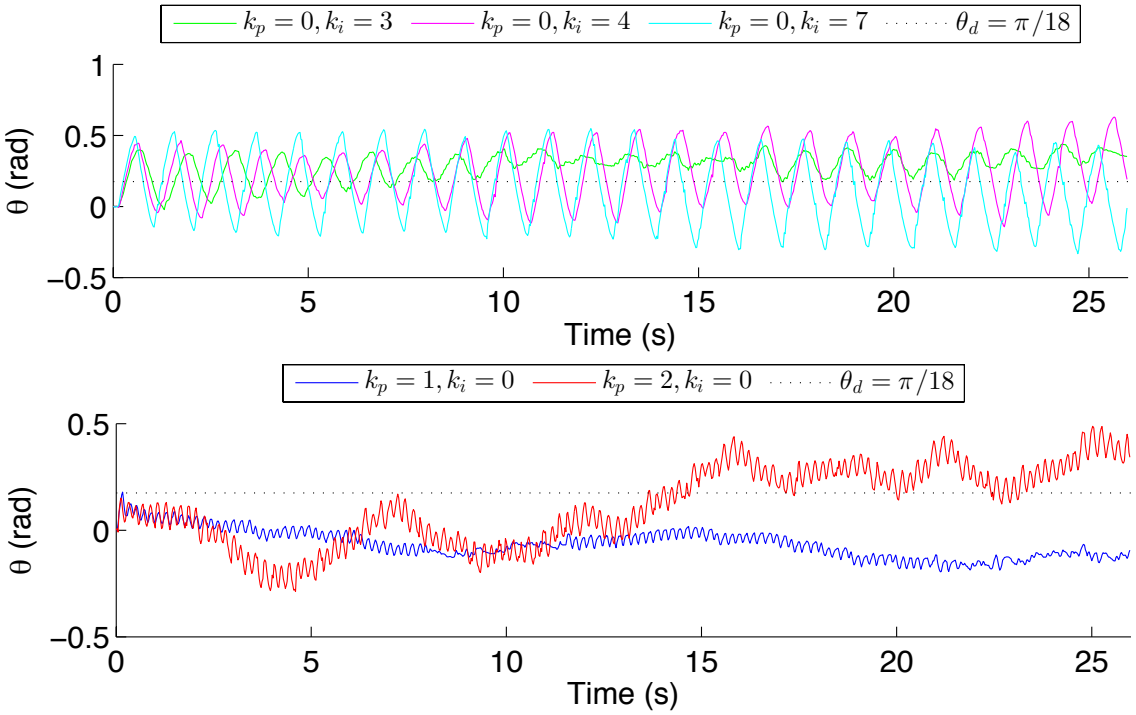

Figure 4: Heading data corresponding to the trajectories shown in Fig. 3.

2.3 Damping-Induced Heading Recovery

2.3.1 Modeling

For the remainder of this chapter, we concern ourselves with the dynamics and control of the foil's heading alone, and not with the propulsion that results from varying this heading. It might seem that the most straightforward way to reorient the foil permanently — say, clockwise, decreasing θ from zero to a negative constant over a certain period of time — would be to spin the rotor in the opposite direction until the desired reorientation had been achieved, and then to discontinue actuation. A fundamental obstacle to this strategy is present in the mechanics of the system, however, that results from the viscous drag exerted on the foil by the water. This can be illustrated concretely as follows.

Fig. 5 depicts a smooth bump function of the form

$$b(w,t) = \begin{cases} \exp\left(\frac{a^2}{a^2-1}\right) & 0 < t < w \\ 0 & \text{otherwise} \end{cases} \tag{1}$$

where

$$a = \frac{2t}{w} - 1.$$

If $\dot{\phi}$ is set equal to $b(w,t)$, the rotor will accelerate smoothly from rest to a maximum angular velocity of 1 rad / s counterclockwise and then decelerate symmetrically, coming to rest (relative to the foil) at $t = w$. For every simulation described in this section, $\dot{\phi}$ corresponds to a linear combination of such functions.

In the absence of dissipation, the rotational dynamics of the foil and rotor together are governed by the conservation of total angular momentum. If F and B denote the effective rotational inertias of the foil and rotor, respectively, then this conservation law is equivalent to the differential equation

$$F\ddot{\theta} + B(\ddot{\theta} + \ddot{\phi}) = 0.$$

The form of this equation is unchanged by the fact that the effective inertia of the foil may include added inertia inherited from the surrounding fluid. The top panel in Fig. 6 depicts the variations in θ and ϕ that occur over time when $\theta = \dot{\theta} = \phi = 0$ initially, $\dot{\phi}$ is given by the bump function shown in Fig. 5, F and B are assigned the (arbitrary) values

$$F = 1 \text{ kg m}^2, \quad B = 5 \text{ kg m}^2,$$

and dissipation is absent from the system. Not surprisingly, spinning the rotor coun-

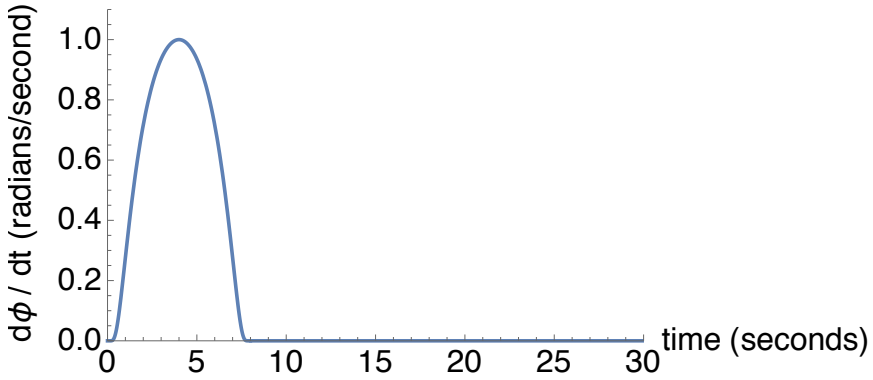

Figure 5: Relative counterclockwise rotor speed corresponding to the three simulations represented in Fig. 6, given by (1) with w equal to eight seconds.

terclockwise relative to the foil induces the foil to rotate clockwise, and the foil ceases to rotate when actuation is discontinued.

The introduction of damping to the system in the form of dissipative resistance to the foil's rotation doesn't merely attenuate the extent to which spinning the rotor will counter-rotate the foil. The hydrodynamic forces acting on a real rotating hydrofoil are complicated, and have high-order dynamics associated with vortex shedding and wake-body interactions (modeled computationally in [48]), but a primitive model can be obtained by focusing on the components of rotational drag that are linear or quadratic in rotational speed. In the presence of these, the conservation of angular momentum is superseded by the evolution equation

$$F\ddot{\theta} + B(\ddot{\theta} + \ddot{\phi}) = -\mu\dot{\theta} - \nu\dot{\theta}^2, \tag{2}$$

where μ and ν are positive constants.

The "self-recovery" phenomenon documented in [9, 10, 11] arises in the present context when μ is nonzero. The middle panel in Fig. 6 depicts the response in the

foil's orientation to the same rotor motion depicted in the preceding panel when $\nu = 0$ but $\mu = 2$ kg m^2 / s. Initially, the foil counter-rotates in response to the spinning of the rotor, but once the rotor is brought to rest relative to the foil, the foil's heading returns all the way to its initial value. This behavior isn't specific to our choice of rotor motion: it's straightforward to show (using the final value theorem) that following any sequence of actuation that's bounded in time, θ will return asymptotically to its initial value. The asymptotic value of θ can't be altered through any finite-time sequence of actuation when drag linear in $\dot{\theta}$ — viscous drag — is present but additional nonlinear drag is not.

When both viscous drag and nonlinear drag act on the foil, heading recovery occurs only partly, but can still be substantial. We demonstrate this experimentally in section 2.3.2[2], but the inclusion of quadratic drag in (2) is sufficient to engender the phenomenon of partial recovery. The bottom panel in Fig. 6 depicts the response in the foil's orientation to the same rotor motion depicted in the preceding panels when $\mu = 2$ kg m^2 / s and $\nu = 1$ kg m^2. The angle θ reaches a minimum of -2.04 radians and then recovers to -0.597 radians.

Damping-induced heading recovery can represent a substantial obstacle to simple motion control for an aquatic vehicle, and one objective of the present work is to identify a strategy for attenuating its influence. Such a strategy is suggested by Fig. 7, which depicts the outcome when — in the presence of both viscous and quadratic damping, parametrized as before — the rotor is spun up and down thrice rather than

[2]A physical demonstration that predates the present work is also visible at `http://tinyurl.com/ojoojj8`.

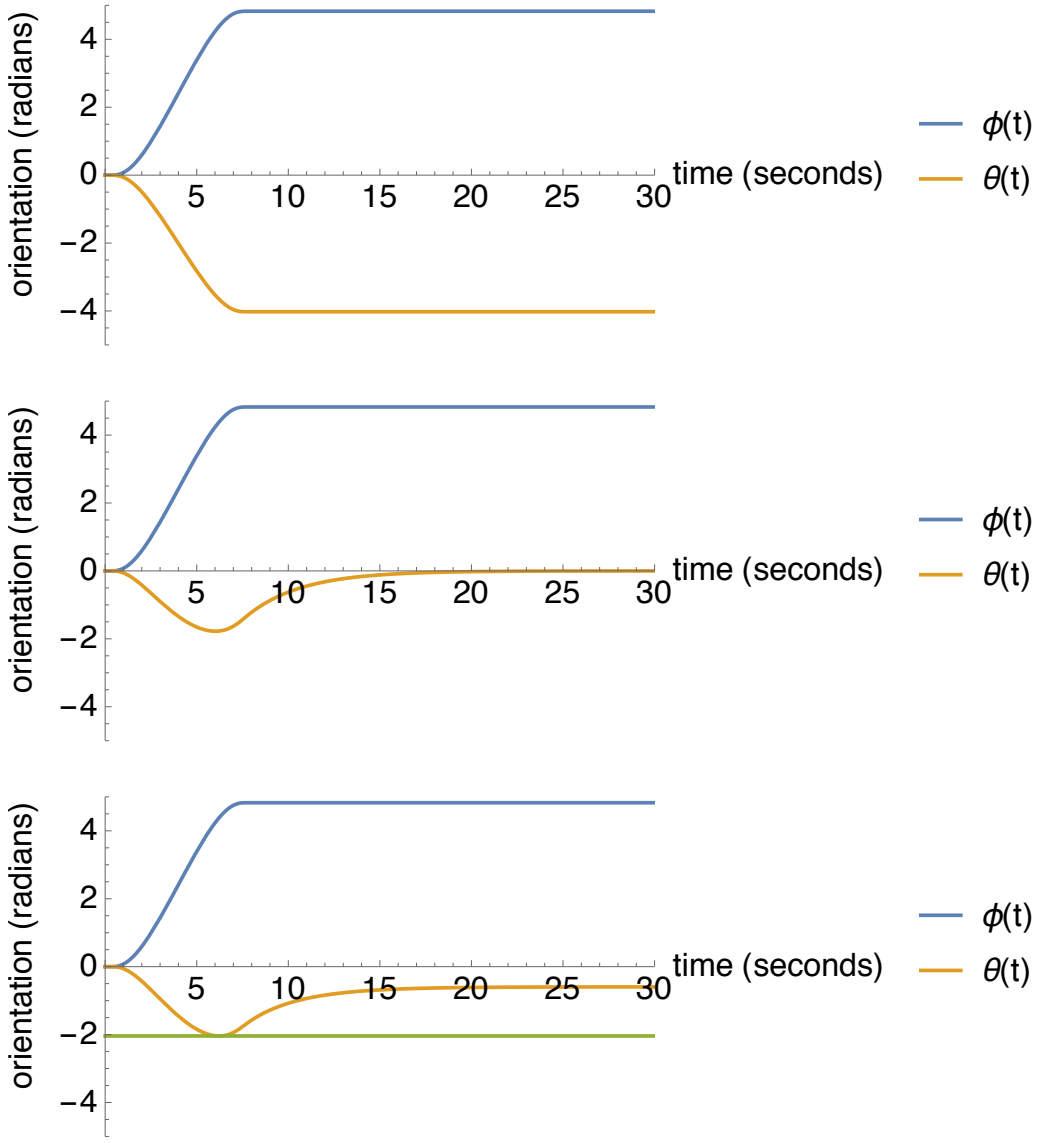

Figure 6: Rotor orientation and foil orientation over time when the rotor's relative counterclockwise speed is as shown in Fig. 5 and damping is absent (top), exclusively linear in the foil's rotational speed (middle), or partly linear and partly quadratic in the foil's rotational speed (bottom).

once in the same window of time, to a degree selected so that the foil is reoriented to the same extreme ($\theta = -2.04$ radians) before actuation is ceased. Subsequent recovery of the foil's heading (now to $\theta = -0.763$ radians) is diminished by more than ten percent. We infer that when nonlinear drag is present, damping-induced heading recovery may be curtailed by actuating the rotor to reorient the foil in a stepwise, rather than monotonic, fashion. We stress that this isn't true when drag is absent from the system (in which case no recovery occurs) or when only viscous drag is present (in which case complete recovery occurs) — both cases that can be treated analytically for arbitrary rotor motions.

2.3.2 Experiments

Using the same test setup as for the experiments in section 2.2, the system was programmed to rotate the rotor at a constant speed for a specific amount of time and then to terminate actuation. The heading angle θ was measured during the rotor's motion and thereafter to document damping-induced recovery.

Fig. 8 depicts the outcome of one such experiment. The angular velocity of the rotor was set to -5.9 rad/s for fifteen seconds and then to zero for seventy-five seconds more; the foil's heading increased while the rotor was spinning and then returned to its initial value thereafter. The data actually show an overshoot in the foil's heading after recovery, but this was apparently due to persistent excitation of the water (confined by nearby rigid boundaries) following the foil's initial motion. Fig. 9 shows the trajectories followed by markers at the center of the rotor and the tail of the foil during this experiment. These two points are used to obtain the foil's heading. The

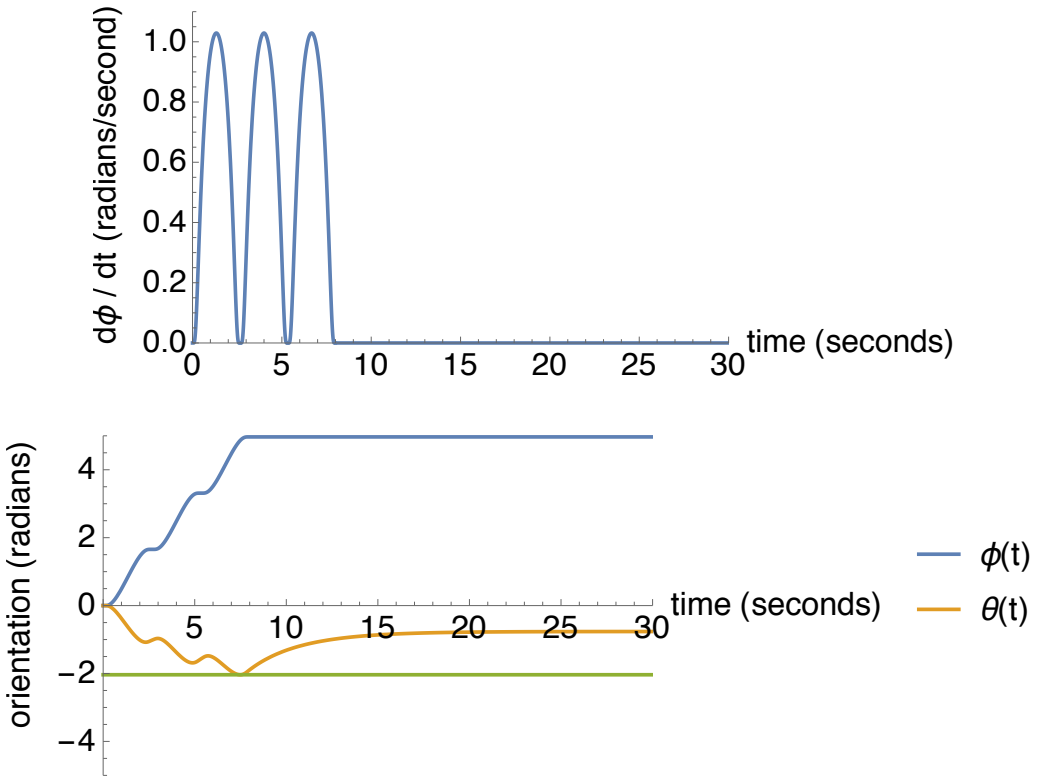

Figure 7: Relative counterclockwise rotor speed (top) and rotor and foil orientation (bottom) demonstrating a 12% decrease in heading recovery compared to the bottom panel in Fig. 6 under the same parametric conditions. The minimum value of θ is -2.04 radians in both cases, indicated with a green line for visual comparison.

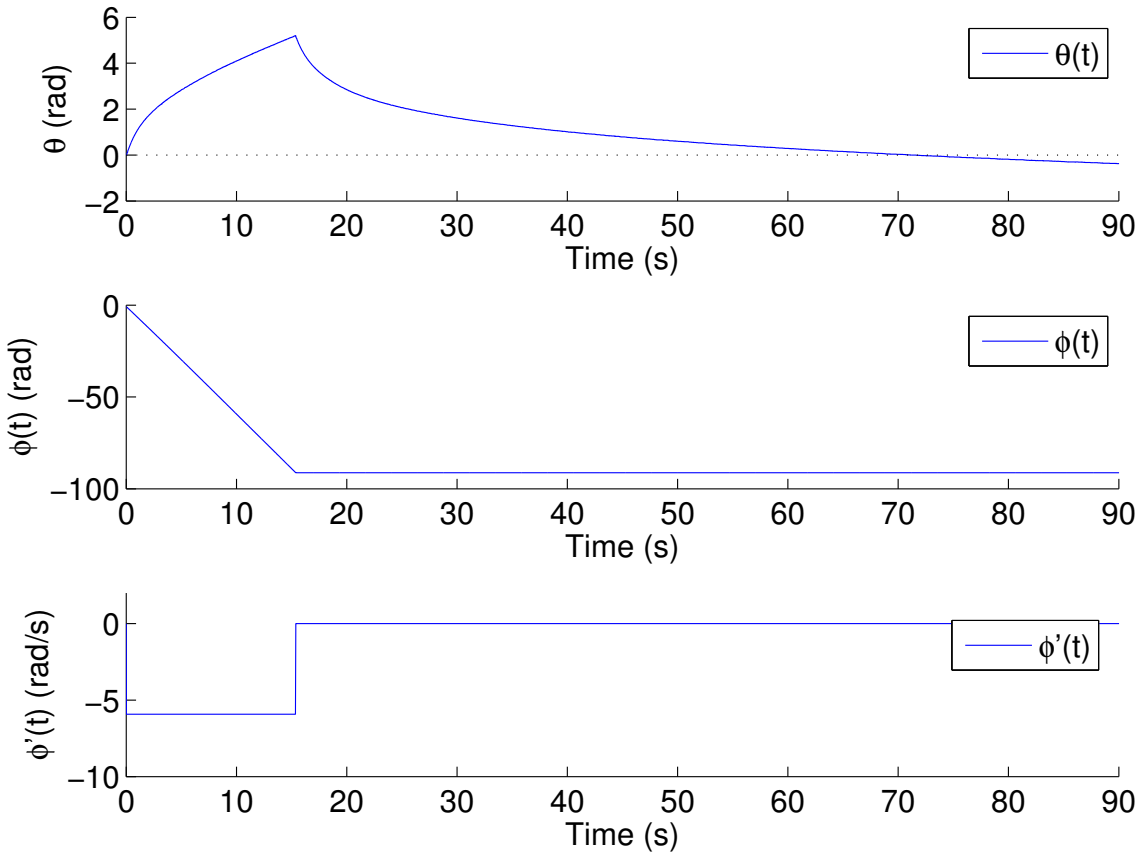

Figure 8: Foil heading (top) as a function of time, exhibiting recovery after the rotor is spun for fifteen seconds at a constant speed relative to the foil and then stopped. The rotor's relative orientation (middle) and relative counterclockwise speed (bottom) are also shown.

green and red arrows indicate the initial and final positions of the foil, respectively; each arrow points from the foil's tail to the center of the rotor.

Figs. 10 and 11 depict the outcome of a second experiment in which the rotor was spun for forty seconds and then stopped. Heading recovery is clearly partial in this case; the angle θ increased from zero to 11.4 radians during actuation and then recovered 43% to 6.5 radians thereafter.

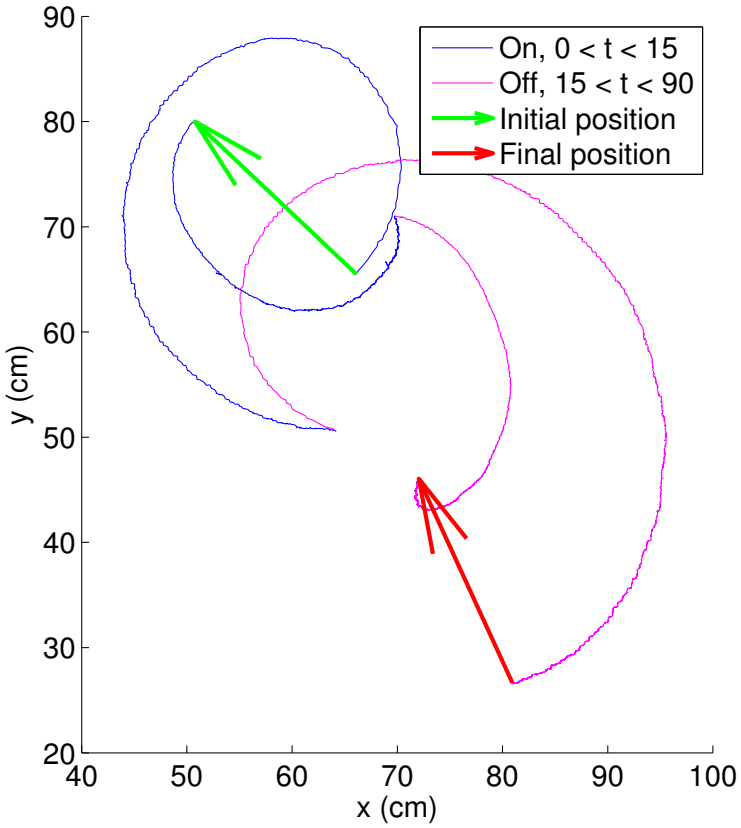

Figure 9: Trajectories of the center of the rotor and the rear of the foil corresponding to the data in Fig. 8.

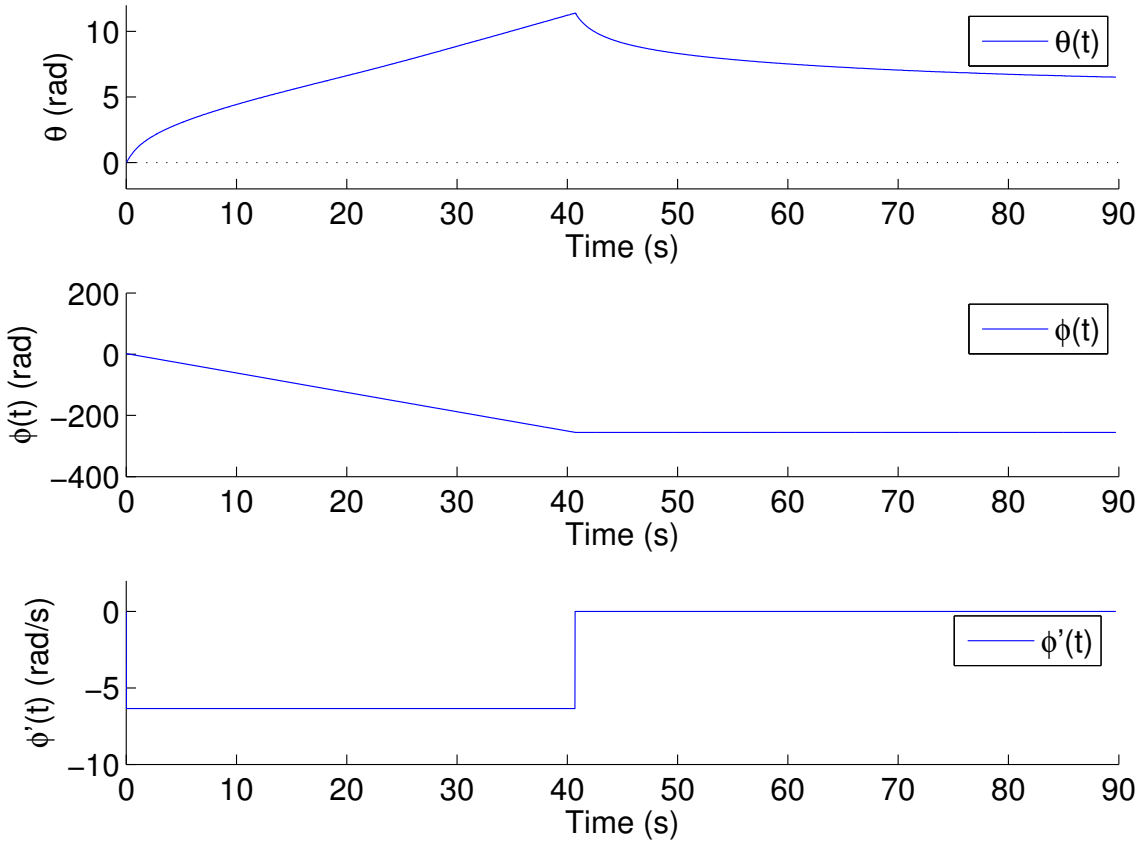

Figure 10: Foil heading (top) as a function of time, exhibiting partial recovery after the rotor is spun for forty seconds at a constant speed relative to the foil and then stopped. The rotor's relative orientation (middle) and relative counterclockwise speed (bottom) are also shown.

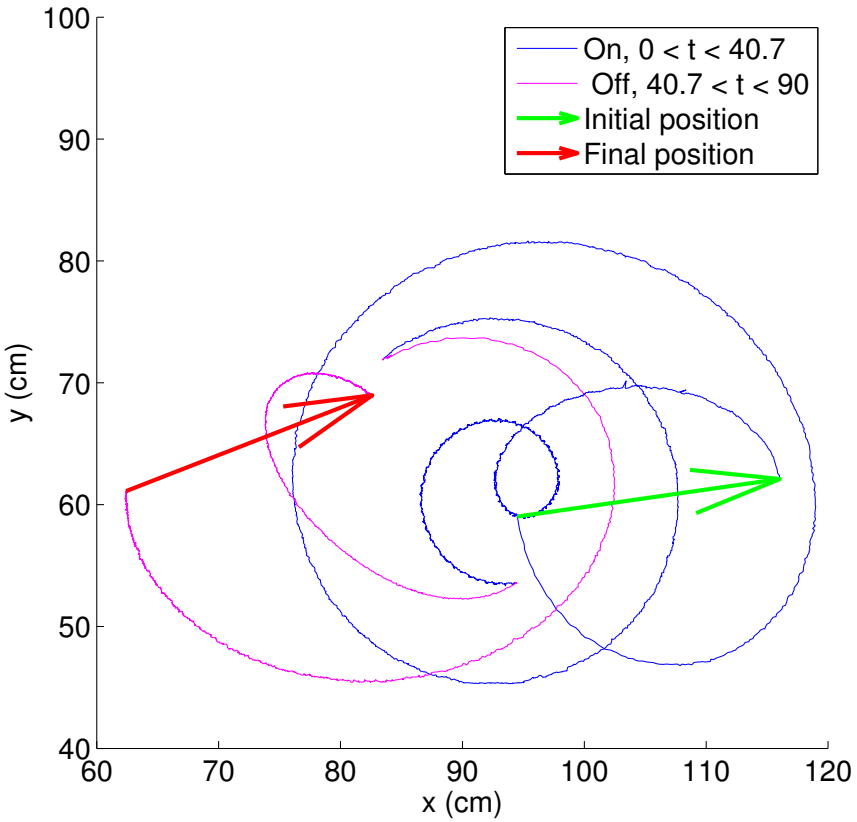

Figure 11: Trajectories of the center of the rotor and the rear of the foil corresponding to the data in Fig. 10.

2.4 Discussion

The system considered is worthy of study partly because of its simplicity. Problems concerning the coupling of steering to propulsion or the influence of damping on heading control are common to many aquatic vehicles; the present system isolates these in a uniquely elemental setting. Because the system isn't merely underactuated but *singly* actuated, its dynamics include no component attributable to *geometric phase*, which plays a substantial role in certain forms of aquatic locomotion [27]. This work considers for the first time the notion of partial heading recovery in the presence of a mixture of linear and nonlinear damping. Our treatment of control in the presence of this phenomenon has been preliminary; we conclude by highlighting an additional relevant feature of systems with nonlinear damping.

The movie linked in the last footnote illustrates a mechanical corollary to the principle of damping-induced recovery. When the rotor atop the foil in the movie is spun at a constant speed for a relatively long time in one direction, the foil doesn't counter-rotate at a constant speed, but instead counter-rotates with decreasing speed, approaching a state in which the foil's orientation is constant despite ongoing actuation. This behavior was *not* exhibited by the physical system depicted in Fig. 1 in the course of performing experiments for this work. The two systems are essentially the same in design but differ in size and mass. We have yet to document the conditions under which this sort of saturation does or doesn't occur in the laboratory, but the simplified model (2) suggests the roles played by inertia and damping.

Suppose that the modeled system from Section 2.3.1 is initially at rest with F, B

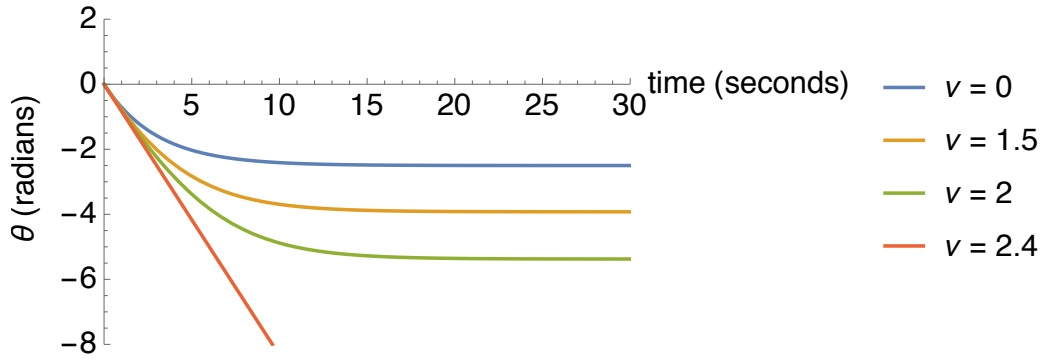

Figure 12: Saturation in the foil's heading in response to constant spinning of the rotor with $\dot{\phi} = 1$ rad / s for positive time. The system is assumed to have been at rest prior to actuation. The parameters F, B, and μ assume the same values as in the lower two panels of Fig. 6 and in Fig. 7. Each curve corresponds to a different degree of quadratic damping in the system; ν is measured in kg m^2.

and μ assigned the values represented in the lower two panels in Fig. 6 and in Fig. 7. Now suppose that the rotor is driven so that $\dot{\phi}$ is a step function with magnitude k. Fig. 12 depicts the outcome when $k = 1$ rad / s and ν assumes four different values (measured in kg m^2).

In the absence of nonlinear damping, the system exhibits the saturation phenomenon described above and θ approaches -2.50 radians asymptotically over time. The introduction of nonlinear damping doesn't initially disrupt the system's tendency to saturate, but increases the discrepancy between the initial and asymptotic values of θ. If ν is increased beyond a critical value, however, persistent spinning of the rotor enables persistent counter-rotation of the foil.

Fig. 13 clarifies the transformation that occurs with a trio of phase portraits. The premise that the system is at rest before the rotor begins to spin requires that $\dot{\theta} = -kB/(F + B)$ initially (when the step input becomes nonzero). The system's

initial condition is indicated with a black dot in each phase portrait; saturation occurs if the trajectory passing through this point approaches the horizontal axis in forward time.

The top panel in Fig. 13 corresponds to the case in which $\nu = 0$. The vector field with components $(\dot{\theta}, \ddot{\theta})$ has constant slope throughout the phase plane — vectors in the upper half plane (not shown) are anti-parallel to vectors in the lower half-plane — and saturation occurs from every initial condition. The middle panel corresponds to the case in which $\nu = 2$ kg m^2. All the initial conditions shown in the lower half-plane lead to saturation, but the upward component of the phase flow diminishes with distance from the horizontal axis. The bottom panel corresponds to the case in which $\nu = 4$ kg m^2. The vertical component of the phase flow reverses sign along the horizontal line $\dot{\theta} = -\mu/\nu = -0.5$ rad / s, and saturation occurs when the system begins at rest (prior to actuation) because the initial condition indicated with a black dot lies below this line. The criterion for saturation with this initial condition is

$$kB\nu < (F + B)\mu.$$

Note that heading saturation of this kind need not be considered a liability. It can always be overcome with a more sophisticated choice of control, and it can be exploited to advantage when the control objective is to approach a certain heading without overshoot.

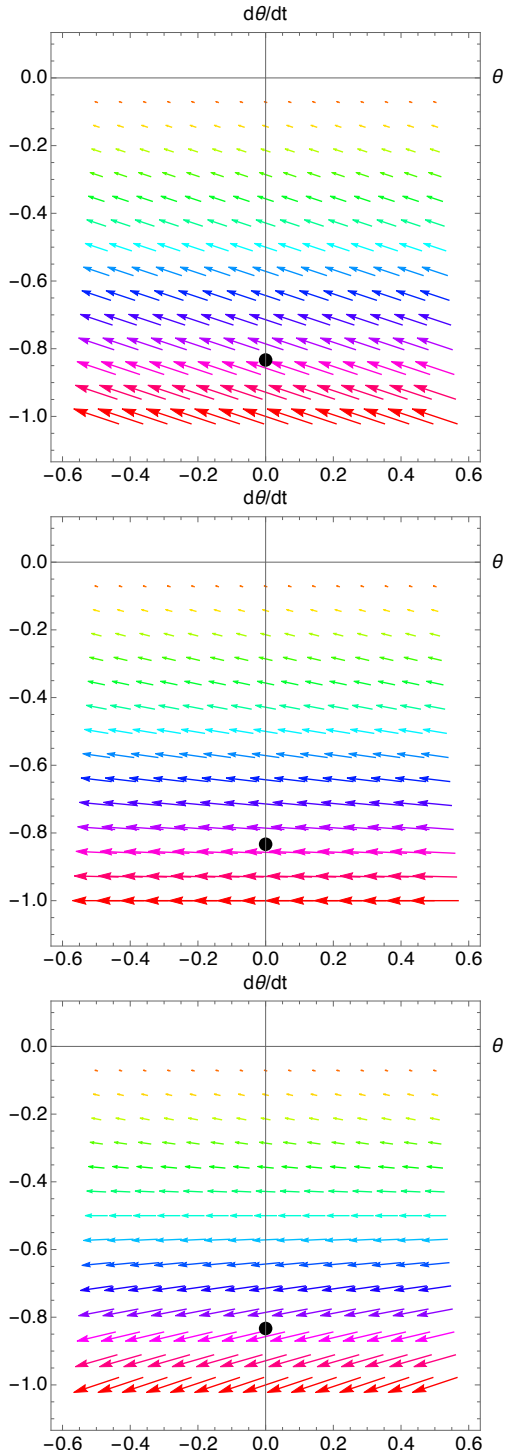

Figure 13: Phase portraits derived from (2) that clarify whether or not the system with zero angular momentum prior to actuation will approach the saturated state $\dot{\theta} = 0$ once the rotor is spun counterclockwise with constant unit speed. In all three cases, F, B, and μ assume the same values as in the lower two panels of Fig. 6 and in Fig. 7. The top, middle, and bottom panels correspond to $\nu = 0$, 2, and 4 kg m^2, respectively.

CHAPTER 3: THE CHAPLYGIN BEANIE — AN ANALOG TO THE HYDROFOIL WITH INTERNAL ROTOR

3.1 Introduction

Control laws that mimic passive physical phenomena are employed in diverse mechanical settings. An actuator that applies a force proportional to the deviation in a mechanical element's measured position from a desired value, for instance, can be considered to act as a linear spring. Mechanical analogies in turn motivate a variety of control designs. Successful strategies for the coordination of multi-vehicle systems, for instance, have been developed whereby individual vehicles respond to movement relative to their neighbors as if linked to these neighbors by linear springs and dampers [38]. Real physical coupling can also complement deliberate control in the context of coordination. Systems of aerial or aquatic vehicles that seek states of motion mimicking bird flocks or fish schools, for instance, may do so using feedback control but may benefit from the local attractiveness of states that represent local energetic minima [39, 31]. The tendency for physically coupled nonlinear systems to synchronize may be so strong as to overcome contrary regulation at the individual level — a point observed as early as Huygens' experiments with synchronizing pendulum clocks in the 1660s [5].

The system depicted in Fig. 14 was introduced in [24] and named the *Chaplygin beanie* because it combines elements of two canonical systems from the mechanics

literature: the *Chaplygin* (or *Carathéodory*) *sleigh* (essentially a modern shopping cart, supported in the front by casters and in the rear by one or more wheels that roll without slipping [6]) and *Elroy's beanie* (a rigid body coupled through an actuator to a balanced rotor surmounting its center of mass [33]). It was demonstrated analytically in [24] that this system will translate from rest if the rotor is induced to spin relative to the cart, and that a simple proportional control law mimicking the action of a torsional spring on the rotor can be used to dictate the cart's asymptotic heading and longitudinal speed simultaneously. An analogy was also developed between this system and a planar fishlike swimmer, each able to propel itself by exploiting a resistance to lateral motion at its rear through periodic variations in angular momentum forward of this resistance. A more direct analogy obtains between the Chaplygin beanie and the aquatic vehicle studied subsequently in [48], consisting of a rigid planar hydrofoil with an internal balanced rotor.

In section 3.2, a physical realization of the system in Fig. 14 is presented and used to validate the control approach suggested in [24]. In section 3.3, a strategy is outlined to generalize this approach to the problem of coordinating the orientation and translational speed of two or more Chaplygin beanies. In section 3.4, numerical results are presented that document a surprising phenomenon whereby a passive Chaplygin beanie with a torsional spring in place of an actuator will reorient itself and follow a self-propelling Chaplygin beanie when the two are supported by a common platform through which vibrational energy can be transmitted. Entrainment of this kind is patently analogous to the synchronization of pendulum clocks sharing vibrational energy through a common mantel, but is also arguably analogous to a

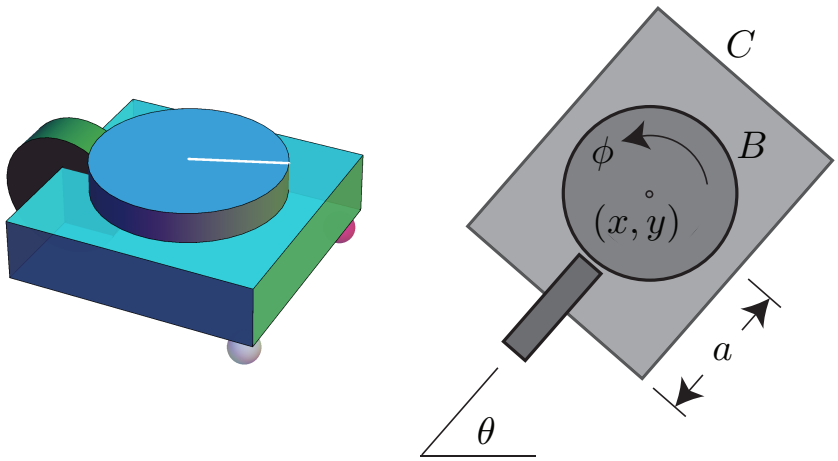

Figure 14: The Chaplygin beanie. The position of the cart's center of the mass and the orientation of the cart relative to a stationary frame of reference are specified by (x, y) and θ, respectively. The rotational inertias of the rotor and cart relative to their point of coupling at the cart's center of mass are denoted by B and C, respectively. The mass of the system overall is denoted by m in the text. The rotational inertia of the rear wheel, which can roll freely but cannot slip laterally, is considered to be negligible.

form of entrainment that occurs within schools of fish that exchange kinetic energy through wake vorticity. A dramatic illustration of the latter is documented in [4]: the flexible body of a dead fish can be induced to swim against a background current toward a bluff object upstream when excited by vorticity shed periodically from the object. The entrainment documented in section 3.4 is interesting in its own right as a new example of unexpected behavior engendered by nonholonomic constraints — the spin reversal of the rattleback is a classic, contrasting example [6] — but may also suggest a future strategy for coordinating the motion of systems of underactuated vehicles like the Chaplygin beanie through decentralized control.

3.2 Singe-Vehicle Dynamics and Control

3.2.1 Analysis

The dynamics of the system shown in Fig. 14, with a torque inducing the rotor to rotate relative to the cart serving as the solitary control input, are those of a control-affine system with drift. The configuration manifold $\mathbb{S}^1 \times \mathrm{SE}(2)$ is four dimensional, but the constraint

$$-\dot{x}\sin\theta + \dot{y}\cos\theta = a\dot{\theta}$$

prohibiting lateral slipping of the rear wheel on the ground decreases the dimension of the system's phase space by one. The machinery of nonholonomic reduction [7] was employed in [24] to isolate the dynamics of the two-dimensional nonholonomic momentum with scalar components

$$J_{LT} = m\dot{x}\cos\theta + m\dot{y}\sin\theta,$$

$$J_{RW} = -m\dot{x}a\sin\theta + m\dot{y}a\cos\theta + (B+C)\dot{\theta} + B\dot{\phi}$$

representing, respectively, the system's forward translational momentum and its angular momentum relative to a vertical axis passing through the center of the rear

wheel. The system's drift dynamics are given overall by

$$\begin{aligned}
\dot{x} &= \frac{J_{LT}}{m}\cos\theta - a\left(\frac{J_{RW}-B\alpha}{ma^2+B+C}\right)\sin\theta \\
\dot{y} &= \frac{J_{LT}}{m}\sin\theta + a\left(\frac{J_{RW}-B\alpha}{ma^2+B+C}\right)\cos\theta \\
\dot{\theta} &= \frac{J_{RW}-B\alpha}{ma^2+B+C} \\
\dot{J}_{LT} &= ma\left(\frac{J_{RW}-B\alpha}{ma^2+B+C}\right)^2 \\
\dot{J}_{RW} &= -a\left(\frac{J_{RW}-B\alpha}{ma^2+B+C}\right)J_{LT} \\
\dot{\phi} &= \alpha.
\end{aligned} \tag{3}$$

Normalizing with respect to the rotational inertia of the rotor, we can consider the rotor's angular acceleration $\dot{\alpha}$ to be under direct control.

A fundamental obstacle to local controllability is present in (3). The forward momentum J_{LT} is nondecreasing, and any change in the cart's heading is necessarily accompanied by an increase in this momentum.[3] Nevertheless, if the system is initially at rest, then it's possible to induce the cart to accelerate using a simple proportional controller so that its heading and translational speed — to wit, θ and J_{LT} — will approach any desired values asymptotically. Without loss of generality, the desired asymptotic value of θ can be taken to be zero. It's shown in [24] (essentially via LaSalle's invariance principle) that the feedback law $\dot{\alpha} = k\theta$ will drive θ to zero for any positive value of the gain k. The closed-loop system will evolve, furthermore, so that the energy-like quantity

$$\Lambda = \frac{(J_{RW}-B\alpha)^2}{ma^2+B+C} + \frac{J_{LT}^2}{m} + kB\theta^2$$

[3] With appropriate magnitude, a sinusoidal torque on the rotor will induce the system to accelerate from rest in an undulatory fashion. A movie of this is visible at `http://tinyurl.com/gm4h2nh`.

is conserved over time. It follows that

$$\lim_{t\to\infty} J_{LT}^2 = m\Lambda(0) = D + kF, \tag{4}$$

where

$$D = m\frac{(J_{RW}(0) - B\alpha(0))^2}{ma^2 + B + C} = m(ma^2 + B + C)\dot{\theta}(0)^2$$

and

$$F = mB(\theta(0))^2.$$

If $\theta \neq 0$ and $\dot{\theta} = 0$ initially, then k can be selected to assign any positive value to $\lim_{t\to\infty} J_{LT}$. If $\theta \neq 0$ but $\dot{\theta} \neq 0$ initially, then k can be selected to assign any positive value to $\lim_{t\to\infty} J_{LT}$ that's greater than a certain lower bound.

3.2.2 Experimental Results

Fig. 15 depicts a physical realization of the Chaplygin beanie. This system's dynamics deviate from those of the model (3) principally because of friction associated with the rear wheel, resisting both pivoting of the cart (due to friction between the wheel and the ground) and forward rolling (due to friction in the bearings between the cart and the wheel). We demonstrate experimentally that if the system in Fig. 15 is initially at rest and its rotor is driven thereafter according to a feedback law akin to $\dot{\alpha} = k\theta$, then the heading angle θ will approach zero over time and the cart's forward speed will approach a value that increases with increasing k.

The controller we implement is merely "akin to" the proportional controller from section 3.2.1 in two practical ways. First, the actuator coupling the rotor to the

Figure 15: A physical Chaplygin beanie constructed primarily from one inch–thick extruded polystyrene foam. In place of casters, the aluminum pie plates hover on cushions of air generated by counter-rotating ducted fans to support the forward end of the cart with minimal friction between the cart and the ground. Batteries contribute significantly to the inertia of the cart; the rotor's large diameter helps to increase its rotational inertia without increasing the system's mass overall.

cart is a small brushed DC gearmotor[4] powered by a pulse-width modulated (PWM) input voltage. The feedback gain k multiplies the cart's heading to determine not the motor torque directly but the duty cycle of the PWM signal. Second, limitations on the speed and torque available from the motor confine our experiments to a regime in which friction plays a visible role. One way to overcome the cart's tendency to lose forward momentum while stabilizing its heading is to increase its tendency to overshoot this heading, since oscillations in heading generate a propulsive force according to the third and fourth lines in (3). We therefore augment the proportional feedback of section 3.2.1 with an integral feedback term to increase overshoot, scaling the integral gain with the proportional gain from one experiment to the next.

It's expected that future versions of the physical apparatus in Fig. 15 will permit experiments involving more aggressive maneuvers that downplay the short-term influence of friction, obviating the need for integral feedback. On the other hand, it's expected that additional experiments with the current apparatus will contribute new understanding to the phenomenon of *damping-induced heading recovery*, a manifestation of damping-induced self-recovery [9] documented in the context of dissipative aquatic locomotion in [23].

Figure 16 depicts the results of three different experiments with the system from Fig. 15. In each experiment, feedback linking the angular acceleration of the rotor to the cart's heading induces the cart to execute a right-angle turn. The translational speed attained by the cart in doing so increases with increasing gain.

[4] `https://www.pololu.com/product/2386`

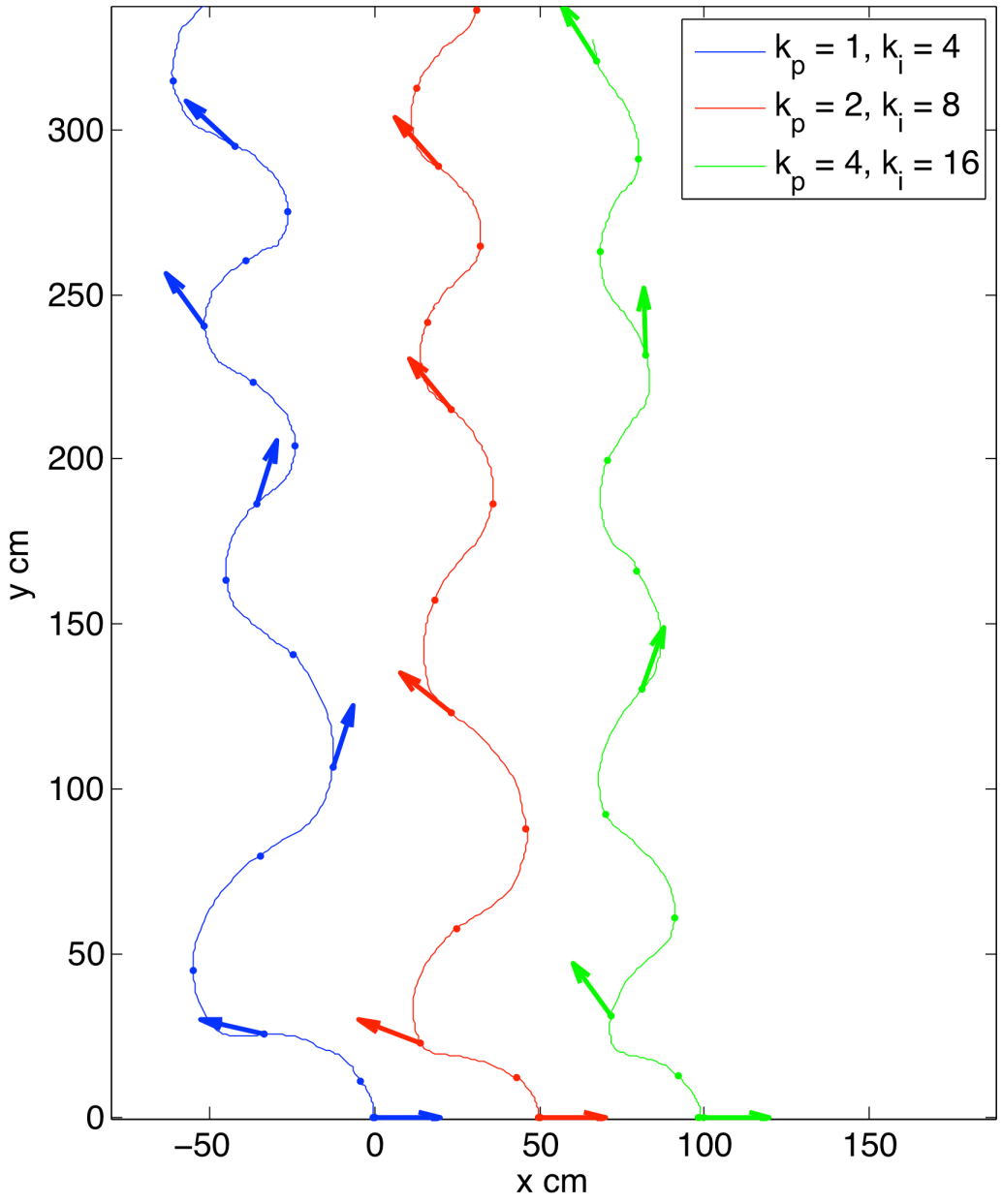

Figure 16: Trajectories of the physical Chaplygin beanie under the influence of three different heading controllers. In each case, the cart is initially centered at rest along the x axis and pointing in the positive x direction. A PI controller is activated to stabilize the heading to the positive y direction, resulting in forward locomotion as well as rotation. The dots along the trajectories represent equal intervals of time, showing that an increase in feedback gain results in an increase in the cart's translational speed. The desired average heading is eventually achieved in every case. A movie depicting an experiment in this series is visible at `http://tinyurl.com/z6vcegc`.

3.3 Heading and Speed Coordination

Imagine two identical Chaplygin beanies at rest, situated so that their initial headings differ. If proportional heading control is applied to each to steer it toward the initial average heading of the two, and if the same gain k is used in both feedback loops, then the two will approach a state asymptotically in which they translate in the same direction at the same speed. The quantity

$$\begin{aligned}\Lambda_{\text{decoupled}} =& \frac{(J_{RW1} - B\alpha_1)^2 + (J_{RW2} - B\alpha_2)^2}{ma^2 + B + C} \\ &+ \frac{J_{LT1}^2 + J_{LT2}^2}{m} + kB\left(\theta_1^2 + \theta_2^2\right)\end{aligned}$$

will be conserved as their dynamics evolve, furthermore, even if their initial average heading doesn't correspond to $\theta = 0$.

An alternative strategy for coordinating the asymptotic heading and speed of the two vehicles is to implement the pair of control laws

$$\dot{\alpha}_1 = k(\theta_1 - \theta_2), \quad \dot{\alpha}_2 = k(\theta_2 - \theta_1) \tag{5}$$

so that each vehicle attempts to stabilize its heading to that of the other as the two headings evolve. A comparison of the two strategies appears in Fig. 17. Using the same shared gain k in both cases, the second strategy results in more rapid convergence to the system's final state. In the second case, the quantity

$$\begin{aligned}\Lambda_{\text{coupled}} =& \frac{(J_{RW1} - B\alpha_1)^2 + (J_{RW2} - B\alpha_2)^2}{ma^2 + B + C} \\ &+ \frac{J_{LT1}^2 + J_{LT2}^2}{m} + kB(\theta_1 - \theta_2)^2\end{aligned}$$

is conserved. The quantities $\Lambda_{\text{decoupled}}$ and Λ_{coupled} differ in the "potential energy" terms that reflect the sense in which the control torques on the two rotors may be associated metaphorically with torsional springs.

Recall from (4) that the final translational speed of a solitary Chaplygin beanie subject to proportional heading control depends on both the feedback gain and the initial error in its heading. Because of this, any number of such vehicles with distinct initial headings can be induced to approach any common heading and translational speed asymptotically through separate control. Though the details aren't presented here, it is proposed that a set of feedback laws interconnecting the dynamics of a collection of such vehicles in a manner that generalizes (5) can always be constructed to achieve the same objective, potentially more efficiently, based on the shaping of a potential energy–like term involving a distribution of gains.

3.4 Vibrational Entrainment

Again imagine two identical Chaplygin beanies at rest, each situated and oriented arbitrarily. Suppose that the rotor atop one cart is actuated but the rotor atop the other is coupled to the cart beneath through a linear torsional spring. Suppose, furthermore, that the two vehicles rest atop a common platform that isn't rigidly fixed but instead exhibits translational compliance with finite inertia. It's clear from the analysis of section 3.2.1 that if the rotor atop the first cart is induced to pivot sinusoidally, then the cart will advance relative to the platform, exerting a time-varying force on the platform that will induce the platform to move as well. It's also relatively clear that if the platform begins to vibrate, this will induce the second cart

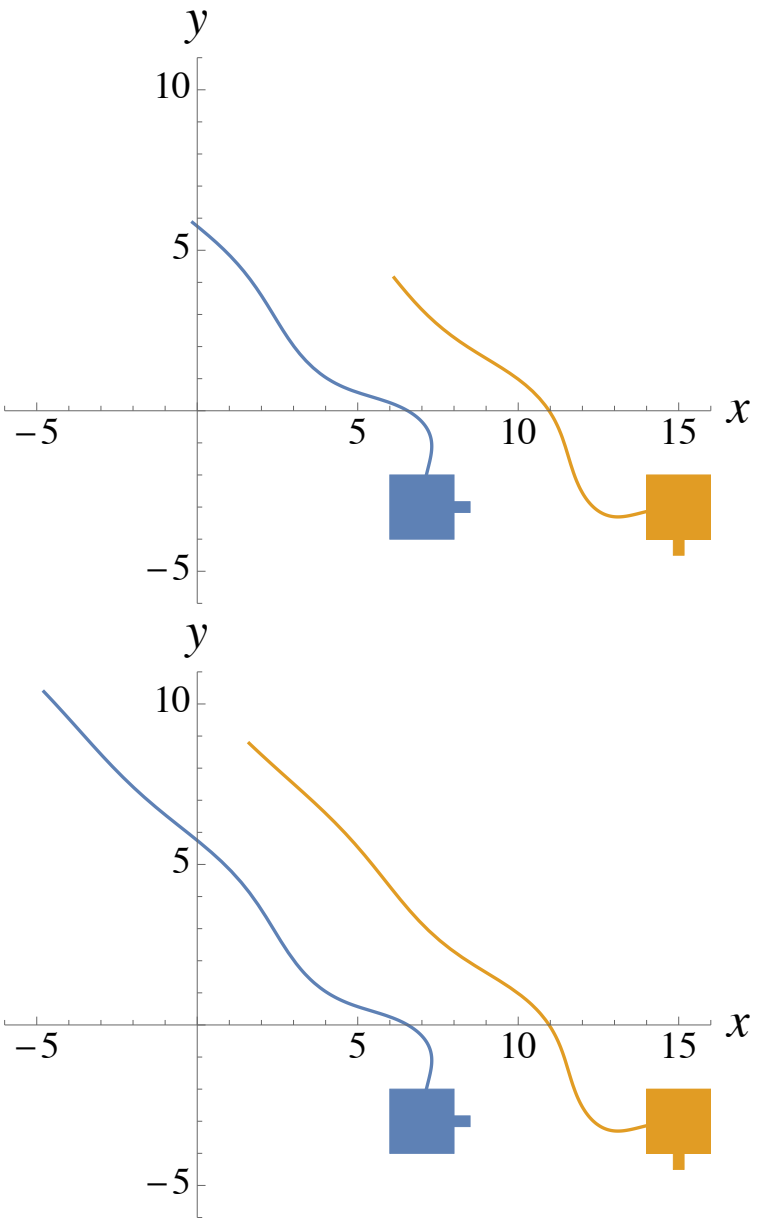

Figure 17: Trajectories of two Chaplygin beanies subject to proportional control stabilizing their headings to a common value. The top panel depicts the pair's response to the decoupled control laws $\dot{\alpha}_i = k(\theta_i - \theta_{\text{desired}})$, the bottom panel to the control laws (5). Both panels correspond to the interval $0 < t < 20$ and $m = a = B = C = k = 1$ for both vehicles.

to pivot about its rear wheel, in turn exciting the second rotor to oscillate, stimulating forward propulsion.

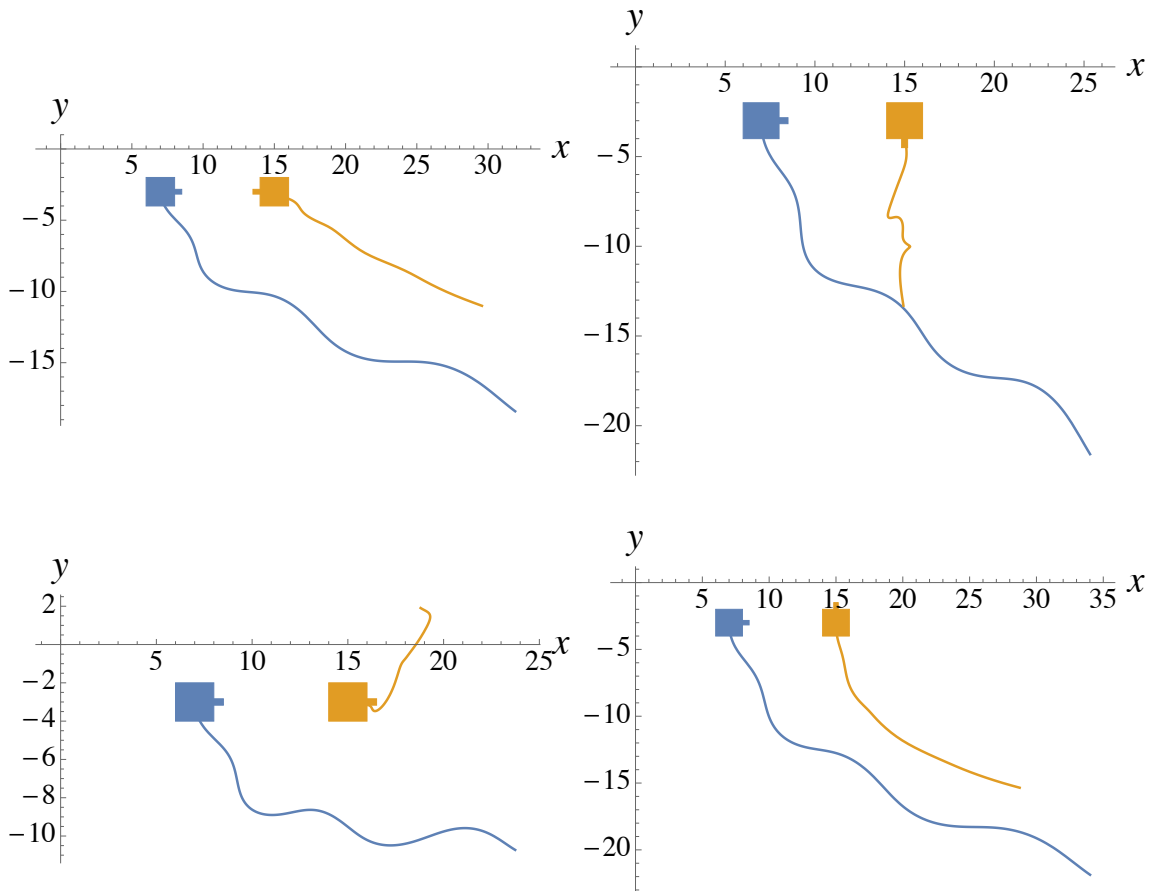

Figure 18: Initial trajectories leading to the entrainment of a spring-driven Chaplygin beanie (orange) by a sinusoidally actuated Chaplygin beanie (blue) on a shared platform that exhibits finite translational inertia. The trajectories shown are measured relative to the platform. The parameters m, a, B, and C are set to unity for both vehicles, as are the mass of the platform and the stiffness of the torsional spring coupling the orange rotor and cart. The blue rotor pivots relative to the blue cart so that $\phi = \sin t$. The two vehicles are shown in their initial configurations in each panel. Since the forward translational speed of each is necessarily nondecreasing, a trajectory that appears to indicate translation in reverse actually reflects reorientation followed by translation. Each panel represents the interval $0 < t < 20$.

What's unapparent is whether or not a relationship exists between the actuated vehicle's eventual direction of translation and that of the passive vehicle. At this point

in the narrative, the system resembles an asymmetric variant of Huygens' clocks: two oscillators share a substrate through which vibrational energy can be transmitted, and as a result the oscillatory dynamics of one drive similar oscillatory dynamics in the other. The reader might anticipate that the passive vehicle will be attracted to a state of translation parallel or antiparallel to the translation of the actuated vehicle, observing that the rear wheel of the passive vehicle will be maximally responsive to lateral forcing and minimally responsive to longitudinal forcing, but this reasoning suggests no bias between parallel and antiparallel states.

In fact, the passive vehicle will eventually follow the actuated vehicle even if doing so requires a complete reversal in the former's heading. The asymptotic difference between the average heading of the one vehicle and the average heading of the other isn't zero — we compare *average* headings because both vehicles describe persistently undulatory paths — but remains small regardless of the initial position and orientation of the one relative to the other. This is illustrated in Figs. 18 and 19. Fig. 18 depicts initial trajectories corresponding to four distinct initial conditions. Some of these trajectories suggest a rapid convergence of the two vehicles' headings, others do not. Fig. 19 depicts the long-term average difference in the vehicles' headings as a function of the initial difference for two different initial relative positions. This long-term average difference is less than $\pi/20$ radians in almost every case, indicating a robust tendency for the actuated vehicle to entrain the passive vehicle in a manner suggestive of the entrainment that can occur when one body propels itself past another in a fluid.

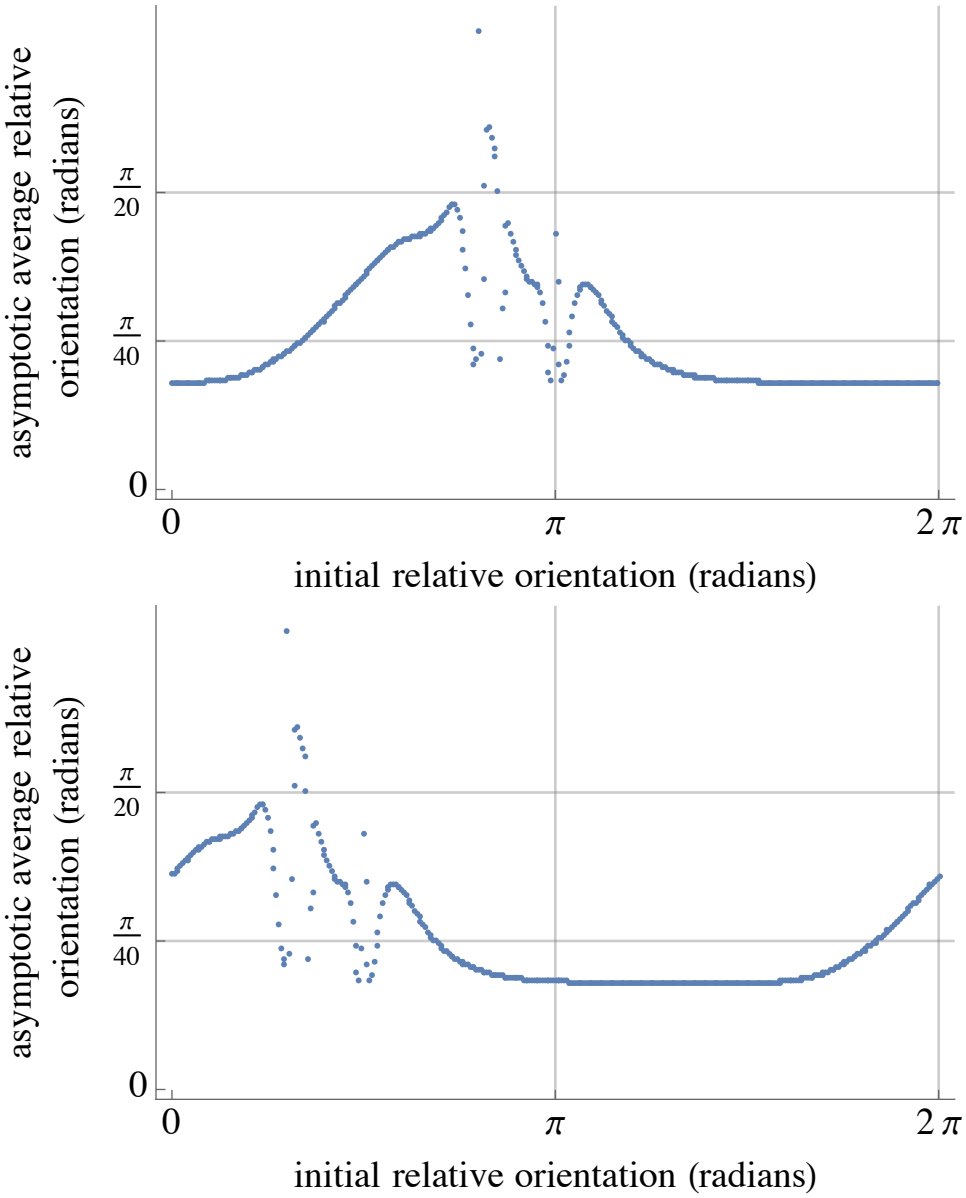

Figure 19: Asymptotic average relative orientation as a function of initial relative orientation for the pair of Chaplygin beanies depicted in Fig. 18. The upper panel corresponds to initial conditions like those in Fig. 18, for which the actuated vehicle initially points away from the passive vehicle, while the lower panel corresponds to initial conditions for which the passive vehicle is initially on the actuated vehicle's right flank. Although the ranges of initial conditions represented by the two panels above are qualitatively distinct, the data they contain are related by an offset of $\pi/2$ radians because the entrainment phenomenon they represent is invariant under translations of either vehicle relative to the other.

CHAPTER 4: SWIMMING AT LOW REYNOLDS NUMBER

4.1 Introduction

The self-propulsion of a solid body deforming in a viscous fluid, if both are initially at rest, can be modeled in the low–Reynolds number limit in terms of a principal connection on a principal fiber bundle. Coordinates on the bundle's base manifold parameterize the body's shape and coordinates on the fiber manifold parameterize the body's position and orientation relative to a stationary frame of reference. Early manifestations of this idea appear in [43, 26]. It follows that the body's displacement and rotation over time can be described by an equation of the form

$$\dot{g} = -g\mathcal{A}(s, \dot{s}), \tag{6}$$

where g is an element of a matrix Lie group G and $\mathcal{A}(s, \dot{s})$ is an element of the corresponding matrix Lie algebra $\mathfrak{g}$ that depends arbitrarily on the body shape s and linearly on the time derivative $\dot{s}$. The matrix $\mathcal{A}(s, \dot{s})$ represents the natural pairing of $\dot{s}$, thought of as a tangent vector on the manifold of body shapes, with a $\mathfrak{g}$-valued one-form $A(s)$ on this manifold. In the context of planar locomotion, G is the special Euclidean group SE(2).

If the body deforms in a time-periodic way, then the net change in position and orientation over one period can be thought of as the geometric phase associated with a closed path in the manifold of body shapes. In the limit as such a path becomes small

— that is, if the cyclic change in the body's shape represents only a small perturbation from a nominal shape — then the associated geometric phase can be approximated by exponentiating the integral of a $\mathfrak{g}$-valued two-form called the local curvature over the area enclosed by the path. Although the geometric phase associated with a large cyclic change in body shape generally isn't well approximated by the integrated local curvature, a visualization of the scalar components of the local curvature on the manifold of body shapes can facilitate a visual approach to motion planning based on the qualitative notion that a path enclosing greater curvature will be a path that produces greater displacement and/or reorientation.

This geometric description of locomotion through shape change isn't restricted to the context of a body in a Stokes flow. The essential physical feature of this problem is that $\dot{g}$ depends linearly on $\dot{s}$ so that the system is driftless, the relationship between shape change and propulsion is invariant under time rescaling, and reversibility precludes the realization of net displacement or reorientation from a cyclic deformation that doesn't enclose area in the manifold of body shapes. Principal connections can be realized as models for the self-propulsion of deformable bodies mediated by conservation laws or by nonholonomic constraints as well; a general introduction to the underlying mathematics appears in [25].

Illustrations of this formalism that appear in the literature rely almost exclusively on analytical models derived from idealized mechanical principles. In this chapter, we realize visualizations of the local curvatures of principal connections arising in low Reynolds–number locomotion using data from physical experiments instead. The systems we consider operate at Reynolds numbers near one; empirical evidence indicates

that they exhibit the driftlessness and reversibility required to justify models in the form of principal connections.

We focus on two planar swimming devices. The first is a variation of the three-link *Purcell swimmer* [40], a canonical system that has been studied analytically and experimentally in the literature. The local curvature of a connection modeling the self-propulsion of this device was obtained analytically in [19] using slender-body theory [14] under the simplifying assumption that the hydrodynamics of each link were decoupled from the hydrodynamics of the others. We reproduce the analytical result of [19], amended slightly to reflect a particular choice of physical proportions for the swimmer's three links, and then juxtapose plots depicting the theoretical local curvature with plots depicting actual translations and rotations of a physical robot propelling itself in a fluid. Overall, our experimental results validate the theoretical model, but some discrepancies are apparent, potentially indicating shortcomings of the assumption of hydrodynamic decoupling among links.

The second system we consider comprises a square array of pitching hydrofoils in a viscous fluid. Again we derive a principal connection using slender-body theory under the assumption that distinct hydrofoils in the array are decoupled hydrodynamically, and again we compare plots depicting the local curvature of this connection to experimental data, observing general but not perfect agreement between theory and experiment. Our study of this second system complements work done in collaboration to document the hydrodynamics within self-propelling hydrofoil arrays at higher Reynolds numbers, at which such arrays may be considered plausible models for biological or robotic fish schools.

The goal of this work isn't simply to validate models like that in [19] for locomotion at low Reynolds number, but also to advance the notion that when the physics underlying a control system justify a model based on a principal connection, a limited sampling of the system's responsiveness to select inputs can be used to estimate the curvature of this connection, from which the system's response to an arbitrary periodic input can then be estimated in the absence of a theoretical model. It was noted above that the existing literature concerning principal connections and locomotion is concerned mostly with theoretical models, but an exception that serves as a precursor to the present work is manifest in [16], wherein laboratory measurements provided the basis for a geometric model for the self-propulsion of a snakelike robot in a granular medium. Here, we adopt a fundamentally different approach to model estimation from that in [16]. Small aperiodic deformations of the robot considered in [16] were used to estimate the connection form A, from which the local curvature was subsequently computed analytically. We use periodic deformations of the robots in this work to estimate the local curvature directly without an estimate of the connection form itself. The sense in which the local curvature is ultimately the object of interest for motion planning is illustrated by the example problem described in section 4.2.

4.2 Curvature and Phase for an Abelian System

For the uninitiated reader, we illustrate the notion of local curvature with an analysis of the simple system depicted in Fig. 20. A circular boat floats in an inviscid fluid. Centered atop the boat is an umbrella. An actuator opens and closes the umbrella;

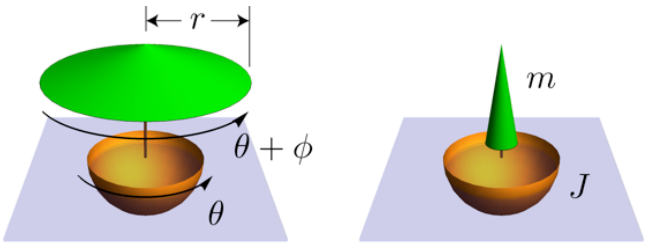

Figure 20: The brown boat can be reoriented, according to (7), by opening, twisting, closing, and untwisting the green umbrella.

another actuator rotates the umbrella relative to the boat. The rotational inertia of the boat is constant but that of the umbrella varies as the umbrella is opened or closed. If the system is initially at rest, then opening and closing the umbrella while rotating it back and forth relative to the boat can induce the boat to exhibit net rotation as a consequence of the conservation of angular momentum about the umbrella's handle.

Suppose, in particular, that θ and ϕ parameterize the rotation of the boat relative to the water and that of the umbrella relative to the boat, respectively, while r parameterizes the extent to which the umbrella is open. If J denotes the boat's rotational inertia and m is a mass associated with the umbrella so that mr^2 corresponds to the umbrella's rotational inertia, then the conservation of initial null momentum corresponds to the equation

$$\dot{\theta} + \frac{mr^2}{J + mr^2}\dot{\phi} = 0. \tag{7}$$

The system's configuration manifold is the Cartesian product of a half-cylinder with coordinates (r, ϕ) and a circle with coordinate θ. The operation of angle addition endows the latter with the structure of a Lie group, so that the configuration manifold

may be regarded as a principal bundle with the half-cylinder as its base manifold and fibers diffeomorphic to the circle. The group operation can be associated with matrix multiplication — so that we have a matrix Lie group, as specified in section 4.1 — by associating each θ with a matrix of the form

$$\begin{bmatrix} 1 & \theta \\ 0 & 1 \end{bmatrix}.$$

With this association, (7) is equivalent to (6) with

$$A(r,\phi) = \begin{bmatrix} 0 & \frac{mr^2}{J+mr^2} \\ 0 & 0 \end{bmatrix} d\phi$$

as the local connection form on the half-cylinder.

Since the circle is one dimensional, only one element in the preceding matrix is nonzero. It's common practice to shift, according to notational convenience, between regarding elements of the Lie algebra in a problem like this as matrices (so that the Lie bracket operation is the matrix commutator) and regarding Lie algebra elements as column vectors; in the present case, the column vector in question is just a scalar one-form. The exterior derivative of this one-form is the Lie algebra–valued two-form

$$dA = \frac{2Jmr}{(J+mr^2)^2}\, dr \wedge d\phi. \tag{8}$$

In general, the local curvature associated with a connection form A is denoted DA and can be computed using the structure equation

$$DA(u,v) = dA(u,v) - [A(u), A(v)], \tag{9}$$

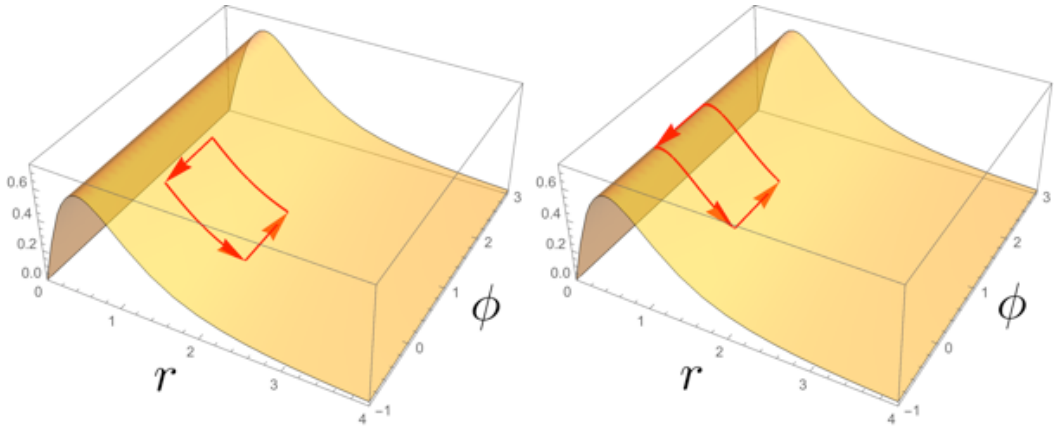

Figure 21: Plots of the scalar coefficient appearing in the local curvature (8) associated with the connection governing the dynamics of the system depicted in Fig. 20, with $J = m = 1$, overlaid with trajectories corresponding to the umbrella motions (10) and (12).

where u and v are arbitrary tangent vectors on the base manifold.[5] In the present case, because the Lie algebra is Abelian, DA and dA are equal.

Suppose, for simplicity's sake, that $J = m = 1$. Fig. 21 depicts two plots of $\frac{2r}{(J+r^2)^2}$ versus r and ϕ. Atop the left-hand plot is overlaid a path that projects downward onto the path C_{left} in the (r, ϕ) plane parameterized by

$$(r,\phi) = \begin{cases} (1+t,0) & \text{if} \quad 0<t<1 \\ (2,t-1) & \text{if} \quad 1<t<2 \\ (4-t,1) & \text{if} \quad 2<t<3 \\ (1,4-t) & \text{if} \quad 3<t<4 \end{cases} . \tag{10}$$

If the umbrella is manipulated according to this parameterization, the boat will exe-

[5]The structure equation (9) varies in the literature, sometimes including a plus sign in place of the minus sign and sometimes including a multiplicative factor of one half, according to whether left bundles or right bundles are being discussed and according to variations in the definition of the wedge product of one-forms and in the sense in which the Lie bracket is defined. We consider left bundles, adopt the wedge product of [45] and [1] rather than that of [28], and consider the bracket to be that denoted by $[\cdot,\cdot]_{\mathfrak{g}}$ in [29] rather than that denoted by $[\cdot,\cdot]_{\wedge}$ in [29].

cute a net rotation equal to

$$\begin{aligned}\theta(4) - \theta(0) &= -\int_{\text{interior of } C_{\text{left}}} \frac{2r}{(1+r^2)^2}\, dr \wedge d\phi \\ &= -\int_0^1 \int_1^2 \frac{2r}{(1+r^2)^2}\, dr\, d\phi = -3/10.\end{aligned} \tag{11}$$

Atop the right-hand plot is overlaid a path that projects downward onto the path C_{right} in the (r, ϕ) plane parameterized by

$$(r,\phi) = \begin{cases} (1/2 + t, 0) & \text{if} \quad 0 < t < 1 \\ (3/2, t-1) & \text{if} \quad 1 < t < 2 \\ (7/2 - t, 1) & \text{if} \quad 2 < t < 3 \\ (1/2, 4-t) & \text{if} \quad 3 < t < 4 \end{cases} \tag{12}$$

If the umbrella is manipulated according to this parameterization, the boat will execute a net rotation equal to

$$\begin{aligned}\theta(4) &= -\int_{\text{interior of } C_{\text{right}}} \frac{2r}{(1+r^2)^2}\, dr \wedge d\phi \\ &= -\int_0^1 \int_{1/2}^{3/2} \frac{2r}{(1+r^2)^2}\, dr\, d\phi = -32/65.\end{aligned} \tag{13}$$

The utility of the local curvature plot appearing twice in Fig. 21 is evident in the comparison of these two motions. Without performing any computation whatsoever, a cyclic change in the umbrella's configuration that will result in greater or lesser net rotation of the boat — even a cyclic change that corresponds to a path arbitrarily more complicated in shape than a rectangle — can be distinguished graphically simply by the amount of curvature it encloses.[6]

[6]Since the value of the local curvature at each point in the base manifold is represented in a figure like Fig. 21 by the height of a surface over a plane, some authors refer to the scalar components of local curvature as "height functions".

It's because the Lie group in this example is Abelian (and the implications of this fact to the Magnus expansion for geometric phase [30]) that (11) and (13) are exactly true. In the remaining sections of this document, we consider systems that exhibit full planar motion parameterized by the Lie group $SE(2)$, which is not Abelian. Our experimental results will show that local curvature plots for such systems approximately accommodate the same interpretation nevertheless.

Since $SE(2)$ is three dimensional, the local curvature in the context of full planar motion has three components. A common notational convention involves premultiplying both sides of (6) by the matrix g^{-1} and then interpreting the resulting terms as column vectors, as described above. When this is done, the column vector ξ corresponding to the Lie algebra element $-g^{-1}\dot{g}$ comprises the components of a moving body's linear and angular velocities relative to a body-fixed frame of reference rather than a spatially fixed frame. The three components of the local curvature arising in the context of planar locomotion correspond, accordingly, to rates of longitudinal and lateral translation and of pivoting.

4.3 Three-Link Purcell Swimmer

The first system we consider both analytically and experimentally is the three-link swimmer depicted in Fig. 22. The outer links each have length $2l$ while the middle link has length $2L$, with $L > l$. The joint angles ϕ and ψ are defined as shown.

Slender-body theory predicts that at low Reynolds number, the longitudinal and lateral forces on each link and the moment about the center of each link are given by

$$F_{i,x} = k\, l_i\, \xi_{i,x}, \quad F_{i,y} = 2k\, l_i\, \xi_{i,y}, \quad M_i = \frac{2}{3} k\, l_i^3\, \xi_{i,\theta}, \tag{14}$$

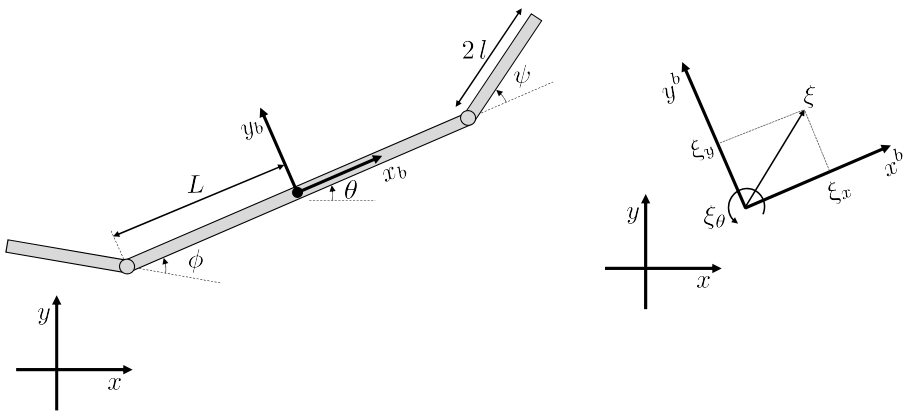

Figure 22: Three-link swimmer. *Left*: Model geometry. *Right*: Body velocity.

respectively, where $\xi_i = [\xi_{i,x}, \xi_{i,y}, \xi_{i,\theta}]^T$ is the body velocity of the ith link, $l_1 = l_3 = l$, $l_2 = L$, and k is a constant.

The body velocities are given by

$$\xi_1 = \begin{bmatrix} \cos(\phi)\xi_x - \sin(\phi)\xi_y + L\sin(\phi)\xi_\theta \\ \sin(\phi)\xi_x + \cos(\phi)\xi_y - (l + L\cos(\phi))\xi_\theta + l\dot{\phi} \\ \xi_\theta - \dot{\phi} \end{bmatrix},$$

$$\xi_2 = \xi,$$

$$\xi_3 = \begin{bmatrix} \cos(\psi)\xi_x + \sin(\psi)\xi_y + L\sin(\psi)\xi_\theta \\ -\sin(\psi)\xi_x + \cos(\psi)\xi_y + (l + L\cos(\psi))\xi_\theta + l\dot{\psi} \\ \xi_\theta + \dot{\psi} \end{bmatrix}.$$

Summing forces and moments about the body-fixed frame, we obtain the generalized

force vector

$$F = \begin{bmatrix} F_x \\ F_y \\ M \end{bmatrix} = \begin{bmatrix} \cos(\phi) & \sin(\phi) & 0 \\ -\sin(\phi) & \cos(\phi) & 0 \\ L\sin(\phi) & -L\cos(\phi) - l & 1 \end{bmatrix} \begin{bmatrix} F_{1,x} \\ F_{1,y} \\ M_1 \end{bmatrix} + \begin{bmatrix} F_{2,x} \\ F_{2,y} \\ M_2 \end{bmatrix} + \begin{bmatrix} \cos(\psi) & -\sin(\psi) & 0 \\ \sin(\psi) & \cos(\psi) & 0 \\ L\sin(\psi) & L\cos(\psi) + l & 1 \end{bmatrix} \begin{bmatrix} F_{3,x} \\ F_{3,y} \\ M_3 \end{bmatrix}.$$

We can rewrite this in the form

$$F = \omega(s) \begin{bmatrix} \xi \\ \dot{s} \end{bmatrix}, \tag{15}$$

where $s = [\phi, \psi]^T$ represents the shape variables and $\omega(s)$ is a 3×5 matrix. Furthermore, we can write

$$\omega(s) = \begin{bmatrix} \omega_1 & \omega_2 \end{bmatrix},$$

where ω_1 and ω_2 are 3×3 and 3×2 matrices respectively.

In an isolated system forces and moments must sum to zero; we obtain a connection from the requirement that

$$F = \begin{bmatrix} 0 \\ 0 \\ 0 \end{bmatrix} = \begin{bmatrix} \omega_1 & \omega_2 \end{bmatrix} \begin{bmatrix} \xi \\ \dot{s} \end{bmatrix},$$

which can be rearranged into the form

$$\xi = -\omega_1^{-1}\omega_2\dot{s}, \tag{16}$$

which matches (6) as outlined in sections 4.1 and 4.2.

The three components of the local curvature associated with the connection represented by $\omega_1^{-1}\omega_2$ in (16), computed using (9), are depicted as functions of ϕ and ψ in the left-hand column of Fig. 23. The right-hand column of Fig. 23 depicts corresponding experimental data obtained in a manner to be described in section 4.5.

4.4 Four-Paddle Swimmer

We now consider a new system, depicted in Fig. 24, consisting of four paddles with hinges placed at the corners of a square of side $\sqrt{2}L$. The length of each paddle is $2l$. The paddles are numbered 1 through 4 starting with the top right one and continuing in a counterclockwise direction. The orientations of the paddles are determined by the shape variables ϕ and ψ as indicated in the figure. Paddles 1 and 3 (in red) move in unison as parameterized by ϕ; paddles 2 and 4 (in blue) move in a mirrored way as parameterized by ψ. We attach a frame of reference at the center of the square, aligning the longitudinal direction with the diagonal between paddles 1 and 3.

The configuration manifold for this system is the same as that for the three-link swimmer but the local connection is different. To find the local connection we repeat the procedure outlined in section 4.3. The forces and moments about the centers of the paddles are given by (14). A difference with the previous system is that $l_i = l$ for

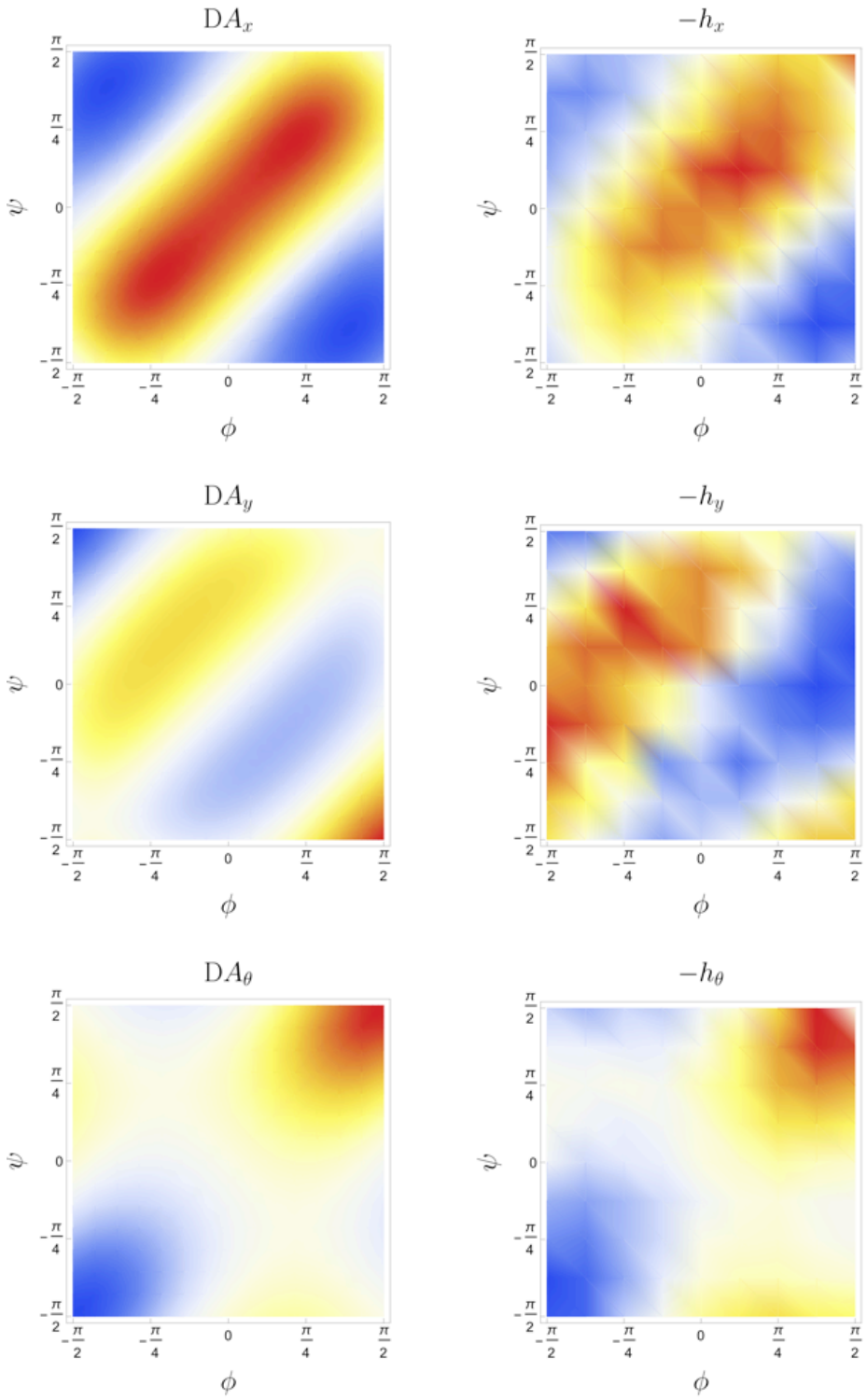

Figure 23: Three-link swimmer plots. *Left*: Theoretical curvature plots corresponding to the three components of $\mathfrak{se}(2)$. *Right*: Components of geometric phase (or *holonomy*) h obtained after performing closed-loop trajectories in the shape manifold, multiplied by -1 for easy comparison with the curvature plots.

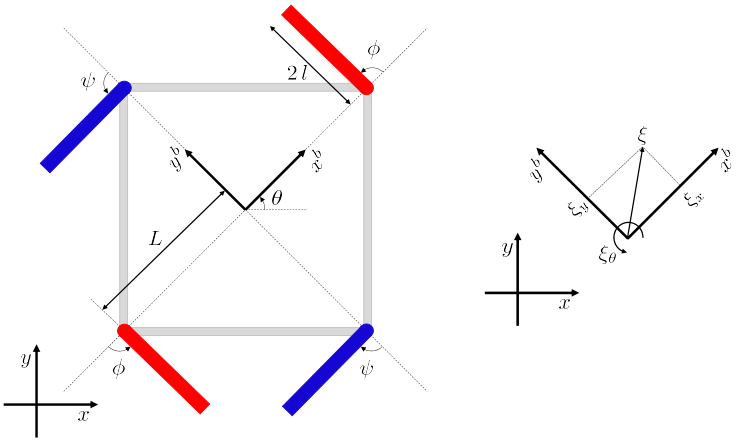

Figure 24: Four-paddle swimmer. *Left*: Model geometry. *Right*: Body velocity.

$i = 1, \ldots, 4$. The body velocities[7] for the paddles are

$$\xi_1 = \begin{bmatrix} \cos(\phi)\xi_x + \sin(\phi)\xi_y + L\sin(\phi)\xi_\theta \\ -\sin(\phi)\xi_x + \cos(\phi)\xi_y + (l + L\cos(\phi))\xi_\theta + l\dot{\phi} \\ \xi_\theta + \dot{\phi} \end{bmatrix},$$

$$\xi_2 = \begin{bmatrix} -\sin(\psi)\xi_x + \cos(\psi)\xi_y + L\sin(\psi)\xi_\theta \\ -\cos(\psi)\xi_x - \sin(\psi)\xi_y + (l + L\cos(\psi))\xi_\theta + l\dot{\psi} \\ \xi_\theta + \dot{\psi} \end{bmatrix},$$

$$\xi_3 = \begin{bmatrix} -\cos(\phi)\xi_x - \sin(\phi)\xi_y + L\sin(\phi)\xi_\theta \\ \sin(\phi)\xi_x - \cos(\phi)\xi_y + (l + L\cos(\phi))\xi_\theta + l\dot{\phi} \\ \xi_\theta + \dot{\phi} \end{bmatrix},$$

$$\xi_4 = \begin{bmatrix} -\sin(\psi)\xi_x - \cos(\psi)\xi_y - L\sin(\psi)\xi_\theta \\ \cos(\psi)\xi_x - \sin(\psi)\xi_y + (l + L\cos(\psi))\xi_\theta - l\dot{\psi} \\ \xi_\theta - \dot{\psi} \end{bmatrix}.$$

[7] A body frame is considered to be attached at the center of each paddle, with its longitudinal direction aligned with the paddle and the positive direction going away from the hinge.

We can write the generalized force vector relative to the body-fixed frame as

$$\begin{bmatrix} F_x \\ F_y \\ M \end{bmatrix} = \begin{bmatrix} \cos(\phi) & -\sin(\phi) & 0 \\ \sin(\phi) & \cos(\phi) & 0 \\ L\sin(\phi) & L\cos(\phi)+l & 1 \end{bmatrix} \begin{bmatrix} F_{1,x} \\ F_{1,y} \\ M_1 \end{bmatrix} + \begin{bmatrix} -\sin(\psi) & -\cos(\psi) & 0 \\ \cos(\psi) & -\sin(\psi) & 0 \\ L\sin(\psi) & L\cos(\psi)+l & 1 \end{bmatrix} \begin{bmatrix} F_{2,x} \\ F_{2,y} \\ M_2 \end{bmatrix} + \begin{bmatrix} -\cos(\phi) & \sin(\phi) & 0 \\ -\sin(\phi) & -\cos(\phi) & 0 \\ L\sin(\phi) & L\cos(\phi)+l & 1 \end{bmatrix} \begin{bmatrix} F_{3,x} \\ F_{3,y} \\ M_3 \end{bmatrix} + \begin{bmatrix} -\sin(\psi) & \cos(\psi) & 0 \\ -\cos(\psi) & -\sin(\psi) & 0 \\ -L\sin(\psi) & L\cos(\psi)+l & 1 \end{bmatrix} \begin{bmatrix} F_{4,x} \\ F_{4,y} \\ M_4 \end{bmatrix}.$$

Writing this equation in the form (15) and equating the generalized force to zero, we again obtain an equation that can be manipulated to look like (6), and thus obtain a connection form. The three components of the local curvature, computed using (9), are depicted as functions of ϕ and ψ in the left-hand column of Fig. 25. The right-hand column of Fig. 25 depicts corresponding experimental data.

4.5 Experimental Estimation of Curvature

Fig. 26 depicts physical versions of the three-link and four-paddle swimmers. Both systems are based on a reconfigurable platform comprising a square frame with four Pololu micro gear motors with encoders. On each motor a paddle or link may be

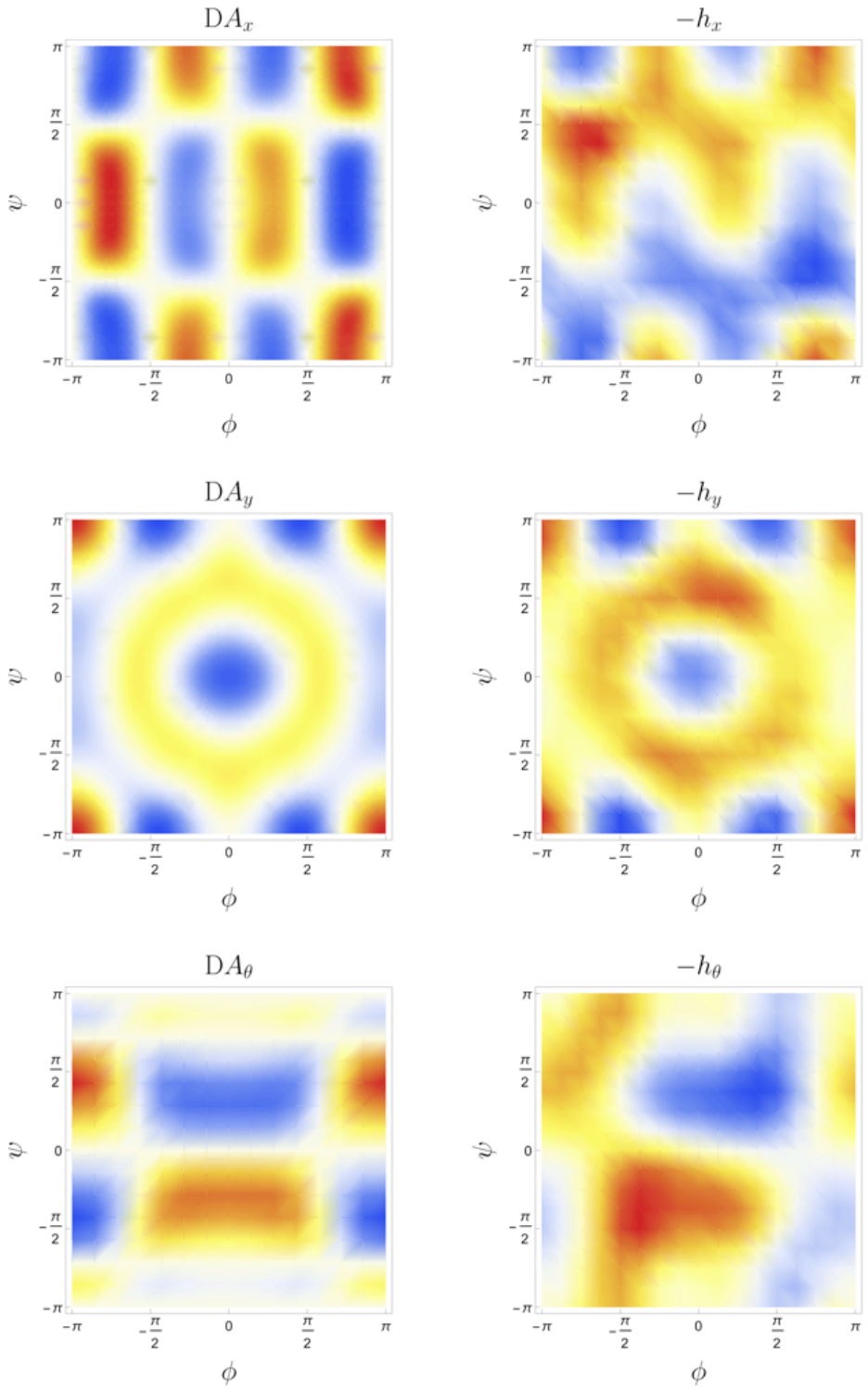

Figure 25: Four-paddle swimmer plots. *Left*: Theoretical curvature plots corresponding to the three components of $\mathfrak{se}(2)$. *Right*: Components of geometric phase (or *holonomy*) h obtained after performing closed-loop trajectories in the shape manifold, multiplied by -1 for easy comparison with the curvature plots.

attached to the shaft, depending on the desired configuration. For the three-link swimmer, an extra passive link can be added along the diagonal of the frame to act as the middle link. The square frame is suspended from a horizontal beam with supports on the ends. Each of the supports consists of a styrofoam tower, shown in pink. Mounted on the beam is an Arduino Mega that controls the movement of the motors. The controller is equipped with an XBee for serial wireless communication with a PC. The electronics are powered by an on-board 6V 2200mAh NiMH battery pack.

Each swimmer is deployed in a bath of light corn syrup. To ensure that the only interaction between the fluid and the swimmer is through the paddles, the experiment rests atop an air table that's pressurized to levitate the two styrofoam supports. Fig. 27 shows the setup with a swimmer in the fluid. We track the motion of each swimmer using markers on the supporting beam, seen in yellow in Fig. 27. Images are taken from a Raspberry Pi camera mounted above the test apparatus. The coordinates of the markers are obtained using a projective transformation with the aid of the known position of four fixed reference markers on the table.

In order to estimate the local curvature of the connection underlying the dynamics of each swimmer experimentally, we select a family of square trajectories, akin to the square trajectories considered in the example of section 4.2, that tile the manifold of swimmer shapes. Each trajectory is centered around a shape corresponding to a different point (ϕ, ψ); we evaluate the geometric phase associated with each trajectory and associate it with the corresponding point. In the limit as the area enclosed by such a trajectory becomes small, the associated phase is equal to the image under the

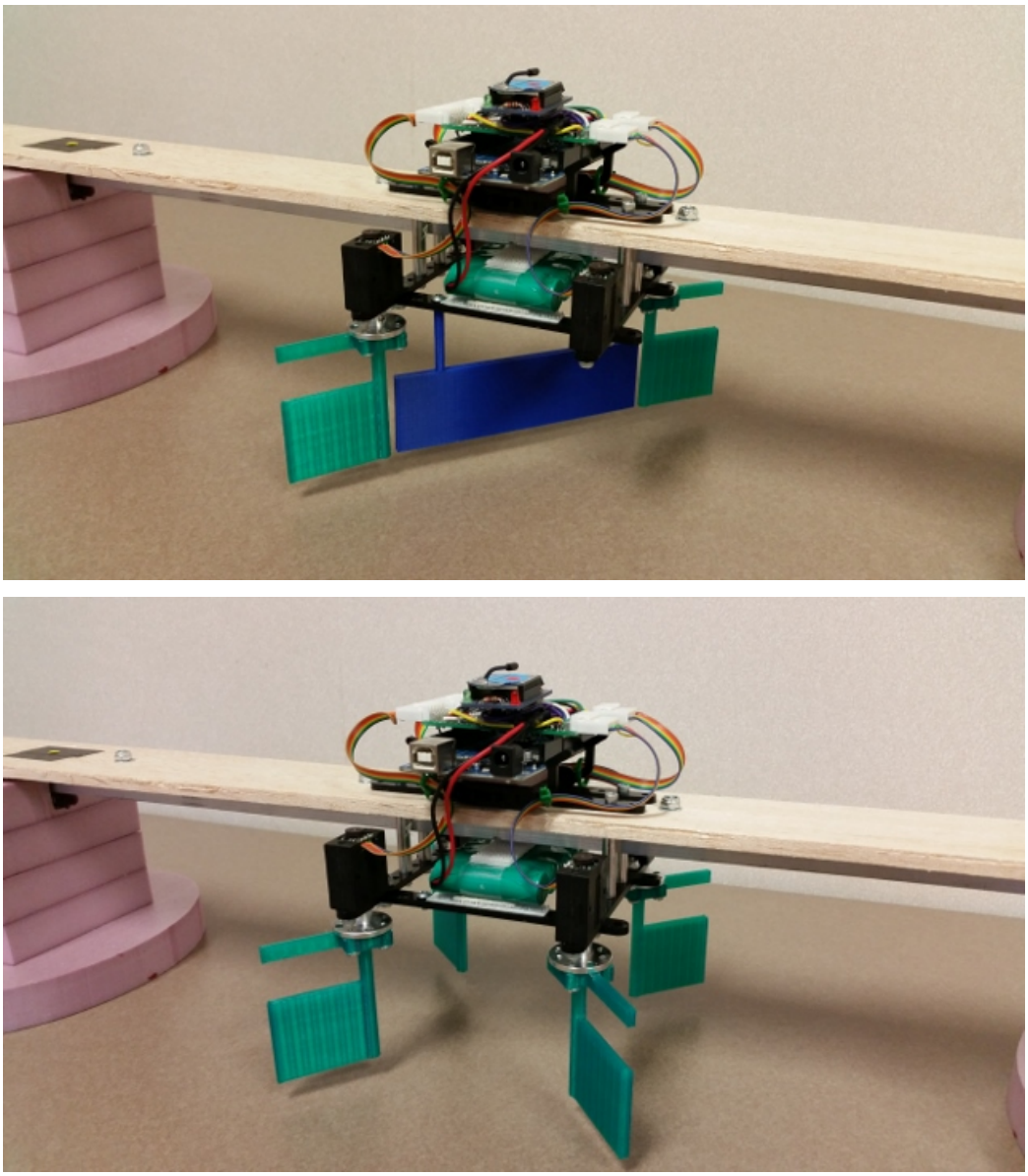

Figure 26: Experimental three-link swimmer and four-paddle swimmer.

exponential map of the integral of the local curvature form — multiplied by minus one — over the area enclosed by the trajectory. If the phase associated with a trajectory that encloses a larger area corresponds to fiberwise left translation by a group element h in the system's configuration bundle, then the matrix logarithm of h will provide an approximation to the product of the local curvature at the center of the trajectory and the area enclosed by the trajectory.

The experiments generating the data depicted in the right-hand columns of Figs. 23 and 25 correspond to a discretization of the space of pairs (ϕ, ψ) into a grid with steps of $\pi/8$ radians. Associated with each grid point is the geometric phase associated with a counterclockwise square trajectory $\pi/2$ radians by $\pi/2$ radians in size. For the three-link swimmer, the search grid ranges from $-\pi/2$ to $\pi/2$ radians because of physical considerations. For the four-paddle swimmer, the search grid ranges from $-\pi$ to π radians.

As Figs. 23 and 25 show, systematic sampling of the geometric phase associated with relatively large square trajectories in this way is sufficient to reproduce many qualitative features of the local curvatures for both swimmers. In the absence of analytical models, the right-hand columns of these figures could faithfully serve as surrogates for the left-hand columns for the purpose of selecting gaits that enclose desired combinations of positive and negative curvature.

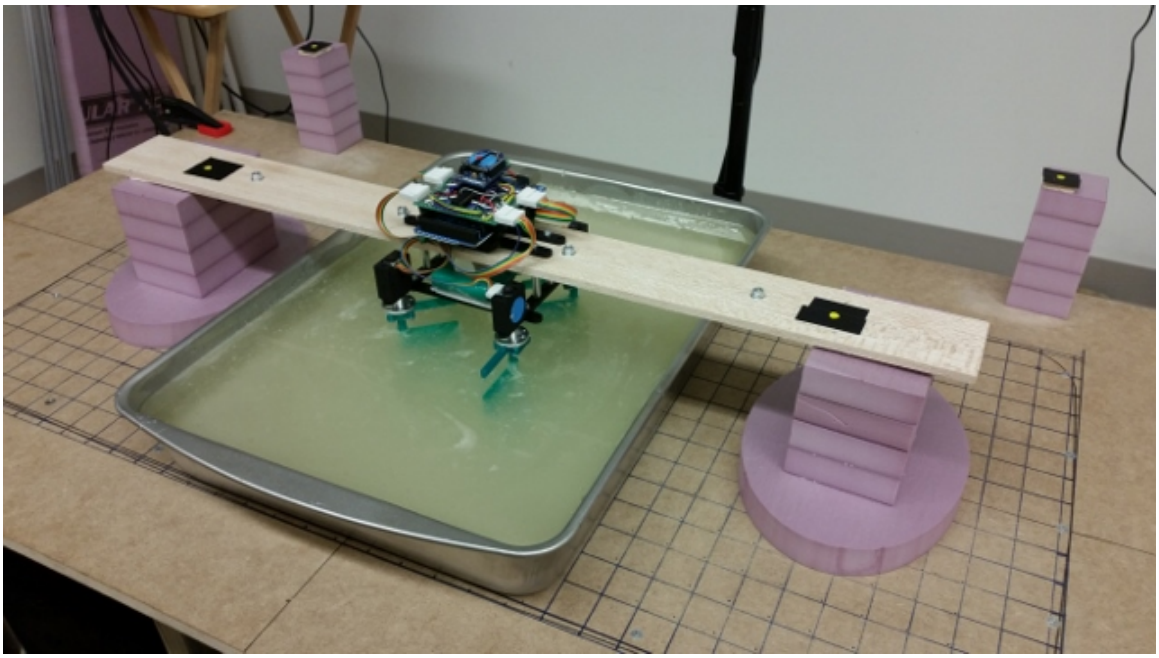

Figure 27: Four-paddle swimmer in fluid atop air table.

CHAPTER 5: THREE-LINK SWIMMER IN IDEAL FLUID

5.1 Introduction

In the 1660s, the pioneering chemist Robert Boyle compiled a list of desiderata for the future of natural philosophy. Alongside a number of priorities familiar in the modern era, including *The Art of Flying*, *The Cure of Diseases... by Transplantation*, and *The practicable... way of finding Longitudes*, this list — reproduced in full in [22] — asserts the importance of

The Emulating of Fish without Engines by Custome & Education only

as a topic for future study.[8] Boyle's ambition in this area is unclear, but the present chapter concerns the emulation of fish with a deficit of engines — suitably interpreted — and concludes with the promise of future work exploiting "custome and education only" in this context.

Biomimetic designs for aquatic robots have received substantial attention in recent decades because of the agility and efficiency of swimming marine animals. Although the elastic compliance of marine animal skin has been acknowledged as a contributor to efficiency through drag reduction — a survey of research concerning skin properties and drag reduction appears in [18] — the role of body elasticity as a surrogate for actuation within jointed swimmers isn't fully understood. The simplest possible

[8] Boyle's spelling and capitalization have been reproduced from the original manuscript.

biomimetic swimmer is arguably the three-link swimmer with two coplanar actuated joints introduced in [40] and used in Chapter 4. In this chapter, we examine a variation of this system in which only one of the swimmer's joints is actuated directly while the other is fitted with a damped torsional spring in place of an actuator.

In section 5.2 we describe a mathematical model for a singly actuated Purcell-style swimmer in an ideal fluid and demonstrate that sinusoidal forcing of the modeled system's actuated joint is sufficient to excite oscillations in the elastic joint and enable locomotion. Varying the forcing frequency influences the nature of this locomotion in a manner that can be understood by visualizing the system's dynamics in joint-angle space against the backdrop of the three scalar functions representing the local curvature. In section 5.3 we describe physical experiments with a Purcell-style swimmer in a laboratory water tank, comparing singly actuated locomotion to fully actuated locomotion. These experiments confirm the influence that forcing frequency can have on swimming speed and direction for the singly actuated robot and demonstrate that replacing an actuator with a spring can result in improved energy efficiency.

5.2 Modeling and Simulation

Purcell's swimmer has become a canonical system in the literature concerning locomotion through shape change at low Reynolds number. In this setting, the system admits an elegant mathematical model whereby the displacement and reorientation associated with a periodic change in shape can be associated with a geometric phase related to the corresponding path in the space of joint angles. A summary of this perspective is provided by [2] alongside experimental data validating such a model

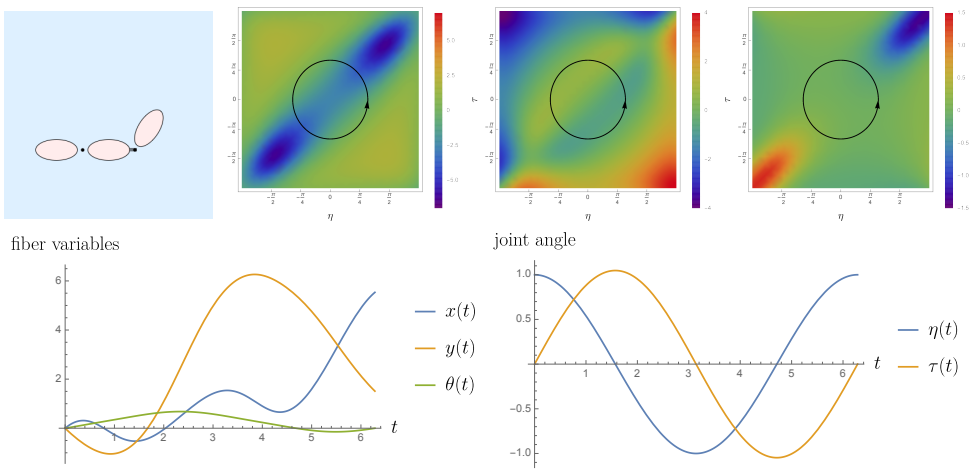

Figure 28: Swimming gait, corresponding to a circular path centered about the origin in joint-angle space, resulting in net displacement and reorientation from rest for the Purcell-style swimmer in an ideal fluid. The three components of the local curvature are computed as functions of the joint angles under the assumption that each elliptical body link has only added mass (in the sense of [35]). The functions $x(t)$, $y(t)$, and $\theta(t)$ are determined numerically from the conservation of linear and angular momentum. All physical parameters are assigned nominal values of order one.

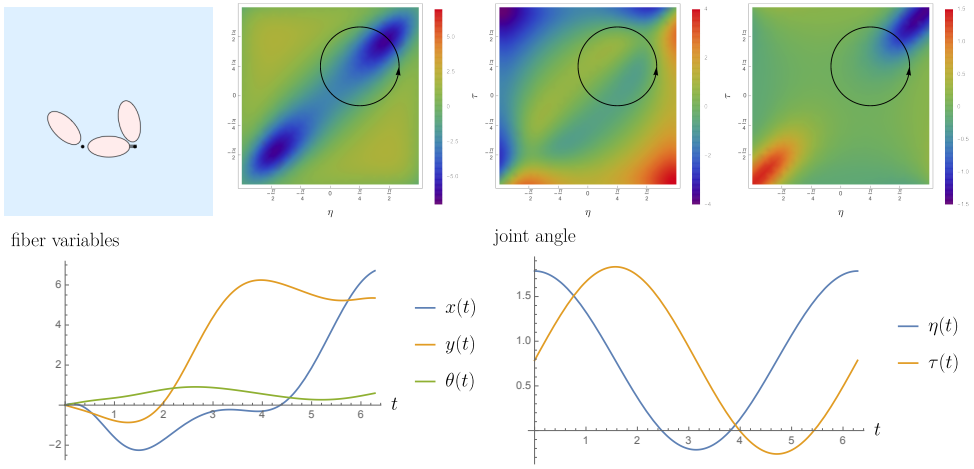

Figure 29: Swimming gait, corresponding to a circular path centered about $(\pi/4, \pi/4)$ in joint-angle space, resulting in net displacement and reorientation from rest for the Purcell-style swimmer in an ideal fluid. The three components of the local curvature are computed as functions of the joint angles under the assumption that each elliptical body link has only added mass (in the sense of [35]). The functions $x(t)$, $y(t)$, and $\theta(t)$ are determined numerically from the conservation of linear and angular momentum. All physical parameters are assigned nominal values of order one.

for Reynolds numbers close to unity.

The self-propulsion of a deforming body from rest in an inviscid fluid admits an analogous geometric interpretation. The analogy between the two hydrodynamic regimes is detailed in [27]. The displacement and reorientation of the body in response to a periodic shape change may be interpreted as a geometric phase relative to a *mechanical connection*, in the sense of [32], reflecting the conservation of the net linear and angular momentum of the body and fluid together. The fact that the body's effective translational mass varies with its shape enables propulsion in spite of — indeed, because of — momentum conservation.

Associated with the mechanical connection is a vector-valued function of the shape of the body called the *local curvature*. In the context of planar swimming, the local curvature has three scalar components, individually associated with translation in two directions (relative to a body-fixed reference frame) and with rotation. In the case of a Purcell-style swimmer, the local curvature is a function on the two-dimensional torus of joint angles. A mathematical discussion of the relevant geometric mechanics is beyond the scope of the present chapter, but the essential significance of local curvature is straightforward to illustrate.

Figs. 28 and 29 are organized into two rows. Top rows start with a cartoon image of a Purcell-style swimmer comprising three elliptical bodies with joints in between. To the right is a trio of plots depicting, through variations in color, the scalar values of the three components of the mechanical connection's local curvature as functions of the swimmer's two joint angles. Superposed atop each curvature plot is a closed loop representing a cyclic variation in the swimmer's shape, the initial configuration of the

swimmer — as shown in the carton — corresponding to the location of the arrowhead along the loop. The bottom rows show the plots depicting the associated variations in the swimmer's joint angles, position and orientation as individual functions of time.

In each case, the net longitudinal and lateral displacement of the swimmer and its net reorientation at the conclusion of a single cyclic shape change reflect the extent to which negative curvature in the left, center, and right colored plots, respectively, are enclosed bye the looped path. Note in Fig. 28, for instance, that the net curvature enclosed in the left colored plot is more distinctly negative than that enclosed in the center or right plots. The looped path represents a swimming motion resulting in longitudinal translation to a greater degree than it results in lateral translation or rotation. In Fig. 29, the looped path has been shifted to enclose even more negative curvature in the left colored plot, but as a result encloses more negative curvature in the right colored plot as well. The longitudinal translation of the swimmer at the conclusion of the stroke is increased but so too is its reorientation. Mathematically, the enclosure of curvature is associated with locomotion through the application of Stokes' theorem to a truncated version of the series expansion developed in [30], in a manner that's exact in certain situations (as detailed in [25]) but only approximate here.

The paths depicted in joint-angle space in Figs. 28 and 29 are prescribed but those depicted in Fig. 30 are limit cycles that result when one joint angle is varied sinusoidally while the other is allowed to respond dynamically under the influence of a critically damped linear torsional spring with unit stiffness. Each row of the figure represents a different simulation. In each case, one of the swimmer's joints — the

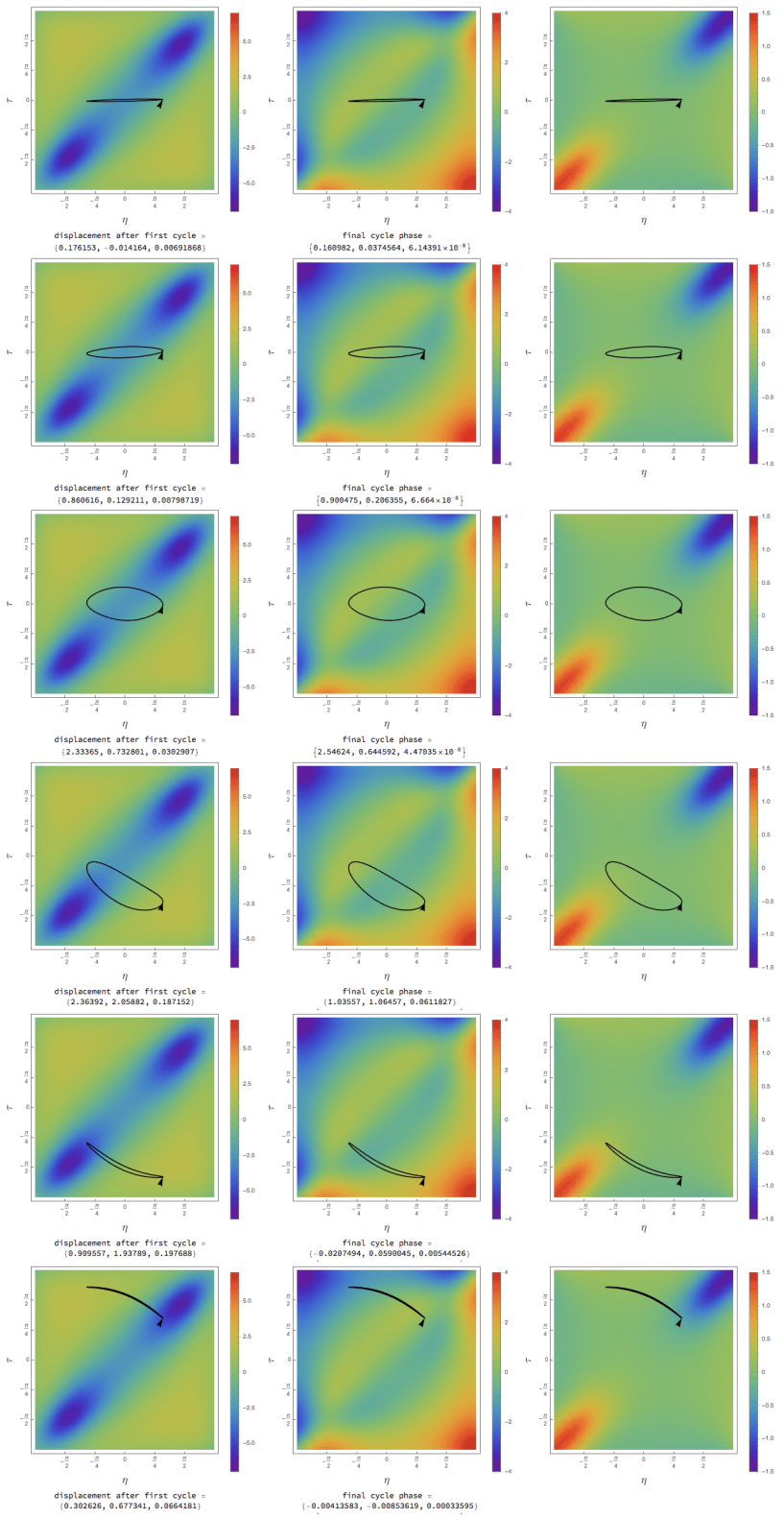

Figure 30: Limit cycles in joint-angle space resulting from sinusoidal oscillations of the swimmer's head joint. Frequency of oscillation decreases in equal steps from top to bottom. Note the bifurcation and reversal in swimming direction toward the bottom.

right-hand joint in the sense of the cartoons of Figs. 28 and 29, parameterized by the variable η ("head") — oscillates sinusoidally with unit amplitude at a different frequency. The other joint, parameterized by τ ("tail"), begins in a centered state with its spring relaxed, but after a small number of periods begins to oscillate with the same frequency. Only the steady-state path in joint-angle space is shown. The curvature enclosed by this steady-state path differs from row to row; the corresponding locomotion differs accordingly.

The frequency at which the swimmer's head oscillates affects not only its average swimming speed but also its swimming direction and rotation rate. Varying only this frequency as a control input, the swimmer can be induced to navigate throughout the plane.

At the extremes of low and high frequency, the limit cycles depicted in Fig. 30 collapse to enclose minimal area. One way to interpret this is to note that changes in frequency are equivalent to changes in spring stiffness with frequency fixed. At high frequency, as shown in the top row of the figure, the spring is effectively slack. At low frequency, as shown in the bottom row, the spring is effectively rigid. In each case, it follows that the swimmer can access only a one-parameter family of shapes and no area can be enclosed in joint-angle space. Maximal translation occurs when the driving frequency is matched to the stiffness of the spring to open the loop in joint-angle space as widely as possible.

5.3 Physical Experiments

The remainder of the chapter describes experiments with a robotic version of the swimmer depicted in Fig. 28. We first consider the case in which one of the robot's joints is driven sinusoidally while the other responds elastically, confirming that variations in swimming speed and direction can be realized through variations in the driving frequency. Damping isn't added to the robot's spring-loaded joint explicitly; friction within the springs we use combines with viscous drag on the body's links to provide approximately critical damping. We then replicate a selection of swimming gaits accessible to the singly actuated robot using a modified robot with actuators at both joints. The way in which the robot's shape varies over time determines its locomotion in a manner that's independent of the number of actuators responsible for the shape change, but we observe that the singly actuated robot is able to propel itself with lower energetic cost because of its internal elastic dynamics.

5.3.1 One Servo and One Spring-Loaded Joint

Fig. 31 depicts a three-link swimmer comprising styrofoam rafts connected with Actobotics aluminum channels. The system is reconfigurable in that servomotors or springs can be fitted to the joints. The yellow markers shown in the figure are used to track the robot's position and orientation using a ceiling-mounted Raspberry Pi camera. The robot swims in a 4ft $\times$ 8ft rectangular tank, floating atop six inches of water. Onboard electronics include a Particle Photon micro-controller, an XBee radio, custom circuitry to measure electrical power consumption, and an SD card writer for data logging.

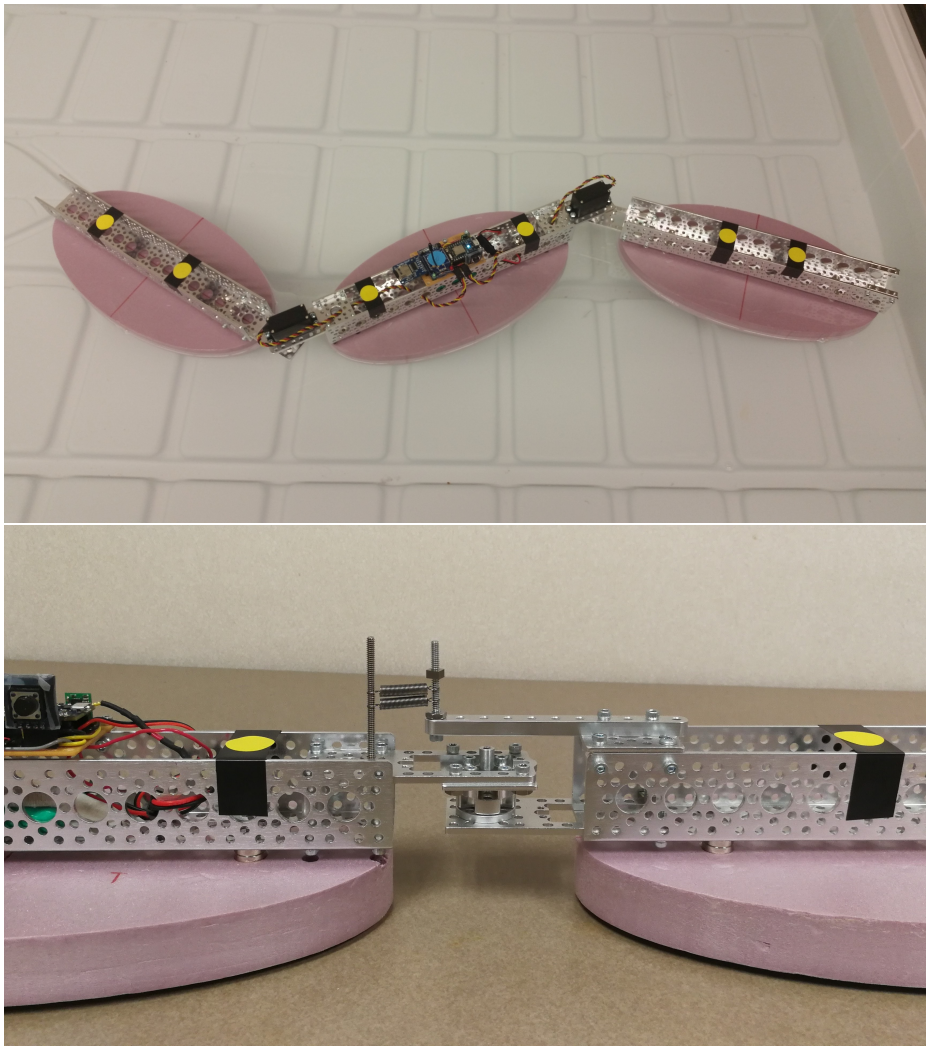

Figure 31: *Top*: A Purcell-style three-link swimmer floating in water. *Bottom*: A spring-loaded unactuated joint.

The experiments that were performed involved the system configured with one servo and one spring-loaded joint. The servo was actuated sinusoidally such that $\eta(t) = A_1 \sin(2\pi f t)$. The frequency f was varied between 0.2 Hz and 1.5 Hz. The spring-loaded joint responded similarly to a spring-mass-damper system. The amplitude and phase responses varied with frequency. Given the response of the passive joint, the system swam forward in some cases and backward in others, according to whether the underactuated joint lagged or led the actuated joint. Fig. 32 summarizes the results obtained after performing experiments with $A_1 = 60$ degrees and three different configurations for the passive joint. The compliance of the joint was changed by adding springs in parallel. From the figure it can be seen that increasing the stiffness of the passive joint increased the maximum swimming speed. It can also be seen that each change in stiffness shifted the frequency corresponding to the maximum speed as it changed the resonant frequency of the system. If we look at both the speed and phase plots, we can see that when the phase plots cross the -180 degrees mark — for all three cases — the swimming speeds turn negative, meaning the swimmer is now swimming backwards. This verifies the basic idea that with different frequencies we can obtain different speeds and directions of swimming.

Another set of experiments was performed using two springs with $A_1 = 30$ degrees, doing the same sweep of frequency. A smaller amplitude of oscillation was chosen to allow a better range of motion in the pool where the experiments were performed. For these experiments we characterized the response of the passive joint for each frequency. The joint-angle trajectory $\tau(t)$ was fitted to a sinusoid of the form $A_2 \sin(2\pi f t + \phi) + D$ for every frequency f. This provided parameters with which to actuate both joint

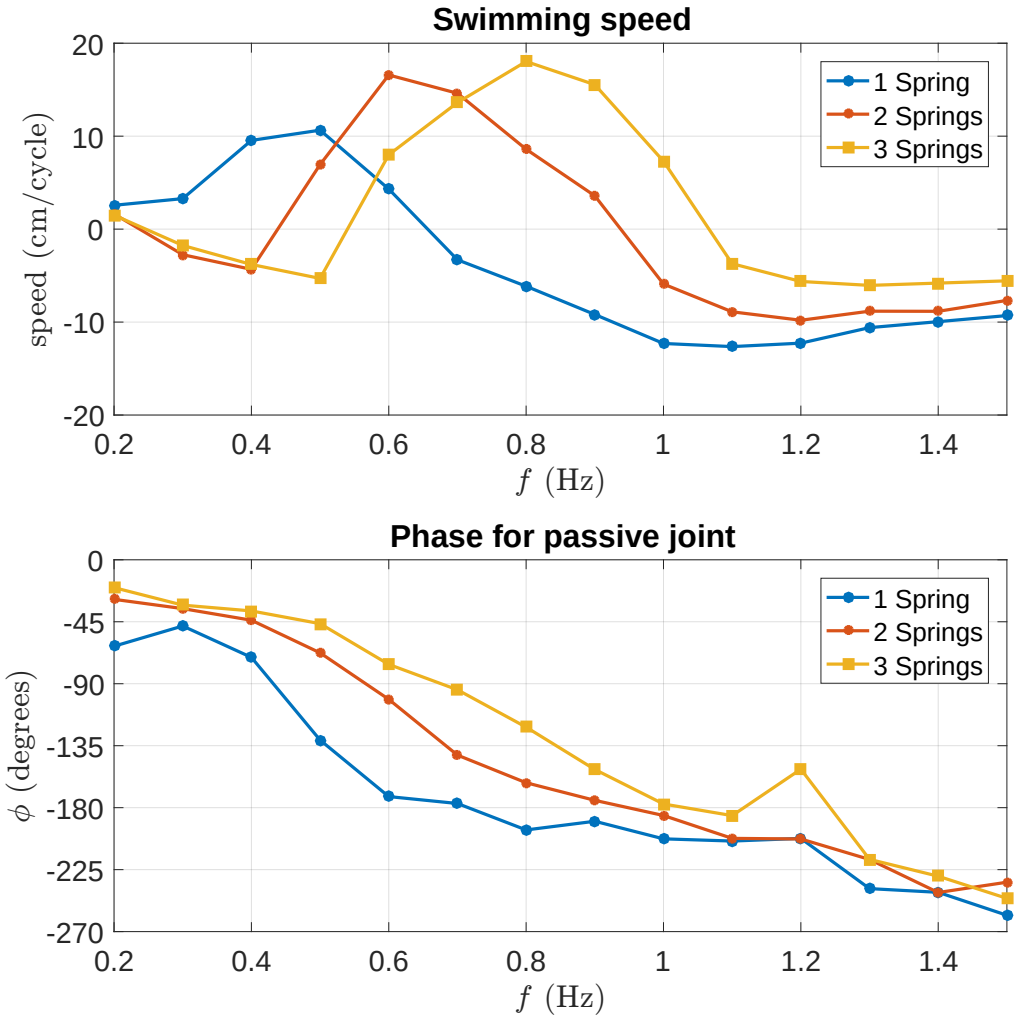

Figure 32: Frequency response with amplitude $A_1 = 60$ degrees for three different spring configurations on the passive joint. *Top:* Swimming speeds. *Bottom:* Phase for the passive joint relative to the actuated joint.

angles in the two-servo swimmer. Table 1 summarizes the swimming speeds obtained with the frequency sweep as well as the parameters characterizing the passive link response for each frequency. There are two speeds reported in the table, speed_1 and speed_2. The former is the maximum of the average speeds calculated at the end of every actuation period considering as starting point the origin of the experiment, while the latter is the maximum of the average speeds for every period of actuation. The two frequencies resulting in the fastest speeds have been highlighted.

Table 1: Data extracted from experiments with two springs and $A_1 = 30$ degrees. Frequency is given in Hz and speed in cm/cycle. The amplitudes A_1 and A_2 as well as the offset D and phase ϕ are all in degrees.

f	speed_1	speed_2	A_1	A_2	D	ϕ
0.2	1.43	1.43	29.43	9.25	-1.80	-16.88
0.3	1.50	1.50	29.36	14.59	-2.68	-20.27
0.4	3.13	3.13	30.68	29.11	-2.28	-37.09
0.5	6.75	6.89	30.02	54.36	-2.46	-84.28
0.6	5.39	5.42	29.65	55.95	-2.76	-147.31
0.7	2.60	2.60	28.66	41.60	-3.20	-170.76
0.8	1.46	1.86	28.78	33.01	-3.14	-178.26
0.9	0.70	0.89	28.59	29.61	-3.54	-192.59
1.0	0.29	0.36	28.88	26.57	-3.51	-198.76
1.1	-0.57	-0.88	28.55	25.09	-4.05	-202.04
1.2	-0.76	-1.21	28.85	23.48	-3.88	-208.06
1.3	-1.14	-1.25	29.19	23.16	-4.12	-195.38
1.4	-1.75	-1.77	29.32	22.90	-3.83	-206.23
1.5	-2.31	-2.32	29.25	21.76	-3.86	-207.93

5.3.2 Two Servos

The swimmer was next equipped with servos at both joints and we prescribed the same joint trajectories as those represented in the 0.5 Hz and 0.6 Hz rows of Table 1. Each run consisted of ten periods of actuation. Now we can compare the results of

the fully actuated experiments and the underactuated ones.

Fig. 33 shows the joint angles driven at 0.5 Hz for both experiments. It can be seen that in general the trajectories agree very well, though there is some difference at the beginning of the experiment because the spring-loaded joint had some transient response.

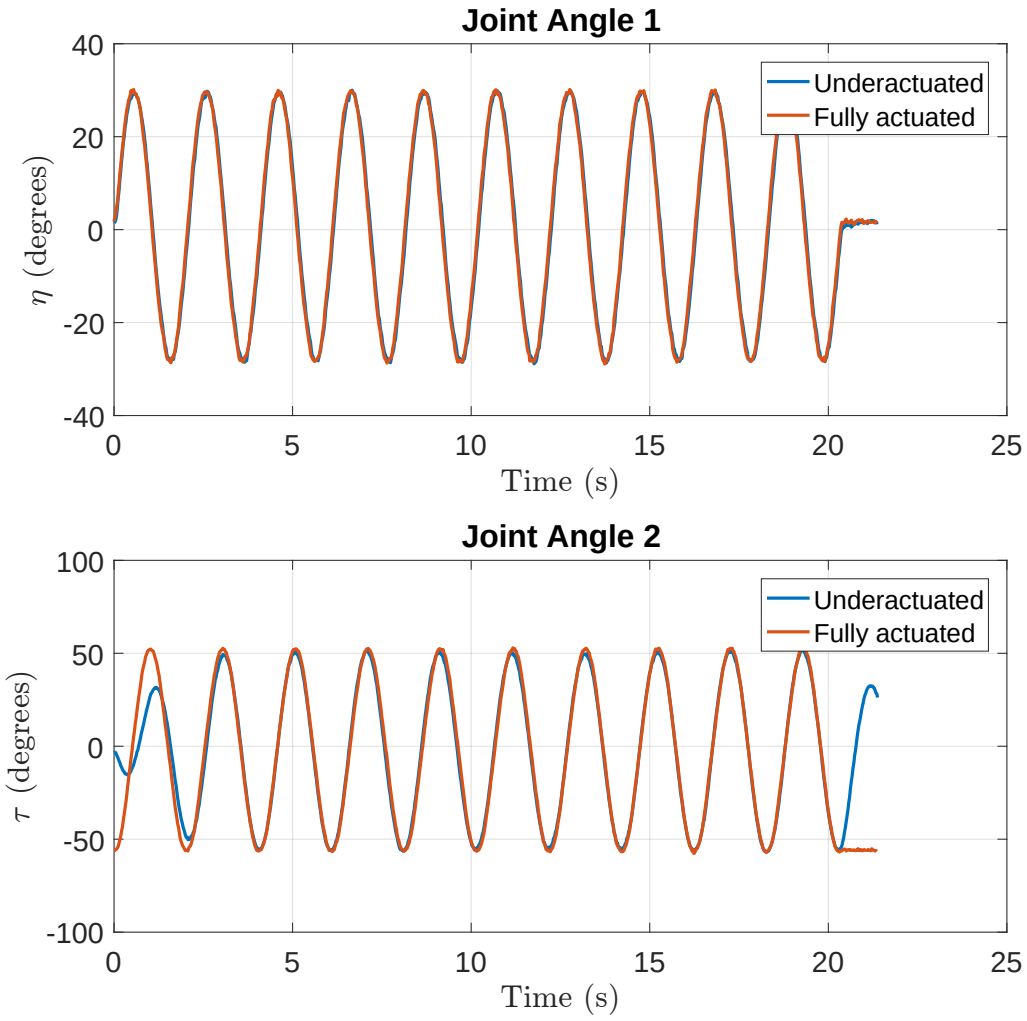

Figure 33: Joint angles at 0.5 Hz for both underactuated and fully actuated configurations.

Fig. 34 shows the trajectories for the center of the middle link for both experiments,

the dots indicate the actuation cycles. Fig. 35 shows the same trajectories, but the initial positions have been translated to the origin with an offset in the y-direction of $+1$ and -1 cm for the two cases. The trajectories have been rotated such that the initial orientation of the middle link is 0 degrees. Fig. 36 shows the orientation of the swimmer throughout the experiment.

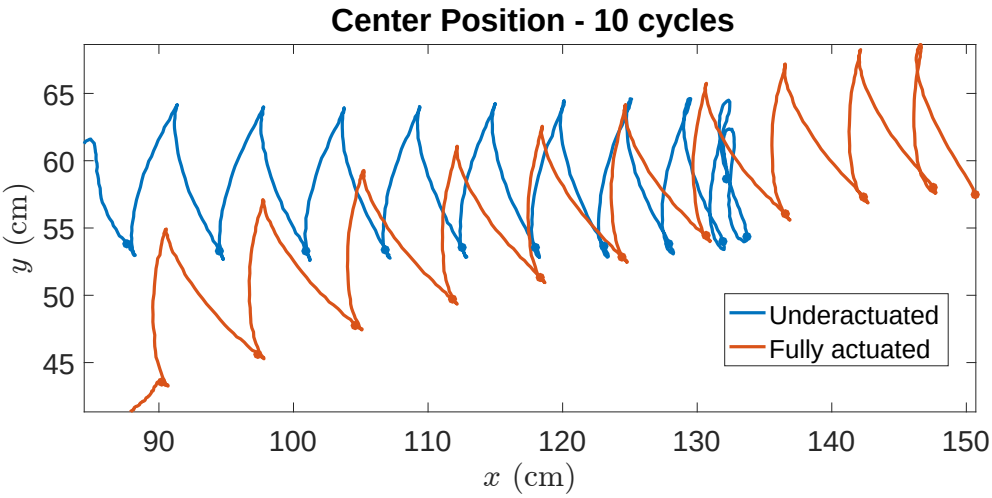

Figure 34: Full trajectories for the underactuated and fully actuated swimmers driven at 0.5 Hz. Both experiments are moving towards the left, in the direction of the "head" of the swimmer. The trajectories show the full motion of the centroid of the middle link, the position after each cycle of actuation marked with a dot.

In the top panel of Fig. 37 is plotted the distance traveled in each experiment starting from period three. The bottom panel compares the distance traveled by the underactuated swimmer to that traveled by the fully actuated swimmer. It can be seen that in period ten, the distance traveled by the underactuated system is within 10% of that traveled by the fully actuated system.

Figs. 38–42 show the same plots corresponding to the systems driven at 0.6 Hz. It can be seen again that the performance of the underactuated system is comparable to

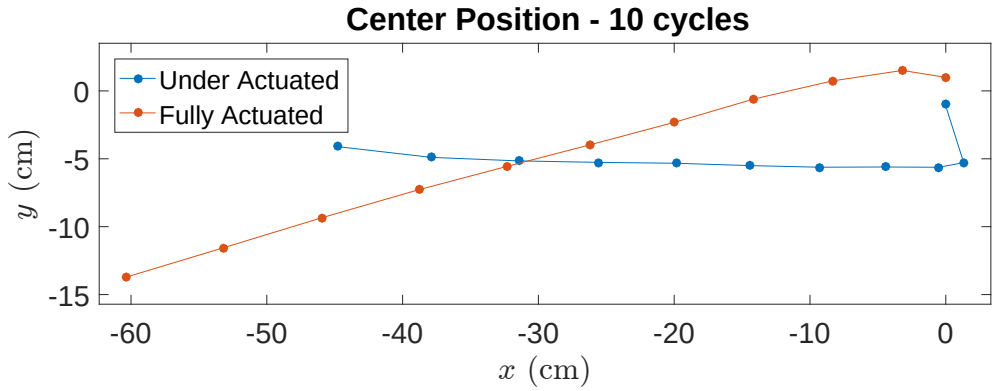

Figure 35: Trajectories sampled once per cycle for experiments driven at 0.5 Hz.

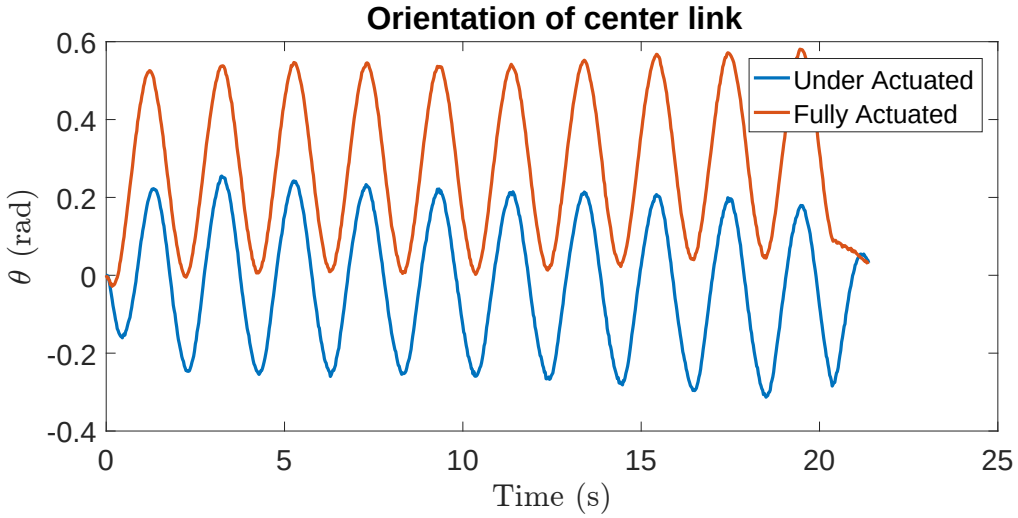

Figure 36: Orientation of middle link for experiments driven at 0.5 Hz.

that of the fully actuated system. There is a bit more of a difference in the distance traveled per cycle, Fig. 42, because the fully actuated system slowed down between periods six and nine, possibly due to interactions with reflected waves in the pool. The underactuated system maintained a nearly constant speed after cycle two, however, as can be seen by the distance between the blue dots in Fig. 40.

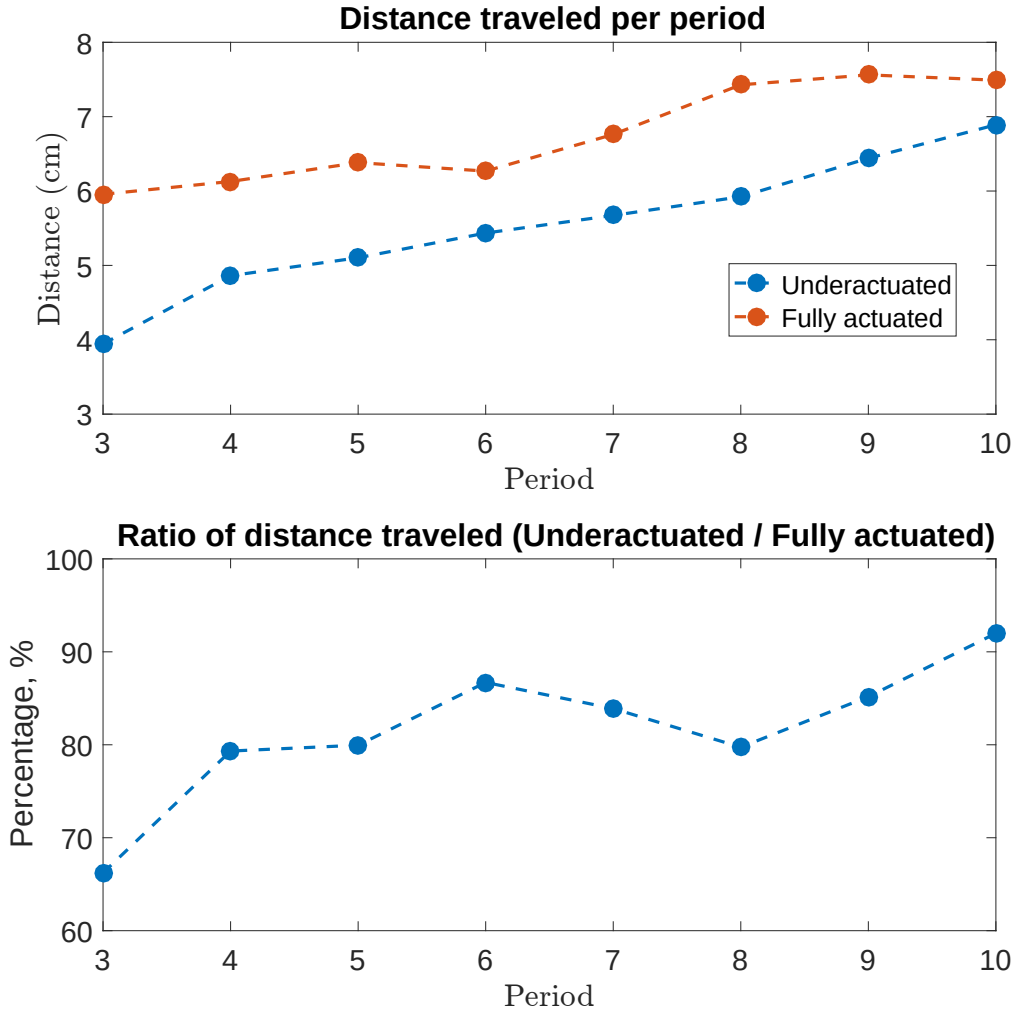

Figure 37: Comparison of distance traveled per period for experiments at 0.5 Hz.

5.3.3 Power Consumption

Power consumption data was collected as the swimmers — underactuated and fully actuated — performed their gaits. Fig. 43 shows the joint angles as they were prescribed by the micro-controller for the underactuated and fully actuated swimmers when driven at 0.5 Hz along with the current measured during these experiments. The current was used to calculate the power consumption by the actuators. It can be seen

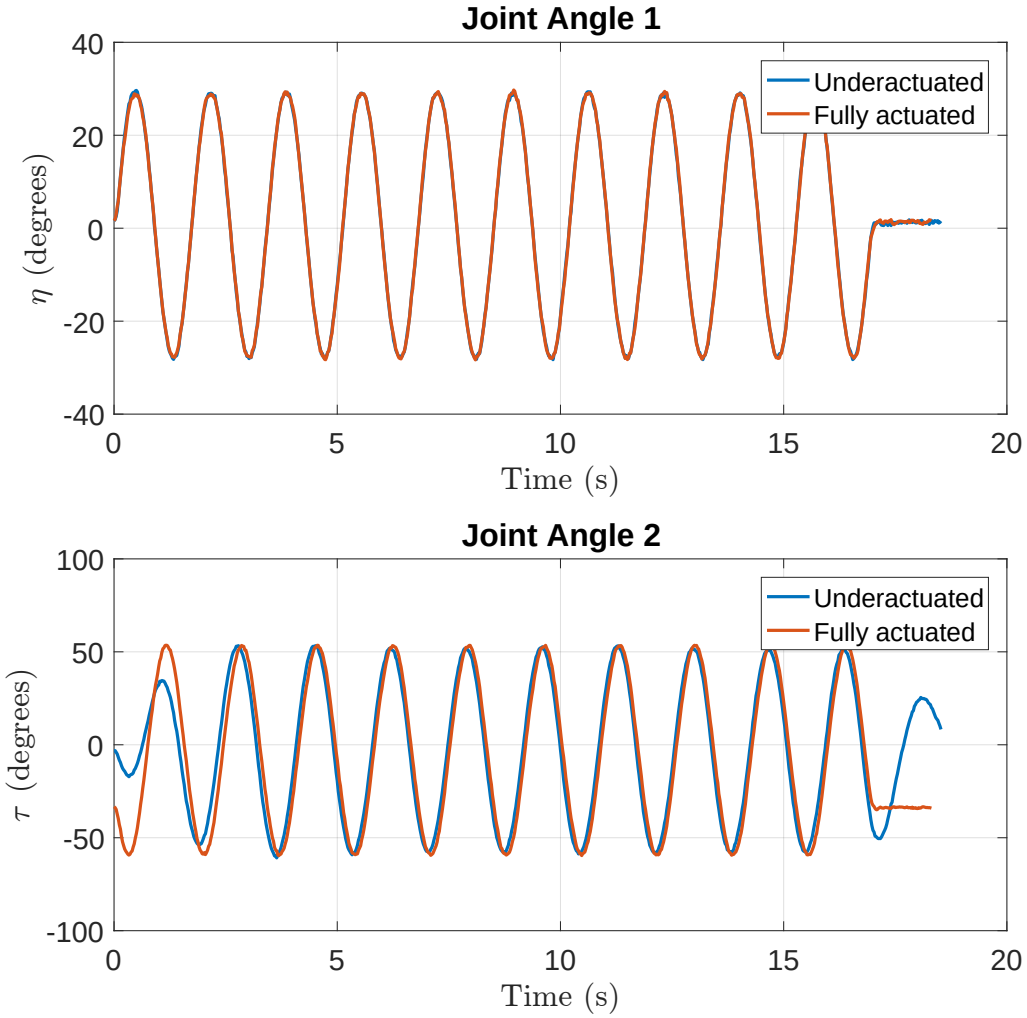

Figure 38: Joint angles at 0.6 Hz for both underactuated and fully actuated configurations.

that the current in the fully actuated system has a greater magnitude. The average current is 57.76 mA for the underactuated swimmer and 145.94 mA for the fully actuated swimmer.

Fig. 44 shows, in the top panel, the average power consumed with both configurations driven at 0.5 Hz. Instantaneous power was first obtained by multiplying instantaneous voltage and current supplied to the servo(s). The average power was

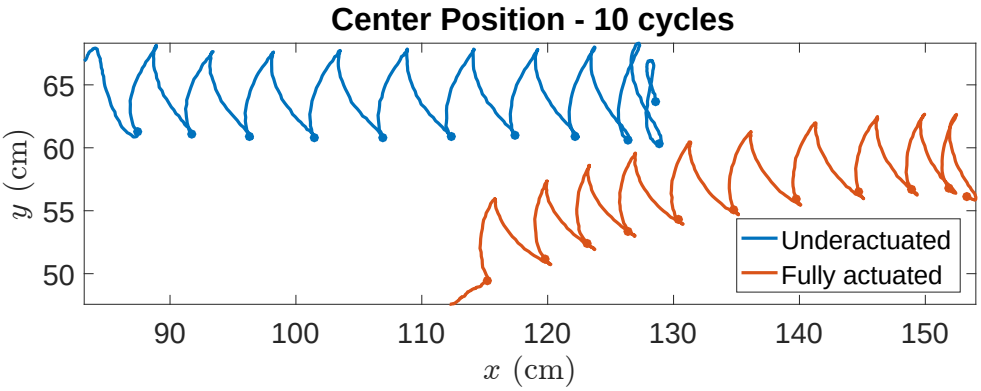

Figure 39: Full trajectories for the underactuated and fully actuated swimmers driven at 0.6 Hz. Both experiments are moving towards the left, in the direction of the "head" of the swimmer. The trajectories show the full motion of the centroid of the middle link, the position after each cycle of actuation marked with a dot.

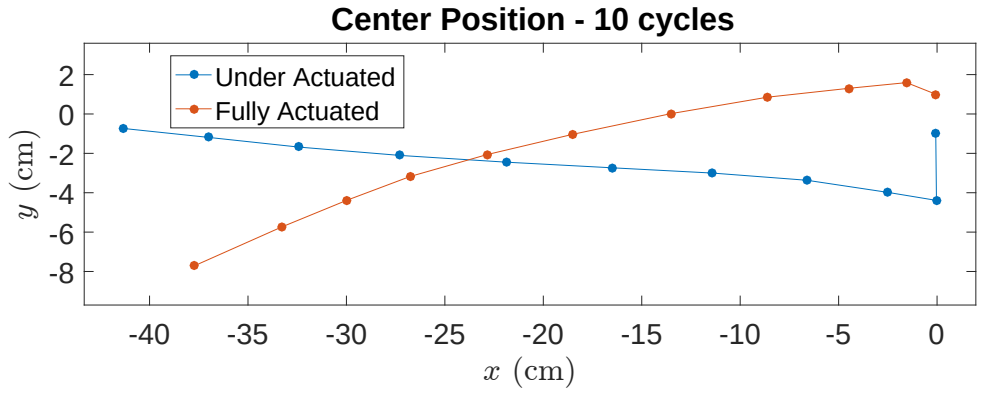

Figure 40: Trajectories sampled once per cycle for experiments driven at 0.6 Hz.

then obtained by averaging the instantaneous power over one period. The average power for each period is indicated by the dots in the top panel of Fig. 44. The continuous lines plotted are the moving average obtained with a window size equal

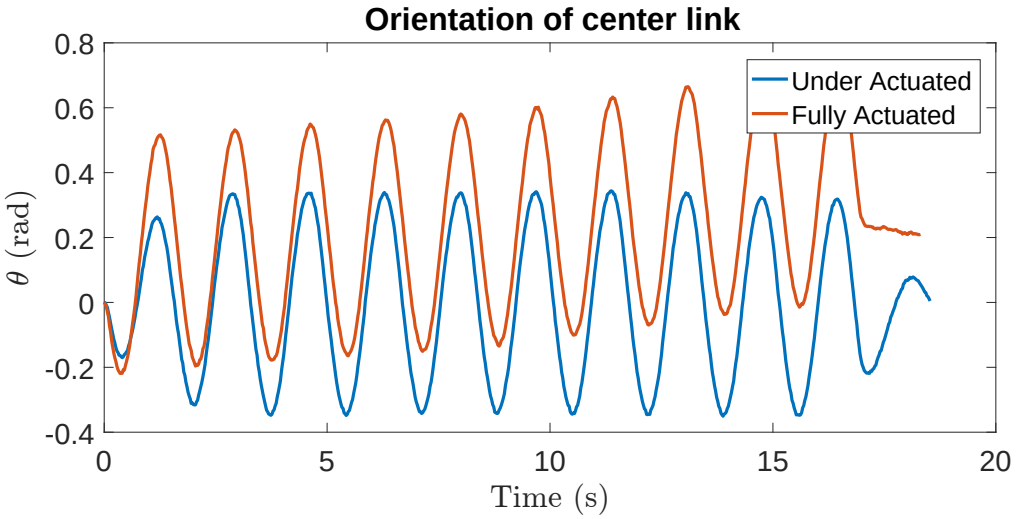

Figure 41: Orientation of middle link for experiments driven at 0.6 Hz.

to the period of the signals prescribed. The bottom panel shows the power ratio

$$\mathrm{P_{ratio}} = \frac{\mathrm{P_{UA}}}{\mathrm{P_{FA}}},$$

where UA and FA stand for underactuated and fully actuated, respectively. In the 0.5 Hz case, the mean power ratio for all cycles is 0.393. The power ratio for the last cycle is 0.4. For the 0.6 Hz driving frequency we get the average power and power ratio as shown in Fig. 45. The average power ratio for 0.6 Hz is 0.339 and the power ratio for the last cycle was 0.34.

All this means that the power being used to drive the actuators was less than half in the case of the single actuator. One may argue that the power consumption advantage seen here reflects the fact that servos require a relatively large amount of current to move even when they are under no external load. This relatively large current is needed because servos are geared, which adds friction and inertia. In an attempt to see if there really is an efficiency increase in replacing a servo with a

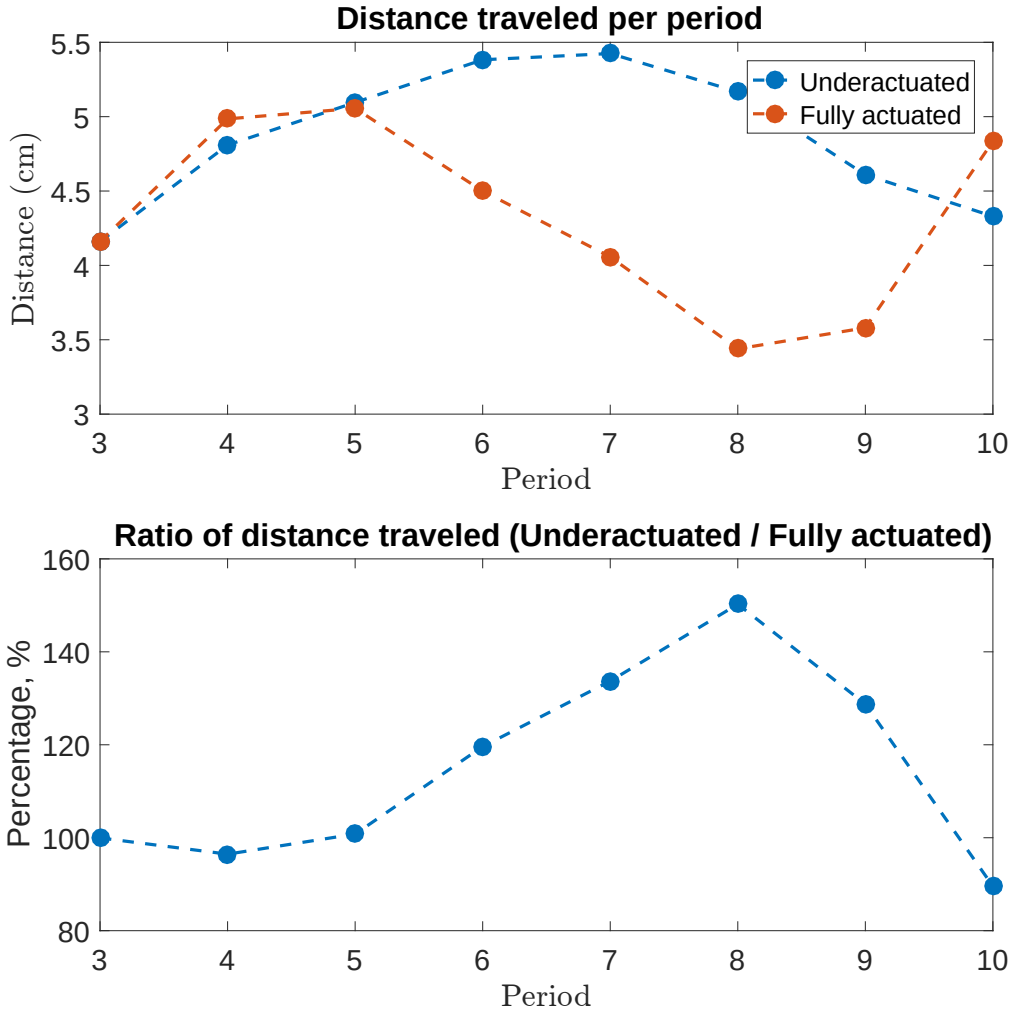

Figure 42: Comparison of distance traveled per period for experiments at 0.6 Hz.

spring, we therefore ran the servos with no load — removed from the system — and measured the power consumption. Such a measurement can be used as a baseline for how much power is being used as overhead by each servo and its gears/inertia. These measurements were done while prescribing the same motions that were used during experiments where the servos were attached to the swimmer in the water. Once the baselines were removed, the power ratios obtained were 0.674 for 0.5 Hz and 0.408

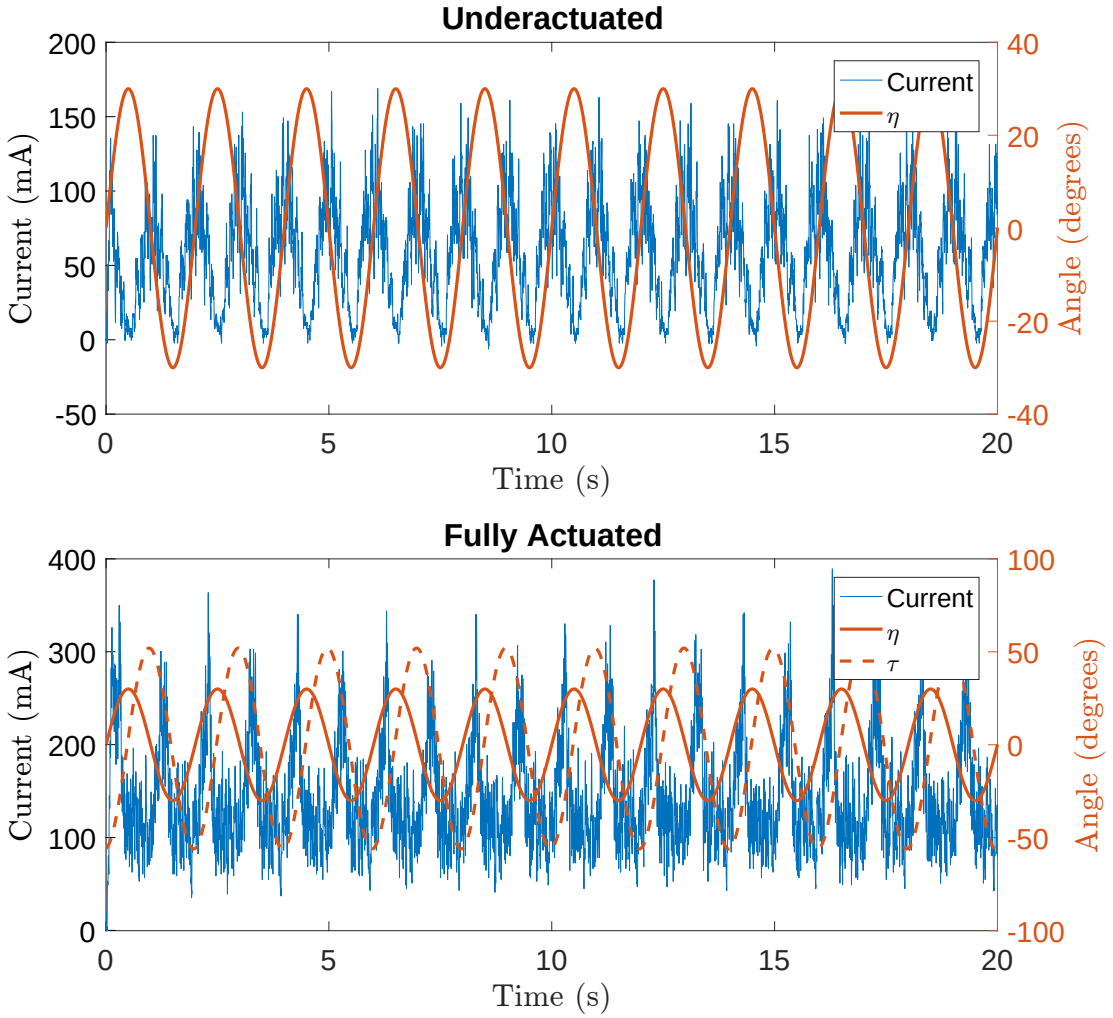

Figure 43: Joint angles as prescribed by the micro-controller and the current measured.

for 0.6 Hz. This means there is indeed an energetic advantage in replacing the second servo with a spring-loaded joint.

5.4 Future Work

The present work sets the stage in an obvious way for computational and experimental studies of swimming devices with larger numbers of internal degrees of freedom endowed with elastic compliance in place of direct actuation. Basic questions in this

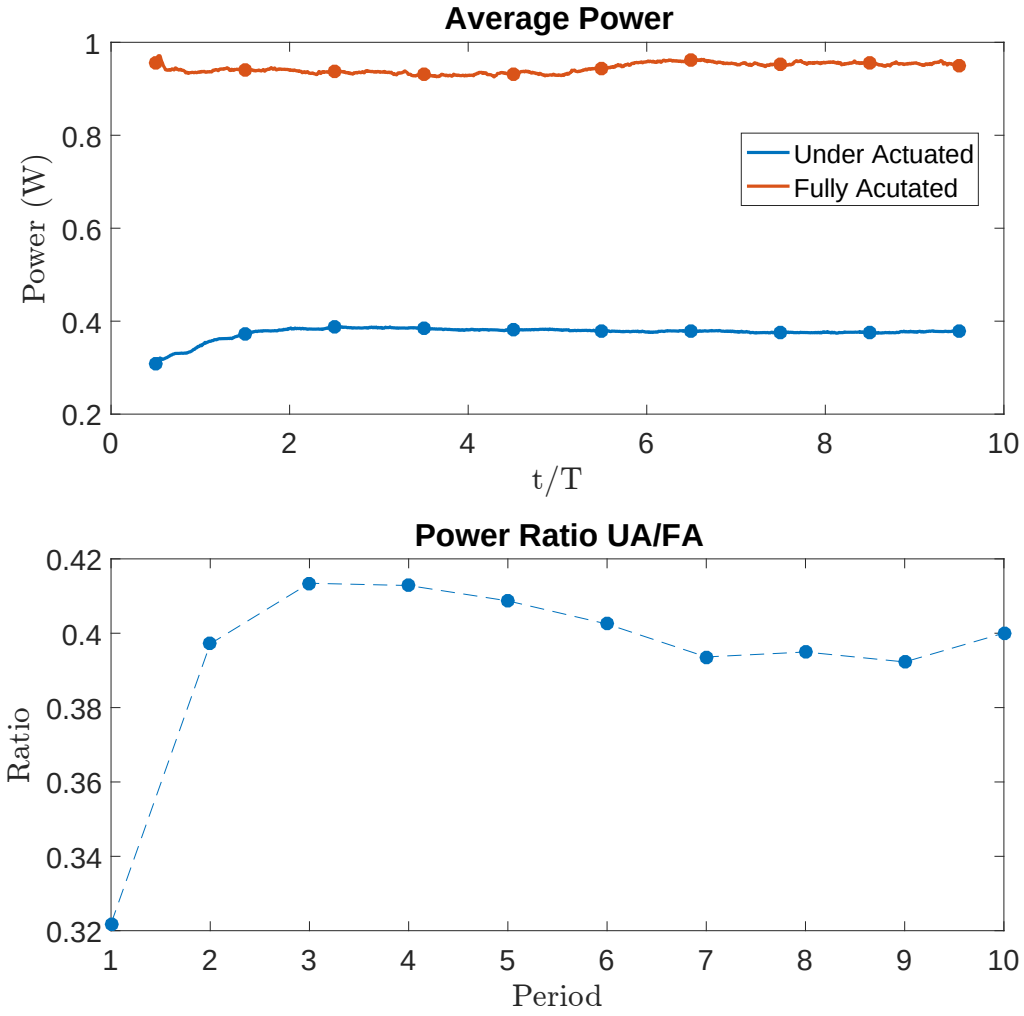

Figure 44: *Top:* Average power per cycle over ten cycles when driven at 0.5 Hz. *Bottom:* Power ratio at 0.5 Hz.

setting concern the optimal distribution of actuation and stiffness within such devices as well as optimal strategies for extracting efficient and diverse swimming gaits from them. But what of Boyle's "Custome & Education only"?

Fig. 46 depicts two views of the flattened toroidal joint-angle space of a swimming system described in [2], on which two components of the local curvature of the connection governing the system's locomotion are represented by variations in color. Atop

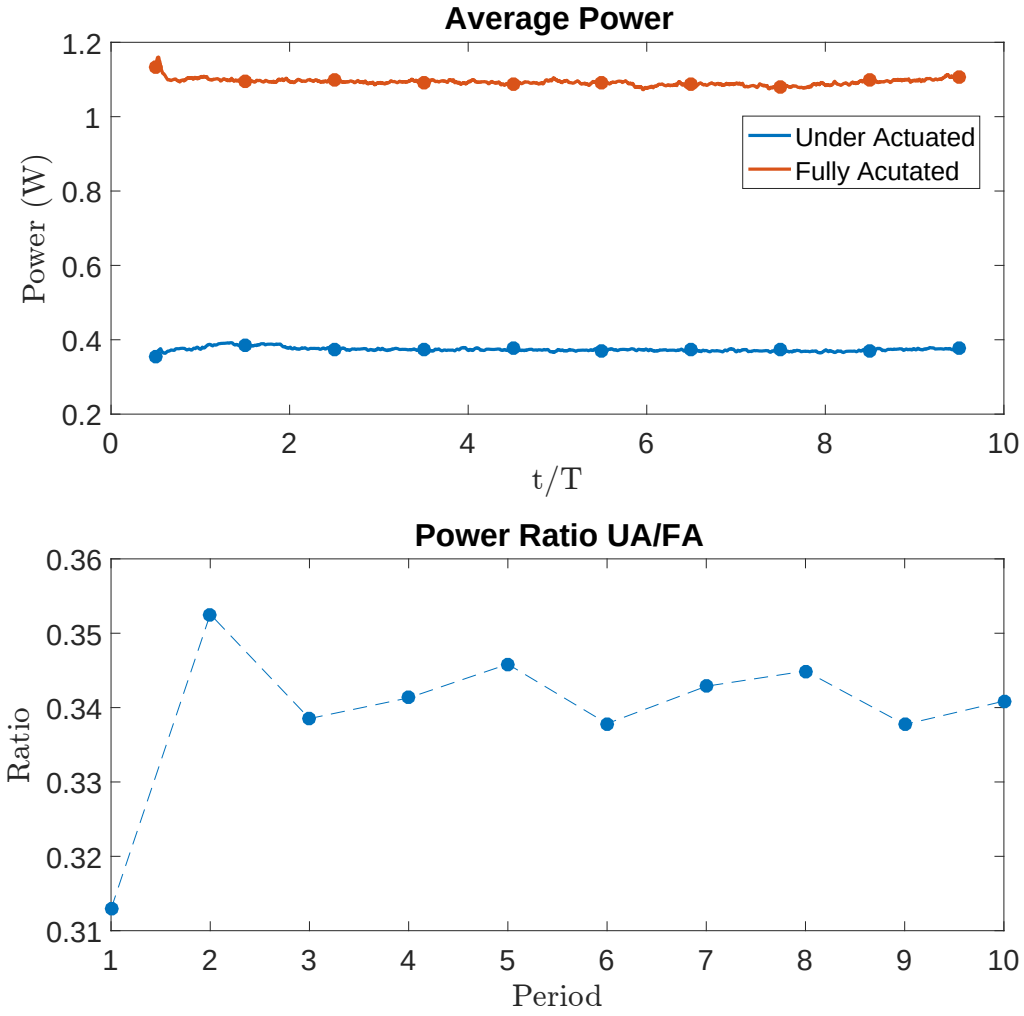

Figure 45: *Top:* Average power per cycle, over ten cycles when driven at 0.6 Hz. *Bottom:* Power ratio at 0.6 Hz.

each is superposed a four-step piecewise linear path optimized to achieve a certain locomotion objective, the path on the left exploiting the global topology of the torus to follow a zero-curvature contour.

These paths were obtained using *reinforcement learning*, a machine learning technique involving the episodic exploration of behaviors in search of optimal rewards ([8],[47]). Recent work by the authors of [2] and collaborators applies similar meth-

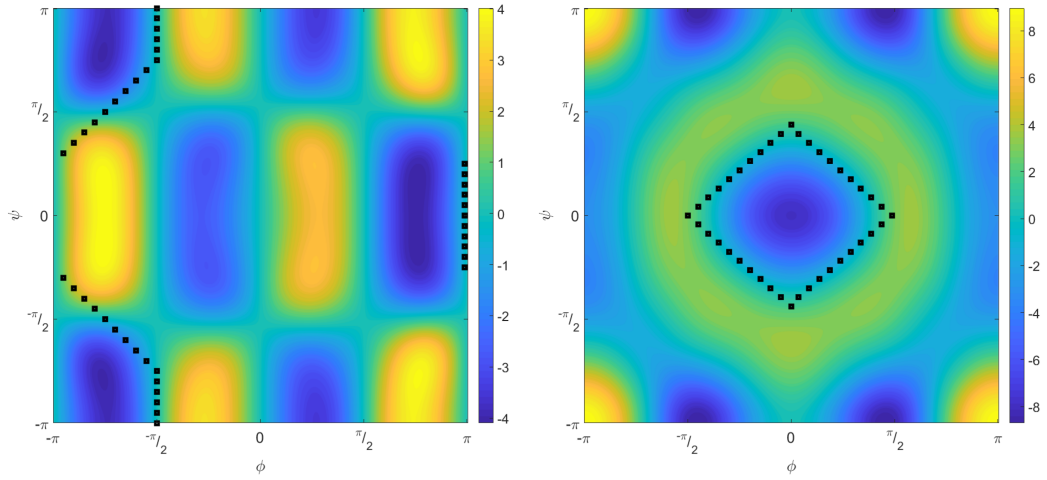

Figure 46: Piecewise linear enclosure of local curvature via reinforcement learning.

ods to the optimization of swimming gaits for elastically compliant swimmers like the singly actuated swimmer from the present work. Certainly the deployment of minimally actuated swimmers that learn for themselves how best to swim, without the prescription of controls by their designers, represents a goal aligned with Boyle's list.

CHAPTER 6: QUASISTEADY PARTICLE TRANSPORT IN SLOWLY VARYING PERIODIC FLOWS

6.1 Introduction

The ability to manipulate particles suspended in fluids on a micrometer scale has a variety of applications, some of which prohibit individual mechanical particle handling. The particles in question may be cells from a biological sample, to be separated according to cell type and tallied for cancer diagnosis ([17]), for instance, or they may be abrasive particles to be circulated in proximity to a brittle surface for precision machining ([36, 21]). The first of these applications illustrates the need for contact-free technology to manipulate fragile particles without risking damage to them. Both examples illustrate the need for high-throughput technology that can direct the sustained transport of particles without feedback control at the level of individual particle position.

To collect nutrients from their surroundings, sessile aquatic protozoa like *Vorticella* use vibrating cilia to drive streaming flows that transport nearby food particles to their mouths ([49]). Although a single such organism may possess many cilia, it's common for the cilia of a single organism to beat synchronously to drive a flow that can be characterized with relatively few parameters. Circulatory patterns like those observed near the mouth of a solitary feeding protozoan can even be established by

exciting a fluid with a single vibrating probe.[9] If a fluid is excited by several probes vibrating independently in proximity to each other, complex patterns of material transport can be created and manipulated by varying the amplitudes, frequencies, and directions of the probes' motion. This suggests a practicable approach for particle manipulation in engineered environments.

6.2 Particle Capture in Streaming Flows Driven by Vibrating Cylinders

A model based on an analytical representation (from [20]) of the flow near such a cylinder in the absence of particles was developed in [12]. While the addition of particles of arbitrary size may perturb such a flow significantly, sufficiently small particles represent a negligible perturbation. This is the premise of the *Maxey-Riley equations* (from [34]), which model the behavior of a small particle driven by a background flow by assuming that the flow dynamics are independent of the particle dynamics. The Maxey-Riley equation was used in [12] to demonstrate that small particles suspended in the fluid near a single vibrating cylinder will be attracted to the centers of four streaming cells that persist at locations arranged symmetrically around the cylinder's average position.

Fig. 47 illustrates this trapping of particles. The left panel depicts the flow in one quadrant adjacent to the cylinder, which is shown in grey. The cylinder vibrates from left to right, and the flow shown is mirrored in the three omitted quadrants. Although the flow is unsteady, the time-averaged trajectories of fluid particles — the time-averaged *Lagrangian streamlines* — are closed. Some such streamlines are

[9] Video footage of such an experiment, conducted by the third author of [3] , is visible at `http://kellyfish.net/insitutec.mov`. The probe in the video is roughly 6 μm thick.

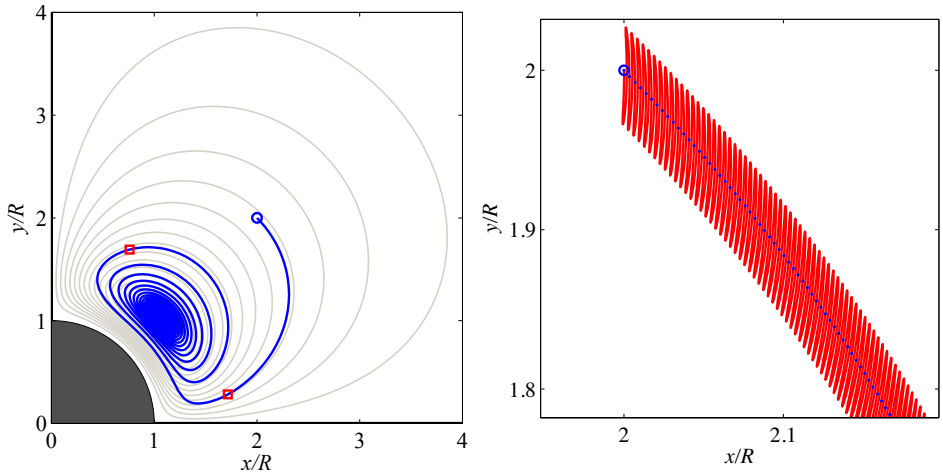

Figure 47: *Left:* The time-averaged trajectory of a small inertial particle against the backdrop of time-averaged Lagrangian streamlines in a flow with Reynolds number 40, described in detail in [12]. *Right:* A portion of the particle's actual trajectory (in red) with periodic samples exhibiting net motion (in blue).

shown in light grey. Fluid particles complete excursions around these streamlines slowly; each oscillation in the cylinder's position advances a fluid particle a small distance (in the net) along one of these streamlines. The small material displacement of the fluid by each cyclic variation in its boundary is known as *Stokes drift*, having first been analyzed (in the context of a different physical problem) in [46].

The right panel in Fig. 47 depicts (in red) a portion of the trajectory of an inertial particle driven by the background flow. This trajectory was computed by integrating the Maxey-Riley equations numerically. Since the fluid oscillates with the cylinder, so too does the particle, and the trajectory shown exhibits a significant high-frequency component. The net displacement of the particle after each oscillation is nonzero, however, and periodic sampling of the particle's position (in blue) reveals a distinct average trajectory. The blue spiral in the left panel represents a more extensive set of periodic samples from the particle's trajectory. The point on the blue spiral that's

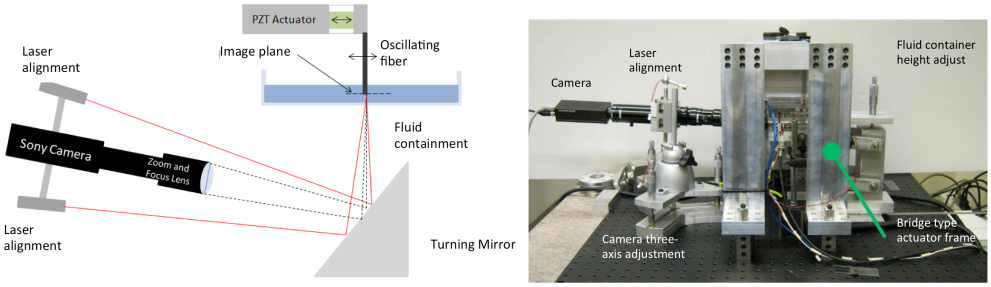

Figure 48: Apparatus for imaging particle transport near a solitary vibrating probe.

farthest from the cylinder is the particle's initial location; vibration of the cylinder induces the particle to migrate to the center of the innermost Lagrangian streamline.

6.3 Physical Model Validation

Fig. 48 depicts an experimental apparatus that's been developed to verify the phenomenon of particle capture shown in Fig. 47. A cylindrical probe half a millimeter thick protrudes downward from an aluminum flexure ([44]) into a petri dish containing water seeded with silvered glass beads. The flexure is driven piezoelectrically to cause the probe to vibrate laterally at a frequency adjustable up to 10 kHz. A horizontal plane containing a cross section of the probe away from its tip is imaged with a high-speed video camera.

The left side of Fig. 49 depicts still frames from footage captured using the system in Fig. 48. Each of the four frames in the top row represents the superposition of its predecessors (from left to right) with a subsequent still image. Each of the four frames in the bottom row is a close-up of the top left corner of the frame above, as indicated by the yellow box. The vibrating probe is seen in the center of each frame in the top row and in the corner of each frame in the bottom row. The blue circular disk overlapping the bottom right frame indicates the position and scale of the probe

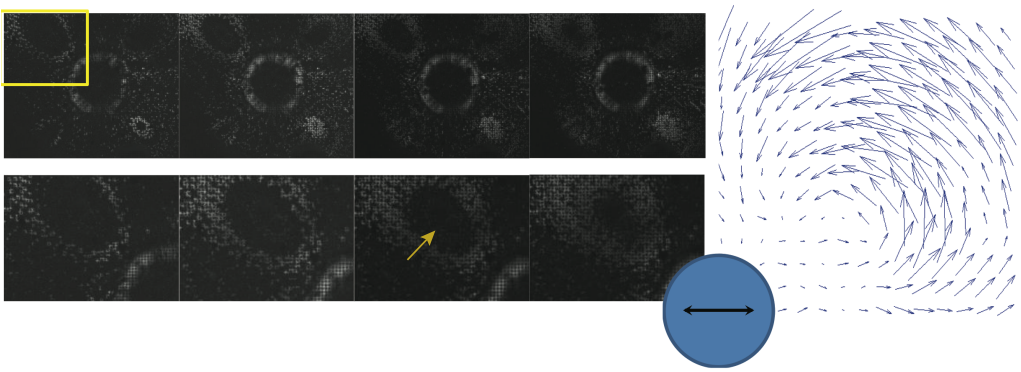

Figure 49: *Left:* Superposed frames from video captured using the apparatus from Fig. 48, indicating particle capture consistent with Fig. 47. *Right:* Velocity field data reconstructed from comparisons of particle positions in successive frames. The blue probe is positioned to fit both sides of the figure.

and its direction of motion.

The experiment depicted in Fig. 49 is preliminary, but the images clearly show that glass beads in proximity to the probe, visible as light pixels, spiral inward toward the centers of the four surrounding streaming cells. The leftmost frame in the bottom row depicts beads distributed around a cell with an unpopulated center. Each subsequent frame indicates increased migration of beads into this center, highlighted by the yellow arrow in the third panel.

The right side of Fig. 49 reconstructs the time-averaged velocity field representing the beads' motion around one streaming cell via *particle image velocimetry*, inferring velocity vectors from comparisons of sequential still images. Again, the blue circular disk indicates the probe's scale and direction of motion. Because the beads used in this experiment are small and neutrally dense, their velocities resemble the velocities of fluid particles and their time-averaged trajectories diverge only gradually from time-averaged Lagrangian streamlines. Because the probe vibrates thousands of times per

second, however, beads are captured in the centers of streaming cells within seconds.

6.4 Control via Geometric Phase

The concept of *geometric phase* applies when a cyclic change in some of the variables specifying a system's configuration engenders a net change in other such variables in a manner that's independent of time parametrization. Typically, the context is that of a system with a configuration manifold exhibiting a physically meaningful bundle structure. The configuration of a robotic vehicle that changes its internal shape to propel itself, for instance, corresponds to a point in a bundle over the manifold of points representing internal shapes. Fibers of this bundle are copies of the Lie group of translations and/or rotations of the vehicle in ambient space; the net translation and/or rotation associated with a cyclic shape change — in other words, the net resulting fiberwise displacement — represents a geometric phase if it's independent of the rate at which this change is executed. Robotic locomotion based on geometric phase was discussed in detail in [25].

Stokes drift provides another example of geometric phase. The deliberate displacement of fluid particles as a result of cyclic displacements in the position of a cylindrical probe was treated as a control problem in [37]. The objective therein was the design of trajectories in the manifold of probe positions to generate desired fiberwise displacements in a symplectic bundle over this manifold. The evolution of a fluid surrounding a moving probe consists exclusively of geometric phase in the driftless Reynolds-number extremes of ideal flow and Stokes flow; the mathematical parallelism between these physically diverse settings was discussed in [26].

In this chapter, we invoke the concept of geometric phase in the context of inertial particle transport near a pair of parallel probes like the probes in Figs. 47 and 49 vibrating independently in proximity to one another. The motion of each probe is parametrized by its axis, amplitude, and frequency of vibration. Each choice of these parameters determines a periodic flow characterized by a time-averaged Lagrangian streamline pattern akin to, but topologically more complex than, that in the left panel of Fig. 47. Inertial particles released into this flow will, over time, accumulate at trapping points corresponding to centers — or, presumably, to sufficiently stable spirals — in the averaged Lagrangian velocity field.

In general, if the parameters specifying the motion of the probes are varied gradually, trapping points in the flow will be displaced gradually, transporting trapped particles with them in a reversible manner. If flow parameters attain certain combinations of values, however, bifurcations in the averaged flow field may occur that cause trapping points to alter their character as fixed points or to vanish entirely. When a trapping point ceases to be attractive to inertial particles, the particles it carries will be released to converge to other trapping points. This process is irreversible; restoring a trapping point that's surrendered its particles won't recover these particles if they've been given time to settle at another trapping point.

Suppose that the parameters specifying the motion of the probes are varied in a cyclic manner, but that particles in the flow are given time at every step to converge to trapping points. If a cyclic excursion in parameter space induces no bifurcation in the time-averaged flow, then trapped particles will exhibit no net displacement at the end of each cycle. If a cycle involves one or more bifurcations, however, particles

trapped at a certain point at the beginning of the cycle may be trapped elsewhere at the end of the cycle, even though the original flow field has been restored. As long as the flow is deformed slowly relative to the migratory dynamics of untrapped particles, furthermore, the net transport of particles throughout the flow associated with a particular cyclic variation in parameters will depend only on the geometry of the loop executed in parameter space and not on its time parametrization.

In this last regard, the net transport of inertial particles associated with a slow cyclic deformation of the flow resembles the geometric phase associated with a closed path in a manifold on which coordinates correspond to directions, amplitudes, and frequencies of probe vibration. This phase corresponds to fiberwise motion within a bundle over the aforementioned manifold; points in each fiber correspond to arrangements of trapped particles within the flow. It is demonstrated explicitly in Section 6.5 (and reaffirmed in Section 7.5) that cyclic parametric variations can indeed produce bifurcations of the kind required for net particle transport.

6.5 Transport of Captured Particles via Periodic Flow Deformation

The Lagrangian streamline pattern depicted in the left panel of Fig. 47 is based on an analytical expression obtained in [20]. A simplified model for the same time-averaged flow field, limited in scope to the flow outside a thin boundary layer surrounding the cylinder, was developed in [42], where versions of the velocity field were obtained for the case in which no outer boundary is present and for the case in which a circular outer boundary is present.

In the present work, we model the flow transverse to a pair of vibrating probes by

superposing two copies of the bounded velocity field from [42], each parametrized to match the excitation due to one of the probes. This model is clearly an approximation, since the velocity field associated with either probe will fail to satisfy the boundary conditions on the other probe, and since the outer circular boundaries observed by the two individual fields will be misaligned. Sufficiently far from boundaries, however, we believe our model to represent the correct averaged velocity field with sufficient fidelity to warrant analysis.

[42] considered the flow around a transversely vibrating cylinder of radius r_1 enclosed by a circular boundary of radius R. The stream function Ψ is given in polar coordinates (r, ϕ) by

$$\Psi = A\left(\frac{C_1}{r^2} + C_2 + C_3 r^2 + C_4 r^4\right)\sin(2\phi) \tag{17}$$

with

$$A = -\frac{3}{2}\frac{s^2\omega}{r_1},$$

where s and ω are the magnitude and angular velocity of the oscillations, respectively. The boundary conditions are

$$-\frac{1}{r}\frac{\partial\Psi}{\partial\phi} = v_r = 0$$

on the bounding walls,

$$\frac{\partial\Psi}{\partial r} = v_\phi = A\sin(2\phi)$$

for $r = r_1$, and

$$v_\phi = 0$$

for $r = R$. For more details see [42].

Applying these boundary conditions, we can solve for the coefficients in (17) to obtain

$$\begin{aligned} C_1 &= -\frac{R^4\, r_1^3}{2\left(R^2 - r_1^2\right)^2}, \\ C_2 &= \frac{r_1\left(R^4 + 2\,R^2\, r_1^2\right)}{2\left(-R^2 + r_1^2\right)^2}, \\ C_3 &= -\frac{r_1\left(2\,R^2 + r_1^2\right)}{2\left(R^2 - r_1^2\right)^2}, \\ C_4 &= \frac{r_1}{2\left(-R^2 + r_1^2\right)^2}. \end{aligned}$$

The velocity field is given in polar coordinates by

$$\begin{aligned} v_r &= \frac{3s^2\omega\left(r^2 - R^2\right)^2\left(r^2 - r_1^2\right)\cos(2\phi)}{2r^3\left(R^2 - r_1^2\right)^2}, \\ v_\phi &= \frac{3s^2\omega\sin(\phi)\cos(\phi)\left(-2r^6 + r^4\left(2R^2 + r_1^2\right) - R^4 r_1^2\right)}{r^3\left(R^2 - r_1^2\right)^2} \end{aligned}$$

and in Cartesian coordinates by

$$\begin{aligned} \dot{x} =& \frac{3s^2\omega\, x\left(r_{xy}^2 - R^2\right)\left(R^2\left(r_1^2\left(x^2 - 3y^2\right) - x^4 + y^4\right) - \left(r_1^2 - x^2 - 3y^2\right)\left(r_{xy}^2\right)^2\right)}{2\left(R^2 - r_1^2\right)^2\left(r_{xy}^2\right)^3}, \\ \dot{y} =& -\frac{3s^2\omega\, y\left(r_{xy}^2 - R^2\right)\left(R^2\left(r_1^2\left(-3x^2 + y^2\right) + x^4 - y^4\right) - \left(r_1^2 - 3x^2 - y^2\right)\left(r_{xy}^2\right)^2\right)}{2\left(R^2 - r_1^2\right)^2\left(r_{xy}^2\right)^3}, \end{aligned} \tag{18}$$

where

$$r_{xy}^2 = x^2 + y^2.$$

We can use (18) to plot the average streamlines that result from the vibrations of the cylinder; such a plot is shown in Fig. 50. The stream plot shows four symmetric streaming cells. The four fixed points are linear centers, which implies that (according

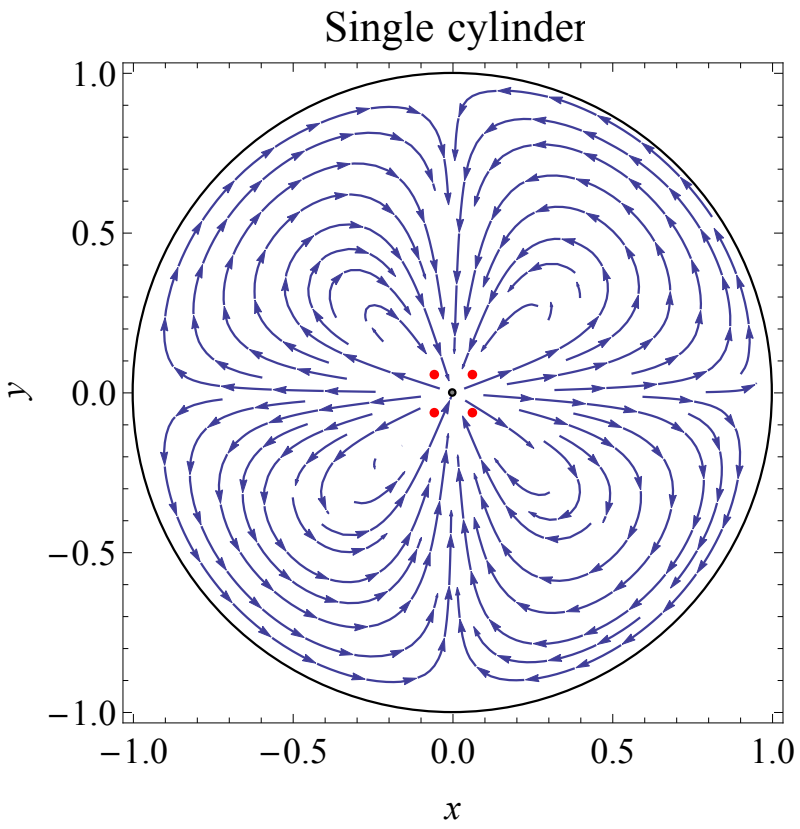

Figure 50: Streamlines generated by a solitary vibrating cylinder. Motion of the cylinder is parallel to the x-axis. The cylinder is indicated by the tiny grey disk in the center of the figure; the outer boundary of the region has a much larger radius than the cylinder in order to approximate the conditions of experiments like that shown in Fig 49. The four red dots represent the positions of fixed points in the velocity field. The parameters used to generate this plot were $s = 0.009$, $\omega = 3.1$, $r_1 = 0.01$, and $R = 1$.

to [12]) particles would be attracted to these locations. The positions of these fixed points depend only on the radii r_1 and R. The coordinates of the fixed points are (x_c, y_c), with

$$x_c = \pm \frac{\sqrt{\sqrt{r_1^2\left(8R^2 + r_1^2\right)} + r_1^2}}{2\sqrt{2}},$$

$$y_c = \pm \frac{\sqrt{\sqrt{r_1^2\left(8R^2 + r_1^2\right)} + r_1^2}}{2\sqrt{2}}.$$

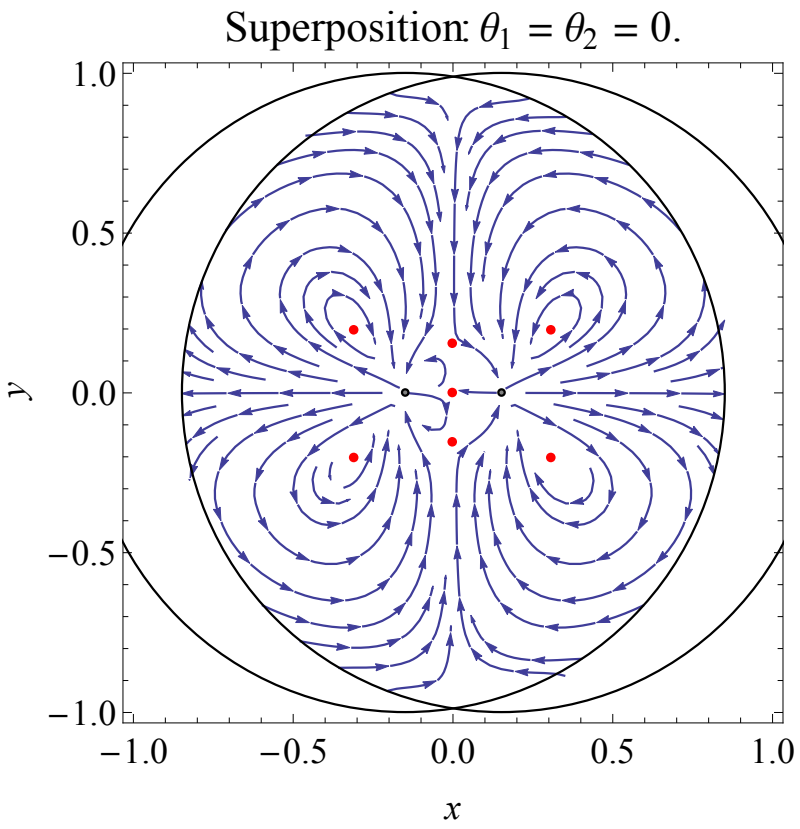

Figure 51: Superposition of two velocity fields created by the vibration of two cylinders with spacing of 0.3. Only the intersection of the two circular regions with radius R centered around the two cylinders is shown. (Axis labels will be omitted in further plots.)

The model with two vibrating cylinders is constructed by superposing the vector fields induced by two independent cylinders. To each cylinder we assign a parameter θ representing the angle between the direction of oscillation and the x-axis and an additional pair of parameters representing the cylinder's displacement from the origin.

The procedure to rotate and translate a cylinder (and the velocity field it generates) is as follows. If

$$\dot{x} = f(x, y), \qquad \dot{y} = g(x, y)$$

denote the velocity field given by (18) and $\mathfrak{R}(\theta)$ is a rotation matrix

$$\mathfrak{R}(\theta) = \begin{bmatrix} \cos\theta & -\sin\theta \\ \cos\theta & \sin\theta \end{bmatrix},$$

then the vector field rotated by the angle θ will be given by

$$\begin{bmatrix} \tilde{f}(x,y,\theta) \\ \tilde{g}(x,y,\theta) \end{bmatrix} = \mathfrak{R}(\theta) \begin{bmatrix} f(\mathfrak{R}(-\theta)[x,y]^T) \\ g(\mathfrak{R}(-\theta)[x,y]^T) \end{bmatrix}.$$

For translation from the origin to the point (h,k), we define the map

$$\mathfrak{T}: \begin{bmatrix} \tilde{f}(x,y) \\ \tilde{g}(x,y) \end{bmatrix} \mapsto \begin{bmatrix} \tilde{f}(x-h,y-k,\theta) \\ \tilde{g}(x-h,y-k,\theta) \end{bmatrix};$$

the rotated and translated vector field is given by

$$\begin{bmatrix} \dot{x} \\ \dot{y} \end{bmatrix} = \begin{bmatrix} \tilde{f}(x-h,y-k,\theta) \\ \tilde{g}(x-h,y-k,\theta) \end{bmatrix}. \tag{19}$$

We now consider the specific case of two cylinders, separated symmetrically along the x axis by a distance 0.3, with angles θ_1 and θ_2. This vector field can be obtained by the direct addition of two vector fields of the form (19), yielding

$$\begin{bmatrix} \dot{x} \\ \dot{y} \end{bmatrix} = \begin{bmatrix} \tilde{f}(x-h_1,y-k_1,\theta_1) + \tilde{f}(x-h_2,y-k_2,\theta_2) \\ \tilde{g}(x-h_1,y-k_1,\theta_1) + \tilde{g}(x-h_2,y-k_2,\theta_2) \end{bmatrix}$$

with $h_1 = -0.15$, $h_2 = 0.15$, and $k_1 = k_2 = 0$. A stream plot for this field with $\theta_1 = \theta_2 = 0$ can be seen in Fig. 51.

We next apply a cyclic variation to the control parameters θ_1 and θ_2, parametrized

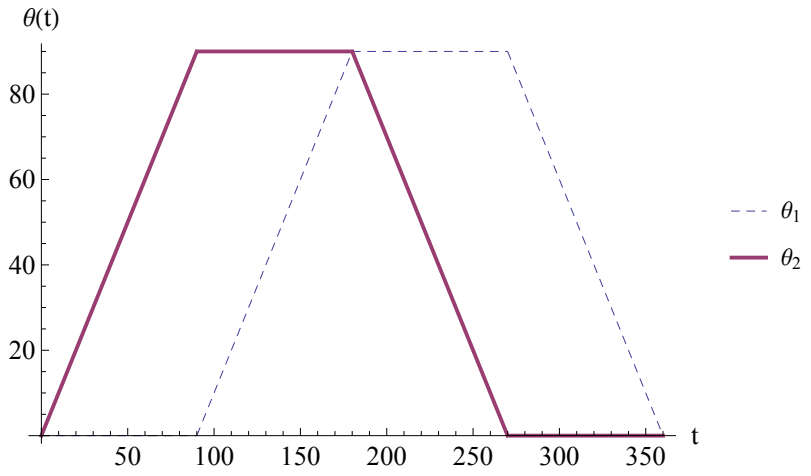

Figure 52: Time parametrization of θ_1 and θ_2.

in degrees as

$$\theta_1(t) = \begin{cases} 0 & 0 \le t \le 90 \\ t - 90 & 90 \le t \le 180 \\ 90 & 180 \le t \le 270 \\ -t + 360 & 270 \le t \le 360 \end{cases}, \qquad \theta_2(t) = \begin{cases} t & 0 \le t \le 90 \\ 90 & 90 \le t \le 180 \\ -t + 270 & 180 \le t \le 270 \\ 0 & 270 \le t \le 360 \end{cases}. \tag{20}$$

These functions are plotted against time in Fig. 52. In Fig. 53 we show a sequence of snapshots of the velocity field generated by the vibrating cylinders as θ_1 and θ_2 vary. For $\theta_1 = \theta_2 = 0$, the velocity field is the same as that shown in Fig. 51. We track the trajectory of one fixed point, shown as a dot in the top left panel of Fig. 53, in pink.

From $t = 0$ to $t = 180$, this fixed point moves smoothly from right to left, interacting closely with no other fixed point. At $t = 90$, the fixed point is clearly a center. From

$t = 180$ to $t = 268$, the fixed point and a saddle point approach each other. Right after $t = 268$, approximately when $\theta_1 = 1.7°$ and $\theta_2 = 90°$, a collision occurs in which the fixed point we've been tracking is annihilated.

Another bifurcation occurs shortly thereafter, when $t \approx 276$, and a new saddle point and spiral emerge nearby. These are seen as dots in the third panel in the middle row of Fig. 53; we now track their trajectories in pink. The spiral follows a trajectory thereafter that leads it to collide with another saddle and vanish shortly after $t = 312$. The saddle point survives the completion of the cyclic variation in θ_1 and θ_2, migrating to the location of one of the saddles that were visible at the beginning of the cycle.

This example represents only one of many cyclic variations that can be applied to the excitation of a pair of vibrating cylindrical probes, but it illustrates that such a cyclic variation can induce a fixed point that's initially attractive to inertial particles to migrate significantly from its initial location in the flow and then to vanish, releasing whatever particles it carried with it into the basin of attraction of a different fixed point. Though inducing no net change in the fluid velocity field, a cyclic change in flow parameters can thus result in the net redistribution of trapped inertial particles in the neighborhood of a pair of probes.

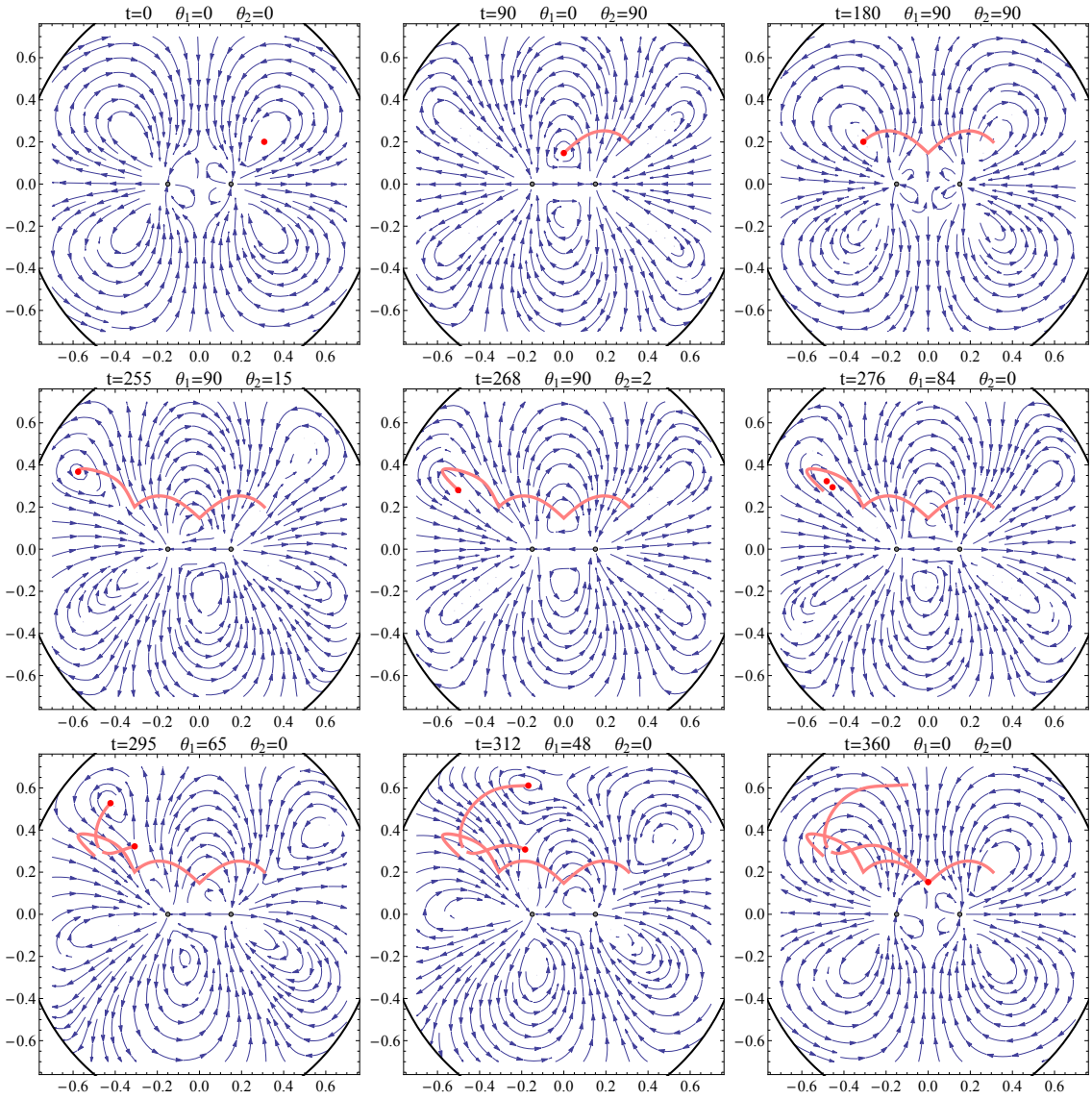

Figure 53: Sequence of stream plots generated as θ_1 and θ_2 vary through one cycle according to (20). The sequence goes from left to right, then from top to bottom.

CHAPTER 7: IMPROVING SIMULATIONS FOR PARTICLE TRANSPORT IN STREAMING CELLS

In Chapter 6 we used the simplified model from [42] to represent the streaming cells generated when a cylinder is vibrated in a fluid, instead of the full model used and obtained in [12], because the latter is very computational intensive. The idea has been to obtain an approximation of the model that can predict the trajectories inertial particles will follow in such a flow without having the computational burden. An alternate strategy was to use the time-averaged flow, that is the mean Lagrangian streamlines (from [12]), and integrate the Maxey-Riley [34] equations to obtain the trajectories of inertial particles. Here we present how to obtain such time-averaged flow and how the trajectories for inertial particles are obtained. We conclude this chapter showing some results using a high-fidelity simulation environment developed by a collaborator, which allows us to reaffirm the strategy proposed in Section 6 for quasisteady particle transport in periodic flows.

7.1 The Fluid Velocity Field

The flow is generated by sinusoidal oscillations, of amplitude A, of a cylinder of radius R, in a quiescient incompressible fluid of density ρ_f and kinematic viscosity ν. The position of the cylinder is given by

$$X(t) = e_x A \sin \Omega t.$$

The solution to this flow is taken from [12], which is based on the work presented in [20], where an analytical solution is given to the flow generated around a cylinder in an oscillatory free stream. [12] makes the appropriate changes so that now the cylinder is the one in motion and the fluid is at rest at infinity.

We first consider a cylinder at rest with the fluid at infinity in uniform oscillatory motion in the x direction, with velocity $U(t) = -A\Omega\cos(\Omega t)$. We seek the solution of the two-dimensional vorticity transport equation,

$$\frac{\partial}{\partial t}(\nabla^2\psi) + \boldsymbol{u}\cdot\nabla(\nabla^2\psi) = \nu\nabla^4\psi$$

subject to

$$\psi = 0,\ \ \frac{\partial\psi}{\partial r} = 0 \ \text{ at } \ r = R,$$

$$\psi \to -A\Omega r\sin\theta\cos\Omega t \ \text{ as } \ r\to\infty,$$

where the polar velocity components are defined as

$$u_r = \frac{1}{r}\frac{\partial\psi}{\partial\theta},\ \ u_\theta = -\frac{\partial\psi}{\partial r}.$$

From hereon, the variables are scaled by R and Ω. We now arrive at the dimensionless form of the problem

$$\nabla^2\left(\nabla^2 - Re\frac{\partial}{\partial t}\right)\psi = Re\,\boldsymbol{u}\cdot\nabla\left(\nabla^2\psi\right)$$

and

$$\psi = 0,\ \frac{\partial \psi}{\partial r} = 0 \ \text{ at } \ r = 1,$$

$$\psi \to -\epsilon r \sin\theta \cos t \ \text{ as } \ r \to \infty,$$

where $\epsilon = A/R$ and $Re = \Omega R^2/\nu$. We introduce an asymptotic expansion in ϵ for the streamfunction,

$$\psi = \epsilon\psi_1 + \epsilon^2\psi_2 + O(\epsilon^3)$$

and thereby develop a hierarchy of problems for ψ_1, ψ_2, etc. We will restrict our attention here to the first two,

$$\nabla^2 \left(\nabla^2 - Re \frac{\partial}{\partial t} \right) \psi_1 = 0, \tag{21}$$

$$\psi_1 = 0,\ \frac{\partial \psi_1}{\partial r} = 0 \ \text{ at } \ r = 1,$$

$$\psi_1 \to -r \sin\theta \cos t \ \text{ as } \ r \to \infty$$

and

$$\nabla^2 \left(\nabla^2 - Re \frac{\partial}{\partial t} \right) \psi_2 = Re\, \boldsymbol{u}_1 \cdot \nabla \left(\nabla^2 \psi_1 \right), \tag{22}$$

$$\psi_2 = 0,\ \frac{\partial \psi_2}{\partial r} = 0 \ \text{ at } \ r = 1,$$

$$\psi_2 \to 0 \ \text{ as } \ r \to \infty.$$

7.1.1 First-Order Solution

The solution for (21) can be written as

$$\psi_1(r, \theta, t) = \mathrm{Re}\left(\Psi_1(r) \mathrm{e}^{-\mathrm{i}\, t} \right) \sin\theta,$$

where the radial dependence can be split into two parts

$$\Psi_1(r) = \Psi_1^{(1)}(r) + \Psi_1^{(2)}(r),$$

each representing the homogeneous solution of one of the two differential operators in (21). $\Psi_1^{(1)}$ is the radial dependence of the solution of the Laplace equation and $\Psi_1^{(2)}$ of the heat equation. Applying boundary conditions the solutions are:

$$\begin{aligned} \Psi_1^{(1)}(r) &= -r - \frac{C}{r}, \\ \Psi_1^{(2)}(r) &= \frac{2H_1^{(2)}(\gamma\, r)}{\gamma\, H_0^{(1)}(\gamma)} = r\left[\frac{H_0^{(1)}(\gamma\, r)}{H_o^{(1)}(\gamma)} + \frac{H_2^{(1)}(\gamma\, r)}{H_0^{(1)}(\gamma)}\right], \end{aligned} \tag{23}$$

where $C = H_2^{(1)}(\gamma)/H_0^{(1)}(\gamma)$. Note that $H_1^{(1)}$ and $H_1^{(2)}$ are the first-order Hankel functions of the first and second kind, respectively, and $\gamma = (\mathrm{i}\, Re)^{1/2}$. To express the streamfunction in the inertial reference frame, cylinder oscillating and fluid at rest in infinity, the first term in (23) is cancelled by the first order modification, see [12]. The associated velocity components with this first-order streamfunction are

$$u_{r,1} = \mathrm{Re}\left(U_{r,1}(r)\mathrm{e}^{-\mathrm{i}\, t}\right)\cos\theta$$

and

$$u_{\theta,1} = \mathrm{Re}\left(U_{\theta,1}(r)\mathrm{e}^{-\mathrm{i}\, t}\right)\sin\theta,$$

where $U_{r,1} = \Psi_1/r$ and $U_{\theta,1} = -\mathrm{d}\Psi_1/\mathrm{d}r$. It can be shown that

$$\begin{aligned} U_{r,1}(r) &= -1 - \frac{C}{r^2} + \frac{H_0^{(1)}(\gamma\, r)}{H_0^{(1)}(\gamma)} + \frac{H_2^{(1)}(\gamma\, r)}{H_0^{(1)}(\gamma)}, \\ U_{\theta,1}(r) &= 1 - \frac{C}{r^2} - \frac{H_0^{(1)}(\gamma\, r)}{H_0^{(1)}(\gamma)} + \frac{H_2^{(1)}(\gamma\, r)}{H_0^{(1)}(\gamma)}. \end{aligned}$$

7.1.2 Second-Order Solution

The first-order solution can now be used to evaluate the forcing term in (22) for ψ_2. This leads to a second-order solution of the form

$$\psi_2(r,\theta,t) = \mathrm{Re}\left(\Psi_2^s(r) + \Psi_2(r)\mathrm{e}^{-\mathrm{i}2t}\right)\sin 2\theta,$$

where the radial dependence of the steady solution is

$$\begin{aligned}\Psi_2^s(r) = &-\frac{r^4}{48}\int_r^\infty \frac{f_0(\tau)}{\tau}\mathrm{d}\tau + \frac{r^2}{16}\int_r^\infty \tau\, f_0(\tau)\mathrm{d}\tau \\ &+\frac{1}{16}\left(\int_1^r \tau^3 f_0(\tau)\mathrm{d}\tau + \int_1^\infty \frac{f_0(\tau)}{\tau}\mathrm{d}\tau\right. \\ &\left.-2\int_1^\infty \tau\, f_0(\tau)\mathrm{d}\tau\right) + \frac{1}{r^2}\left(-\frac{1}{48}\int_1^r \tau^5\, f_0(\tau)\mathrm{d}\tau\right. \\ &\left.-\frac{1}{24}\int_1^\infty \frac{f_0(\tau)}{\tau}\mathrm{d}\tau + \frac{1}{16}\int_1^\infty \tau\, f_0(\tau)\mathrm{d}\tau\right),\end{aligned}$$

where

$$f_0(r) = \frac{\mathrm{i}\,\mathrm{Re}^2}{4}\frac{1}{r}\left(\Psi_1\frac{\mathrm{d}\Psi_1^{(2)*}}{\mathrm{d}r} - \Psi_1^{(2)*}\frac{\mathrm{d}\Psi_1}{\mathrm{d}r}\right).$$

The radial dependence of the oscillatory portion is

$$\begin{aligned}\Psi_2(r) = &\frac{\mathrm{i}\,\pi}{4\,\lambda^2 H_1^{(1)}(\lambda)}\left(H_2^{(1)}(\lambda\, r)\int_1^r \tau\, K_2(\lambda\tau)g_0(\tau)(d)\tau\right. \\ &\left.+K_2(\lambda\, r)\int_r^\infty \tau H_2^{(1)}(\lambda\,\tau)g_0(\tau)\mathrm{d}\tau\right) \\ &+\frac{1}{\lambda^3 H_1^{(1)}(\lambda)}\left[\left(H_2^{(1)}(\lambda\, r) - r^{-2}H_2^{(1)}(\lambda)\right)\right. \\ &\left.\int_1^\infty \frac{g_0(\tau)}{\tau}\mathrm{d}\tau + r^{-2}\int_1 \infty\tau\, H_2^{(1)}(\lambda\,\tau)g_0(\tau)\mathrm{d}\tau\right] \\ &-\frac{1}{4\lambda^2}\left(r^2\int_r^\infty \frac{g_0(\tau)}{\tau}\mathrm{d}\tau - r^{-2}\int_1^\infty \frac{g_0(\tau)}{\tau}\mathrm{d}\tau\right. \\ &\left.+r^{-2}\int_1^r \tau^3 g_0(\tau)\mathrm{d}\tau\right),\end{aligned}$$

where $\lambda = \sqrt{2}\gamma$, $K_2(\lambda\tau) = H_1^{(1)}(\lambda)H_2^{(2)}(\lambda\tau) - H_1^{(2)}(\lambda)H_2^{(1)}(\lambda\tau)$, and

$$g_0(r) = -\frac{\mathrm{i}\,Re^2}{4r}\left(\Psi_1^{(1)}\frac{\mathrm{d}\Psi_1^{(2)}}{\mathrm{d}r} - \Psi_1^{(2)}\frac{\mathrm{d}\Psi_1^{(1)}}{\mathrm{d}r}\right).$$

The velocity components of the second order solution are,

$$u_{r,2} = \mathrm{Re}\left(\frac{2\Psi_2^s}{r} + \frac{2\Psi_2}{r}\mathrm{e}^{-\mathrm{i}2t}\right)\cos 2\theta \tag{24}$$

and

$$u_{\theta,2} = -\mathrm{Re}\left(\frac{\mathrm{d}\Psi_2^s}{\mathrm{d}r} + \frac{\mathrm{d}\Psi_2}{\mathrm{d}r}\mathrm{e}^{-\mathrm{i}2t}\right)\sin 2\theta. \tag{25}$$

The corrected form of the second-order streamfunction in the inertial reference frame can be obtained by making the replacements

$$\Psi_2^s \to \Psi_2^s - \frac{\mathrm{i}}{4}(U_{r,1} + U_{\theta,1}),$$
$$\Psi_2 \to \Psi_2 + \frac{\mathrm{i}}{4}(U_{r,1} + U_{\theta,1})$$

The corresponding corrected second-order velocity components can be obtained from (24) and (25) after using this replacement rules.

The total velocity components using the first and second-order solutions will be given by the following:

$$u_r = \epsilon\, u_{r,1} + \epsilon^2\, u_{r,2}, \tag{26}$$

$$u_\theta = \epsilon\, u_{\theta,1} + \epsilon^2\, u_{\theta,2}. \tag{27}$$

7.1.3 Lagrangian streamfunction

The steady portion of the streamfunction, Ψ_2^s represents the Eulerian streamlines of the flow. However, fluid particles in average do not follow this streamlines, they follow

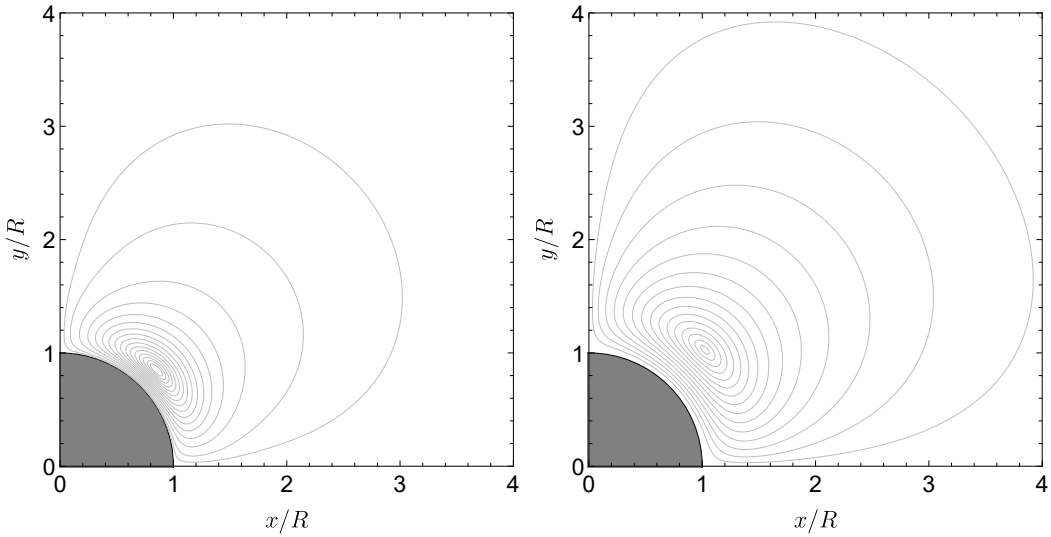

Figure 54: *Left:* Eulerian streamlines. *Right:* Lagrangian streamlines. ($Re = 40$)

the Lagrangian streamlines. The radial dependence of the Lagrangian streamfunction is given by

$$\begin{aligned}\Psi^L(r) =& \Psi_2^s(r) + \frac{1}{2}\mathrm{Im}\left[-\frac{C}{r^2} + \frac{H_2^{(1)}(\gamma\, r)}{H_0^{(1)}(\gamma)}\right] \\ &+ \frac{1}{2}\mathrm{Im}\left[\left(\frac{C}{r^2} - \frac{H_2^{(1)}(\gamma\, r)}{H_0^{(1)}(\gamma)}\right)\left(\frac{H_0^{(1)}(\gamma\, r)}{H_0^{(1)}(\gamma)}\right)^*\right].\end{aligned} \tag{28}$$

The second term in (28) accounts for the change of frame of reference, cylinder oscillating and fluid at rest at infinity. The third term represents the Stokes drift, for more details see [12]. The difference between Eulerian and Lagrangian streamlines can be seen in Figure 54. The Lagrangian streamfunction is given by

$$\psi^L(r,\theta) = \mathrm{Re}\left(\Psi^L(r)\right)\sin 2\theta.$$

7.2 The Maxey-Riley Equations

To calculate the trajectories followed by inertial particles, we numerically integrate the Maxey-Riley (MR) equation [34] with Saffman lift force [41]. Ignoring gravity terms, the MR equation may be expressed as is shown in (29).

$$\begin{aligned}
\frac{\mathrm{d}\mathbf{X}_p}{\mathrm{d}t} &= \mathbf{V}_p \\
m_p\frac{\mathrm{d}\mathbf{V}_p}{\mathrm{d}t} &= -6\pi\rho_f\nu a\left[\mathbf{V}_p(t)-\mathbf{u}(\mathbf{X}_p(t),t)-\frac{1}{6}a^2\nabla^2\mathbf{u}(\mathbf{X}_p(t),t)\right]+m_f\left.\frac{\mathrm{D}\,\mathbf{u}}{\mathrm{D}\,t}\right|_{\mathbf{X}_p(t)} \\
&\quad -\frac{1}{2}m_f\left(\frac{\mathrm{d}\,\mathbf{V}_p}{\mathrm{d}\,t}-\left.\frac{\mathrm{D}\,\mathbf{u}}{\mathrm{D}\,t}\right|_{\mathbf{X}_p(t)}-\frac{\mathrm{d}}{\mathrm{d}\,t}\left[\frac{1}{10}a^2\nabla^2\mathbf{u}(\mathbf{X}_p(t),t)\right]\right) \\
&\quad -6\pi^{1/2}\nu^{1/2}a^2\rho_f\int_{-\infty}^{t}B(\tau)\,\mathrm{d}\,\tau+4K\,\rho_f a^2(\nu\,|G|)^{1/2}\mathrm{sgn}(G)\,|\mathbf{u}-\mathbf{V}_p|\,\mathbf{n},
\end{aligned} \tag{29}$$

where

$$B(\tau)=\frac{\frac{\mathrm{d}}{\mathrm{d}\tau}\left[\mathbf{V}_p(\tau)-\mathbf{u}(\mathbf{X}_p(\tau),\tau)-\frac{1}{6}a^2\nabla^2\mathbf{u}(\mathbf{X}_p(\tau),\tau)\right]}{\sqrt{t-\tau}},$$

$$\begin{aligned}
G=|\mathbf{u}-\mathbf{V}_p|^{-}\,2\Bigg[&(u_x-V_{p,x})^2\frac{\partial u_x}{\partial y}-(u_y-V_{p,y})^2\frac{\partial u_y}{\partial x} \\
&-(u_x-V_{p,x})(u_y-V_{p,y})\left(\frac{\partial u_x}{\partial x}-\frac{\partial u_y}{\partial y}\right)\Bigg]
\end{aligned}$$

and

$$\mathbf{n}=|\mathbf{u}-\mathbf{V}_p|^{-1}\left[-(u_y-V_{p,y})\,\mathbf{e}_x+(u_x-V_{p,x})\,\mathbf{e}_y\right].$$

In (29) $\mathbf{X}_p$ is the particle's position and $\mathbf{V}_p$ is its velocity, m_p and m_f are the particle's mass and mass of the displaced fluid respectively. The densities of the particle and fluid are ρ_p and ρ_f respectively. The particle has radius a and the fluid has kinematic viscosity ν. The symbol K is the Saffman constant with value 1.615. The operators

$\mathrm{d}/\mathrm{d}\,t$ and $\mathrm{D}/\mathrm{D}\,t$ are defined as follows:

$$\frac{\mathrm{d}\,\mathbf{u}}{\mathrm{d}\,t} = \frac{\partial\,\mathbf{u}}{\partial\,t} + \mathbf{V}_p \cdot \nabla\mathbf{u}, \qquad\qquad \frac{\mathrm{D}\,\mathbf{u}}{\mathrm{D}\,t} = \frac{\partial\,\mathbf{u}}{\partial\,t} + \mathbf{u} \cdot \nabla\mathbf{u}.$$

The terms on the right hand side of (29) represent the viscous Stokes drag, fluid acceleration force, added mass, Basset history force and Saffman lift, respectively.

The relative velocity between inertial particle and the fluid is defined as $\boldsymbol{\omega} = \mathbf{V}_p - \mathbf{u}(\mathbf{X}_p)$. With this slip velocity, we get the following derivatives relationship:

$$\frac{\mathrm{D}\,\mathbf{u}}{\mathrm{D}\,t} = \frac{\mathrm{d}\,\mathbf{u}}{\mathrm{d}\,t} - \boldsymbol{\omega} \cdot \nabla\mathbf{u}. \tag{30}$$

Using $\boldsymbol{\omega}$, the relationship given by (30), and non-dimensionalizing the variables using Ω and R as was done for the fluid velocity field, we rewrite the MR equation (29) as shown in (31). We have dropped the Basset term, as it is not used for the present work, it was shown in [12] that this force is negligible.

$$\begin{aligned}\left(\frac{\rho_p}{\rho_f} + \frac{1}{2}\right)\frac{\mathrm{d}\,\boldsymbol{\omega}}{\mathrm{d}\,t} = &-\frac{9}{2}Re_a^{-1}\boldsymbol{\omega} + (1-\rho_p/\rho_f)\left.\frac{\mathrm{d}\,\mathbf{u}}{\mathrm{d}\,t}\right|_{\mathbf{X}_p(t)} - \left.\frac{3}{2}\boldsymbol{\omega}\cdot\nabla\mathbf{u}\right|_{\mathbf{X}_p(t)} \\ &+ 3K\,\pi^{-1}Re_a^{-1/2}|G|^{1/2}\mathrm{sgn}(G)|\boldsymbol{\omega}|\mathbf{n} + \frac{3}{4}Re_a^{-1}(a/R)^2\nabla^2\mathbf{u}(\mathbf{X}_p(t),t) \\ &+ \frac{1}{20}(a/R)^2\frac{\mathrm{d}}{\mathrm{d}\,t}\left[\nabla^2\mathbf{u}(\mathbf{X}_p(t),t)\right]\end{aligned} \tag{31}$$

Here, $Re_a = \Omega\,a^2/\nu = Re(a/R)^2$ is a particle-based Reynolds number. The direction of the Saffman lift is given by $\mathbf{n} = \hat{\boldsymbol{\omega}} \times \mathbf{e}_z$, where $\hat{\boldsymbol{\omega}} = \boldsymbol{\omega}/|\boldsymbol{\omega}|$. The generalized shear rate can be expressed as $G = -\mathbf{n}\cdot\nabla\mathbf{u}\cdot\hat{\boldsymbol{\omega}}$.

7.3 Averaging the Flow Versus Averaging Particle Trajectories

In [12] the inertial particle trajectories were obtained by integrating the MR Equation using the full oscillatory fluid velocity field given by Eqns. (26) and (27), then they were stroboscopically sampled once every oscillation to give the "averaged" trajectory, such a trajectory can be seen in the left panel of Fig. 47. Instead of solving with the full time-varying velocity field and then stroboscopically average the trajectory, we have used a time-averaged velocity field to integrate the MR Equation. This time-averaged velocity field is obtained from the Lagrangian streamfunction, (28). The velocity components are given by

$$u_{r,L} = \frac{1}{r}\frac{\partial \psi^L}{\partial \theta}, \qquad u_{\theta,L} = -\frac{\partial \psi^L}{\partial r}. \tag{32}$$

7.4 Particles in the Lagrangian averaged flow

Fig. 55 shows the trajectories obtained for spherical inertial particles (with normalized radius $a/R = 0.175$) released at three different locations inside a streaming cell. The velocity field is that given by the light gray Lagrangian streamlines, from (32).

It can be seen that trajectories don't follow the same path as when the full oscillatory velocity field is used with the MR equation. Using the full model, all particles starting inside the streaming cell, spiral in and get trapped, as seen in the left panel of Fig. 47. However, some interesting dynamics occur, particles starting far out do spiral in to what seems to be a limit cycle, blue trajectory in Fig. 55. Particles released a little more inside of the streaming cell spiral out and reach the same limit

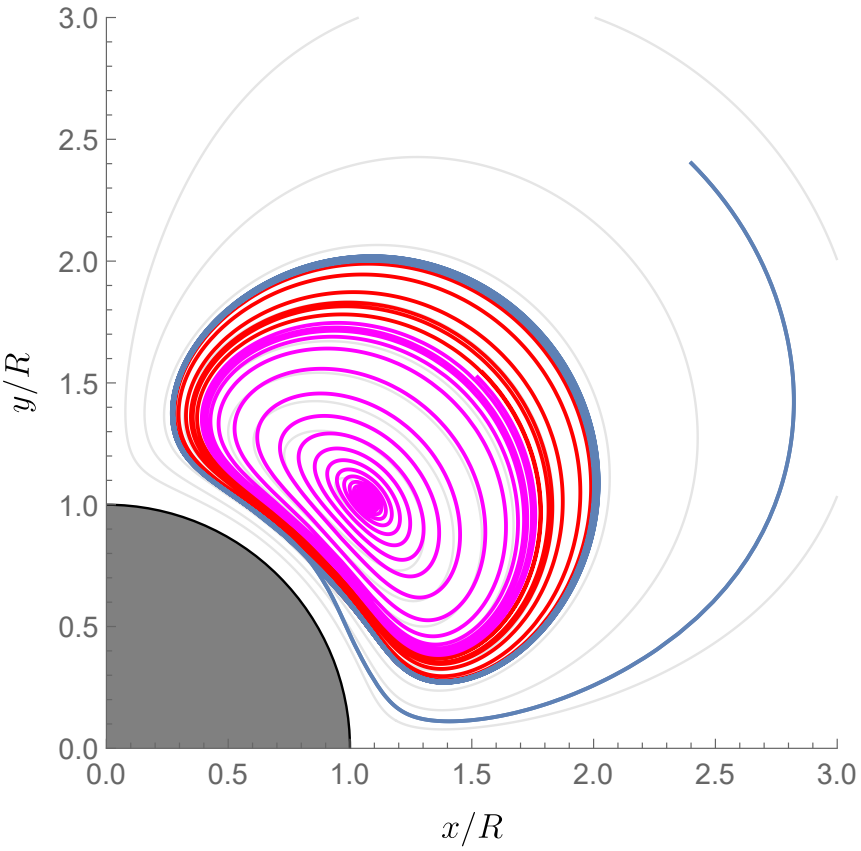

Figure 55: Trajectories followed by inertial particles released at different locations with $a/R = 0.175$ and $Re = 40$.

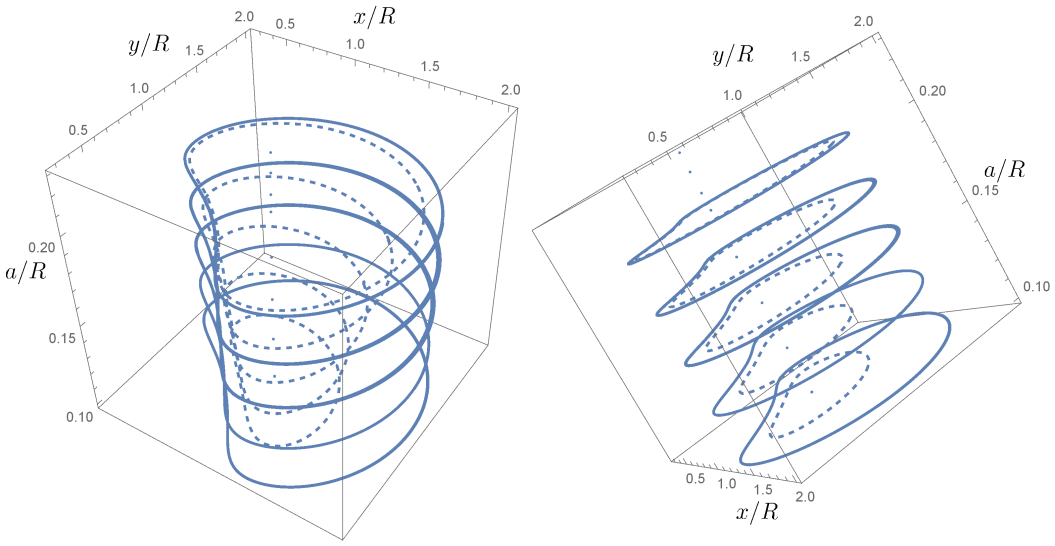

Figure 56: Bifurcation diagram, as a/R takes the following values: 0.1, 0.125, 0.140, 0.175,0.2, 0.209,0.22 and 0.23 with $Re = 40$.

cycle, red trajectory. Start closer to the center of the cell and now the trajectories spiral in to a fix point. The system then, exhibits two "concentric" limit cycles, the outer one is stable and the inner one unstable, with a stable fix point in the center of the cell.

Furthermore, more interesting things happen to the system when we vary the size of the inertial particles, i.e., vary a/R. Fig. 56 summarizes the trajectories that inertial particles of different sizes would generate, depending of their initial position they will spiral towards one of the limit cycles or to the fix point in the center of the cell. It can also be seen that approximately at size $a/R = 0.2$ the two limit cycles collapse. Interesting but does not show the same behavior as the full system.

7.5 Using High-Fidelity Simulations for Particle Transport in arrays of Vibrating Cylinders

In chapter 6, a strategy of using two probes for which their direction of oscillation varies in a cyclic way was suggested, such that the fix points in the streaming cells could be moved in the plane. And not only that, but geometric phase could be achieved in the sense that particles originally trapped in one cell could end up in a different one.

Another strategy that allows the transport of particles from one location using arrays of oscillating probes was introduced in [13]. The strategy consists of exciting one probe at a time, allowing the particles to be trapped in one of its streaming cells and then stop excitation and excite another probe, so that particles would jump from one trapping region to another on the proximity of another cylinder. This strategy has the limitation of only trapping particles next to a probe.

We now propose exploring strategies similar to that of chapter 6, where more than one probe vibrates at the same time, this will allow for the structure of the streaming cells to interact. What we would like to find is a strategy that allows us to move — at least quasisteadily — the streaming cells to new locations and the inertial particles with them.

We have now been able to test strategy proposed in Chapter 6 using a high-fidelity model provided by one of the authors in [12] and [13]. The new simulation environment has been implemented in Julia.[10] This environment allows for easy change

[10] Julia is a high-level, high-performance dynamic programming language for numerical computing. `https://julialang.org/`

in the parameters of simulations where one can add vibrating probes in arbitrary locations.

Fig. 57 shows the results obtained after simulating two probes in a fluid and varying the orientation of the oscillations as was done in Chapter 6. Each probe is assigned an angle θ_i that determines the direction of oscillations. θ_i is parametrized by (20), θ_1 belongs to the probe on the left and θ_2 belongs to the probe on the right. The simulation was done with $\epsilon = 0.1$ and $Re = 40$. The probes were placed 2 diameters apart. Inspecting the different frames from Fig. 57, it can be seen that particles that start trapped in a streaming cell may end in a different cell after a full cycle. We number the streaming cells 1 through 8 when $\theta_1 = \theta_2 = 0$ (first or last frame from Fig. 57), such that cell one is in the top-right corner and we number the rest in a counter-clockwise manner ending with cell eight in the bottom right corner. Using this numbering scheme, Table 2 summarizes where do particles end up after a cycle if they were initially trapped in a cell. We assume the changes in θ_i happen slow enough to allow particles to get trapped and move with the streaming cells. We could think of this cyclic actuation as a discrete map between regions where particles are trapped.

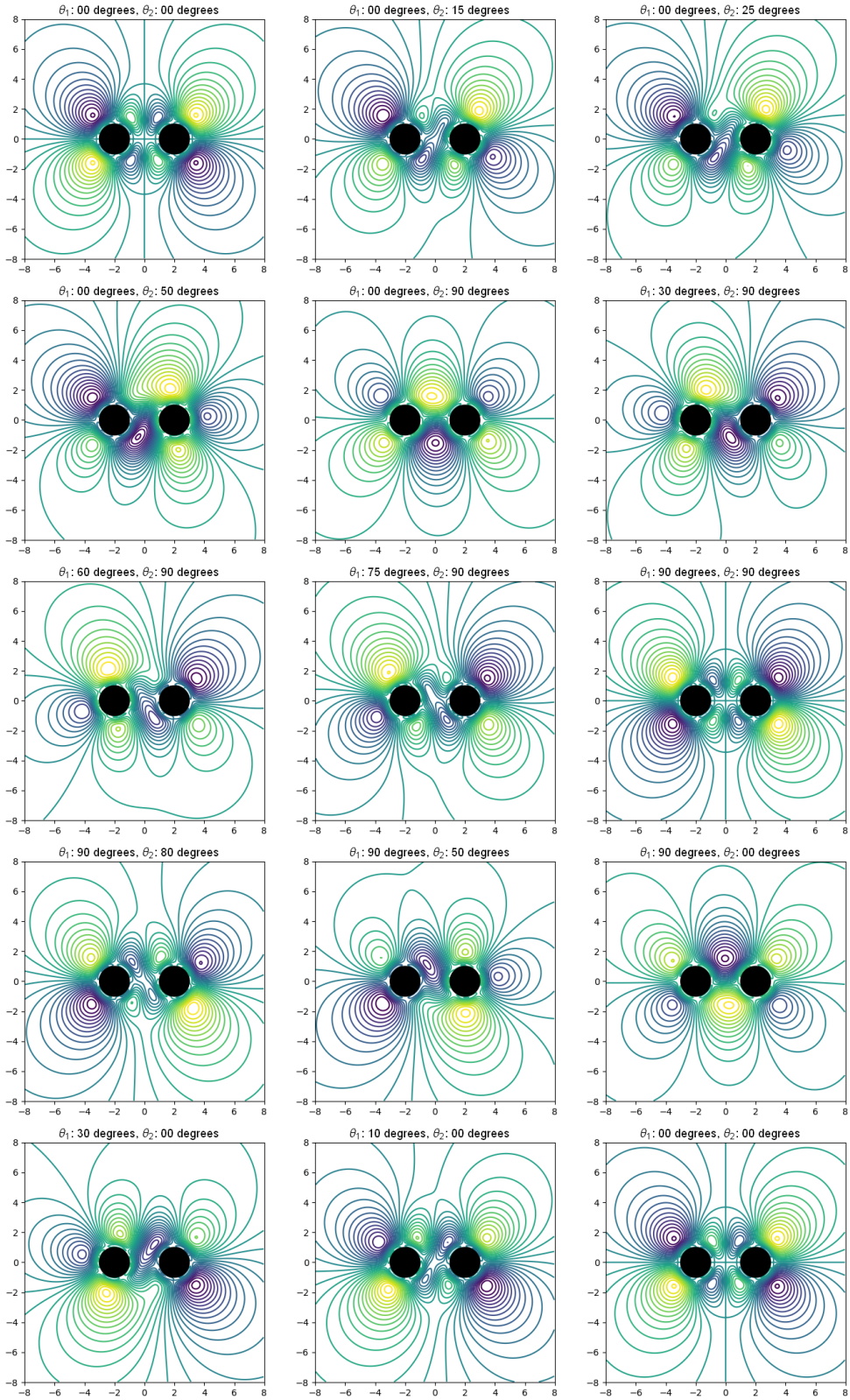

Figure 57: Sequence of average streamlines generated as θ_1 and θ_2 vary through one cycle according to (20) using the high-fidelity model. The sequence goes from left to right, then from top to bottom.

Table 2: Where do particles end up after one cycle as parametrized by (20).

Starting Cell	Ending Cell
1	3
2	2
3	3
4	4
5	5
6	2
7	5
8	8

CHAPTER 8: CONTRIBUTIONS AND FUTURE WORK

8.1 Contributions

We have documented and characterized the phenomenon of damping-induced self recovery in a class of robotic swimmers with an internal rotor. We have also observed and documented a saturation phenomenon when the robot tries to rotate continuously. We found a criterion that needs to be satisfied for this saturation to exist. A strategy to minimize the self recovery is also proposed.

We experimentally verified the use of a PI controller that allows us to control the heading and speed of a class of robotic vehicles with an internal rotor and with single actuation. Swimming and a terrestrial robotic system were tested. The terrestrial vehicle, Chaplygin beanie, is a nonholonomic system, we have built the first physical representation of this system.

For control systems whose underlying physics justify a model based on a principal connection, we have devised a technique that allows us to estimate the local curvature. A limited sampling of the system's responsiveness to select inputs can be used to estimate the curvature, from which the system's response to an arbitrary periodic input can then be estimated in the absence of a theoretical model.

Again, for systems whose model are based on a principal connection, we introduce the idea of having underactuation in the shape manifold. That is, for systems

whose shape would normally be fully actuated, we reduce the number of actuators by replacing one — in the case of a two-dimensional shape manifold — by an elastic compliant joint. This introduces dynamics on the shape manifold. These dynamics may be exploited to allow the use of single actuation and still obtain trajectories that will enclose nonzero net curvature which engenders movement along the fiber — locomotion in the spatial variables. Periodic actuation of the single input can excite the passive elastic joint(s), in steady state the trajectory converges to a limit cycle. Even with single actuation we may still access a rich subset of closed trajectories, that will engender different kinds of locomotion. This different trajectories may be accessed by varying the frequency of actuation of the single input. Trajectories will converge to different limit cycles as frequency varies.

We have extended the idea of geometric phase in fluids, where the cyclic variation of parameters in a streaming flow allows the movement of particles initially trapped in a streaming cell to a different streaming cell. This movement between trapping regions is enabled by a series of bifurcations that occur as the parameters are varied cyclically.

8.2 Future Work

There are multiple lines of research that could be continued from the presented work. For the three link swimmer we could explore on the effect of having different shapes for the links. The aspect ratios of the ellipses can be modified and investigate how does this change the performance of the swimmer. We can extend the work to swimmers with more links, which gives even more options on how to distribute

the actuators and torsional springs. We can try and find the optimal distribution of torsional spring constants. And recalling Boyle's "Custome & Education only", we could ultimately let the swimmers learn how to swim on their own, using some Reinforcement Learning techniques. This could be done in simulation using the model with added masses, but the ultimate way would be doing it with actual experiments, deploying a swimmer in a big body of water and let it learn from experience.

For particle manipulation there are multiple things that can be done. We can continue to search for more strategies that will allow better particle transport in arrays of cylinders. We can still vary other parameters of the oscillations like the amplitude and frequency. The Maxey-Riley equation should be added to the high-fidelity simulation environment. This would allow further characterization on how do particles behave when they are near different kind of fixed points — in the sense of averaged streamlines — like saddle nodes, as well as identify where do particles go when there are bifurcations in the flow.

REFERENCES

[1] R. H. Abraham and J. E. Marsden. *Foundations of Mechanics*. AMS Chelsea Publishing, 2nd edition, 2008.

[2] R. Abrajan-Guerrero, R. Bhansali, and S. D. Kelly. Using physical experiments to estimate the curvatures of principal connections underlying swimming at low Reynolds number. In *Proceedings of the Asian Control Conference*, pages 1314–1319, 2017.

[3] R. Abrajan-Guerrero, J. D. Eldredge, S. T. Smith, and S. D. Kelly. Quasisteady particle transport in slowly varying periodic streaming flows. *IFAC Proceedings Volumes (IFAC-PapersOnline)*, 19:5859–5865, 2014.

[4] D. N. Beal, F. S. Hover, M. S. Triantafyllou, J. C. Liao, and G. V. Lauder. Passive propulsion in vortex wakes. *Journal of Fluid Mechanics*, 549:385–402, 2006.

[5] M. Bennett, M. F. Schatz, H. Rockwood, and K. Wiesenfeld. Huygens's clocks. In *Mathematical, Physical and Engineering Sciences*, volume 458, pages 563–579, 2002.

[6] A. M. Bloch. *Nonholonomic Mechanics and Control*. Springer Verlag, 2003.

[7] A. M. Bloch, P. S. Krishnaprasad, J. E. Marsden, and R. M. Murray. Nonholonomic Mechanical Systems with Symmetry. *Archive for Rational Mechanics and Analysis*, 136(1):21–99, 1996.

[8] L. Busoniu. *Reinforcement learning and dynamic programming for control (Lecture notes)*. 2012.

[9] D. E. Chang and S. Jeon. Damping-Induced Self Recovery Phenomenon in Mechanical Systems With an Unactuated Cyclic Variable. *ASME Journal of Dynamic Systems, Measurement, and Control*, 135(2):021011, 2013.

[10] D. E. Chang and S. Jeon. On the damping-induced self-recovery phenomenon in mechanical systems with several unactuated cyclic variables. *Journal of Nonlinear Science*, 23(6):1023–1038, 2013.

[11] D. E. Chang and S. Jeon. On the Self-Recovery Phenomenon for a Cylindrical Rigid Body Rotating in an Incompressible Viscous Fluid. *Journal of Dynamic Systems, Measurement, and Control*, 137(2):021005, 2015.

[12] K. Chong, S. D. Kelly, S. Smith, and J. D. Eldredge. Inertial particle trapping in viscous streaming. *Physics of Fluids*, 25(3), 2013.

[13] K. Chong, S. D. Kelly, S. T. Smith, and J. D. Eldredge. Transport of inertial particles by viscous streaming in arrays of oscillating probes. *Physical Review E*, 93(1):013109, 2016.

[14] R. G. Cox. The motion of long slender bodies in a viscous fluid Part 1. General theory. *Journal of Fluid Mechanics*, 44(4):791–810, 1970.

[15] R. Cushman, H. Duistermaat, and J. Sniatycki. *Geometry of Nonholonomically constrained systems*. World Scientific, 2009.

[16] J. Dai, H. Faraji, C. Gong, R. L. Hatton, D. I. Goldman, and H. Choset. Geometric Swimming on a Granular Surface. In *Proceedings of Robotics: Science and Systems*, 2016.

[17] J. S. De Bono, H. I. Scher, R. B. Montgomery, C. Parker, M. C. Miller, H. Tissing, G. V. Doyle, L. W. W. M. Terstappen, K. J. Pienta, and D. Raghavan. Circulating tumor cells predict survival benefit from treatment in metastatic castration-resistant prostate cancer. *Clinical Cancer Research*, 14(19):6302–6309, 2008.

[18] F. E. Fish. The myth and reality of Gray's paradox: implication of dolphin drag reduction for technology. *Bioinspiration & Biomimetics*, pages R17–R25, 2006.

[19] R. L. Hatton and H. Choset. Geometric swimming at low and high Reynolds numbers. *IEEE Transactions on Robotics*, 29(3):615–624, 2013.

[20] J. Holtsmark, I. Johnsen, T. Sikkeland, and S. Skavlem. Boundary Layer Flow Near a Cylindrical Obstacle in an Oscillating Incompressible Fluid. *Journal of the Acoustical Society of America*, 26(1):26–39, 1954.

[21] S. C. Howard, J. W. Chesna, S. T. Smith, and B. a. Mullany. On the Development of an Experimental Testing Platform for the Vortex Machining Process. *Journal of Manufacturing Science and Engineering*, 135(5):051005, 2013.

[22] M. Hunter. *Boyle Studies: Aspects of the Life and Thought of Robert Boyle (1627-91)*. Routledge, 2015.

[23] S. D. Kelly and R. Abrajan-Guerrero. Propulsive heading control and damping-induced heading recovery for a free hydrofoil with an internal rotor. In *Proceedings of the American Control Conference*, volume 2016-July, pages 6616–6621, 2016.

[24] S. D. Kelly, M. J. Fairchild, P. M. Hassing, and P. Tallapragada. Proportional heading control for planar navigation: The Chaplygin beanie and fishlike robotic swimming. *American Control Conference*, pages 4885–4890, 2012.

[25] S. D. Kelly and R. M. Murray. Geometric phases and robotic locomotion. *Journal of Robotic Systems*, 12:417–431, 1995.

[26] S. D. Kelly and R. M. Murray. The Geometry and Control of Dissipative Systems. *Proceedings of the 35th Conference on Decision and Control*, 42(3):981–986, 1996.

[27] S. D. Kelly, P. Pujari, and H. Xiong. Geometric mechanics, dynamics, and control of fishlike swimming in a planar ideal fluid. In S. Childress, A. Hosoi, W. Schultz, and J. Wang, editors, *Natural locomotion in fluids and on surfaces; swimming, flying and sliding*, pages 101–116. Springer, 2012.

[28] S. Kobayashi and K. Nomizu. *Foundations of differential geometry*, volume 1. Interscience Publishers, 1963.

[29] I. Kolá, J. Slovák, and P. W. Michor. *Natural Operations in Differential Geometry*. Springer, 1993.

[30] W. Magnus. On the exponential solution of differential equations for a linear operator. *Communications on Pure Applied Mathematics*, VII(4):649–673, 1954.

[31] S. Marras, S. S. Killen, J. Lindström, D. J. Mckenzie, J. F. Steffensen, and P. Domenici. Fish swimming in schools save energy regardless of their spatial position. *Behavioral ecology and sociobiology*, 69(2):219–226, 2015.

[32] J. E. Marsden. *Lectures on Mechanics*. Cambridge University Press, 1992.

[33] J. E. Marsden, R. Montgomery, and T. Ratiu. *Reduction, Symmetry and Phases in Mechanics*, volume 436. Memoirs of the American Mathematical Society, 1990.

[34] M. R. Maxey and J. J. Riley. Equation of motion for a small rigid sphere in a nonuniform flow. *Physics of Fluids*, 26(1983):883, 1983.

[35] L. M. Milne-Thomson. *Theoretical Hydrodynamics*. Dover, 1996.

[36] B. K. Nowakowski, S. T. Smith, B. A. Mullany, and S. C. Woody. Vortex machining: Localized surface modification using an oscillating fiber probe. *Machining Science and Technology*, 13(4):561–570, 2009.

[37] Y. Or, J. Vankerschaver, S. D. Kelly, R. M. Murray, and J. E. Marsden. Geometric control of particle manipulation in a two-dimensional fluid. In *48th IEEE Conference on Decision and Control & 28th Chinese Control Conference*, pages 19–26, 2009.

[38] D. Pais, M. Cao, and N. E. Leonard. Formation shape and orientation control using projected collinear tensegrity structures. In *American Control Conference*, pages 610–615, 2009.

[39] S. J. Portugal, T. Y. Hubel, J. Fritz, S. Heese, D. Trobe, B. Voelkl, S. Hailes, A. M. Wilson, and J. R. Usherwood. Upwash exploitation and downwash avoidance by flap phasing in ibis formation flight. *Nature*, 505:399–402, 2014.

[40] E. Purcell. Life at low Reynolds number. *American Journal of Physics*, 45(1):3–11, 1977.

[41] P. G. Saffman. The lift on a small sphere in a slow shear flow. *Journal of Fluid Mechanics*, 22(02):385, 1965.

[42] H. Schlicthing. Berechnung ebener periodischer Grenzeschichtstr{ö}mungen. *Physicalische Zeitschrift*, 33:327–335, 1932.

[43] A. Shapere and F. Wilczek. Geometry of self-propulsion at low Reynolds number. *Journal of Fluid Mechanics*, 198:557–585, 1989.

[44] S. T. Smith. *Flexures: Elements of Elastic Mechanisms*. Gordon and Breach, 2000.

[45] M. Spivak. *Calculus on manifolds*. Addison-Wesley, 1965.

[46] G. G. Stokes. On the theory of oscillatory waves. *Transactions of the Cambridge Philosophical Society*, 8:441–455, 1847.

[47] R. S. R. Sutton and A. G. a.G. Barto. *Reinforcement learning: An introduction*. MIT press Cambridge, 1998.

[48] P. Tallapragada and S. D. Kelly. Self-Propulsion of Free Solid Bodies with Internal Rotors via Localized Singular Vortex Shedding in Planar Ideal Fluids. *European Physical Journal*, 224:3185–3197, 2015.

[49] S. Vogel. *Comparative Biomechanics: Life's Physical World*. Princeton University Press, 2003.